

<https://doi.org/10.15388/vu.thesis.842>

<https://orcid.org/0009-0002-7326-6953>

VILNIUS UNIVERSITY

CENTER FOR PHYSICAL SCIENCES AND TECHNOLOGY

Tomas Mockaitis

# Electrochemical Methods for Analysis of 3D Cancer Spheroids and Enzyme Activity

**DOCTORAL DISSERTATION**

Natural Sciences

Chemistry (N 003)

VILNIUS 2025

The dissertation was prepared between 2021 and 2025 at the State Research Institute Center for Physical Science and Technology

**Academic Supervisor** – Assoc. Prof. Dr. Inga Morkvėnaitė- Vilkončienė (State Research Institute Center for Physical Science and Technology, Natural Sciences, Chemistry, N 003)

This doctoral dissertation will be defended in a public meeting of the Dissertation Defence Panel:

**Chairman** – Prof. Dr. Jaunius Urbonavičius (Vilnius Gediminas Technical University, Natural Sciences, Chemistry, N 003).

**Members:**

Assoc. Prof. Dr. Renata Butkutė (State Research Institute Center for Physical Sciences and Technology, Technological Sciences, Material Engineering, T 008),

Dr. Mathieu Etienne (French National Centre for Scientific Research, Technological Sciences, Chemical Engineering, T 005),

Habil. Dr. Rimantas Ramanauskas (State Research Institute Center for Physical Sciences and Technology, Natural Sciences, Chemistry, N 003),

Assoc. Prof. Dr. Rasa Žūkienė (Vytautas Magnus University, Natural Sciences, Biochemistry, N 004).

The dissertation shall be defended at a public meeting of the Dissertation Defence Panel at 15:00 on November 7<sup>th</sup> 2025 in Room D401 of the Center for Physical Sciences and Technology.

Address: Saulėtekio av. 3, LT-10257, Vilnius, Lithuania.

Tel. +370 5 264 8884; e-mail: [office@ftmc.lt](mailto:office@ftmc.lt)

The text of this dissertation can be accessed at the Vilnius University library, as well as on the website of Vilnius University:

[www.vu.lt/lt/naujienos/ivykiu-kalendorius](http://www.vu.lt/lt/naujienos/ivykiu-kalendorius)

<https://doi.org/10.15388/vu.thesis.842>

<https://orcid.org/0009-0002-7326-6953>

VILNIAUS UNIVERSITETAS  
FIZINIŲ IR TECHNOLOGIJOS MOKSLŲ CENTRAS

Tomas Mockaitis

# 3D vėžio sferoidų ir fermento aktyvumo analizė elektrocheminiais metodais

**DAKTARO DISERTACIJA**

Gamtos mokslai  
Chemija (N 003)

VILNIUS 2025

Disertacija rengta 2021–2025 metais Valstybiniame mokslinių tyrimų institute Fizinių ir technologijos mokslų centre.

**Mokslinė vadovė** – doc. dr. Inga Morkvėnaitė- Vilkončienė (Valstybinis mokslinių tyrimų institutas Fizinių ir technologijos mokslų centras, gamtos mokslai, chemija, N 003)

Gynimo taryba:

**Pirmininkas** – prof. dr. Jaunius Urbonavičius (Vilniaus Gedimino technikos universitetas, gamtos mokslai, chemija, N 003).

**Nariai:**

doc. dr. Renata Butkutė (Valstybinis mokslinių tyrimų institutas Fizinių ir technologijos mokslų centras, technologijos mokslai, medžiagų inžinerija, T 008),

dr. Mathieu Etienne (Prancūzijos nacionalinis mokslinių tyrimų centras, technologijos mokslai, chemijos inžinerija, T 005),

habil. dr. Rimantas Ramanauskas (Valstybinis mokslinių tyrimų institutas Fizinių ir technologijos mokslų centras, gamtos mokslai, chemija, N 003),

doc. dr. Rasa Žūkienė (Vytauto Didžiojo universitetas, gamtos mokslai, biochemija, N 004).

Disertacija ginama viešame Gynimo tarybos posėdyje 2025 m. lapkričio mėn. 7 d. 15 val. Valstybinio mokslinių tyrimų instituto Fizinių ir technologijos mokslų centro D401 posėdžių salėje.

Adresas: Saulėtekio al. 3, LT-10257, Vilnius, Lietuva, tel. +370 5 264 8884; el. paštas: office@ftmc.lt

Disertaciją galima peržiūrėti Vilniaus universiteto bibliotekoje ir VU interneto svetainėje adresu:

<https://www.vu.lt/naujienos/ivykiu-kalendorius>

## LIST OF ABBREVIATIONS

DCM – Dichloromethane  
DMSO – Dimethyl sulfoxide  
EA – Ethyl acetate  
Hex – Hexane  
HEPES – 2-[4-(2-hydroxyethyl)piperazin-1-yl]ethanesulfonic acid  
DPV – Differential pulse voltammetry  
NBCS – Newborn Bovine Calf Serum  
HepG2 – Human liver cancer cells  
FBS – Fetal bovine serum  
PFA – Paraformaldehyde  
PBS – Phosphate-buffered saline (-)  
ITO – Indium tin oxide  
[Ru(bpy)<sub>3</sub>]<sup>2+</sup> – Tris(2,2'-bipyridyl)dichlororuthenium(II) hexahydrate  
ECL – Electrochemiluminescence  
NADH – Nicotinamide adenine dinucleotide  
GSH – Glutathione  
MCF-7 – Breast cancer cells line  
MRI – Magnetic resonance imaging  
PET – Positron emission tomography  
CT – Computed tomography  
ELISA – Enzyme-Linked ImmunoSorbent Assay  
PCR – Polymerase chain reaction  
NGS – Next-generation sequencing  
RNA – Ribonucleic acid  
DNA – Deoxyribonucleic acid  
VNN1 – Vanin-1/ pantetheinase  
GGT –  $\gamma$ -glutamyl transpeptidase  
DPP-IV – Dipeptidyl peptidase-IV  
CV – Cyclic voltammetry  
EIS – Electrochemical impedance spectroscopy  
ROS – Reactive oxygen species

# CONTENTS

INTRODUCTION .....	9
1. LITERATURE REVIEW .....	14
1.1. Traditional cancer detection methods.....	14
1.1.1. Cancer imaging methods.....	14
1.1.2. Histopathology and biopsy .....	15
1.1.3. Molecular biology diagnostics tools (ELISA, PCR, NGS).....	15
1.1.4. Limitations of traditional cancer diagnostics .....	16
1.2. Biosensors in oncology .....	18
1.2.1. Definition and classification of biosensors .....	18
1.2.2. Biosensor architecture: bioreceptor, transducer and signal processor.....	19
1.2.3. Applications in cancer biomarker detection.....	20
1.2.4. Clinical relevance and representative examples .....	21
1.2.5. Comparison of biosensors with traditional diagnostic methods.....	22
1.3. Principles of electrochemical detection.....	23
1.3.1. Overview of methods: cyclic voltammetry, differential pulse voltammetry, electrochemical voltammetry, amperometry and electrochemiluminescence .....	25
1.4. Electrochemiluminescence (ECL) in cancer detection.....	26
1.4.1. ECL principles and signal generation.....	26
1.4.2. Luminophores and co-reactants .....	27
1.4.3. ECL in cancer diagnostics .....	28
1.4.4. ECL microscopy and live cell imaging.....	29
1.5. 3D cell culture models in cancer research.....	30
1.5.1. Justification for the use of 3D and 2D cultures.....	30
1.5.2. Tumour spheroids and organoids: structure and function.. .....	31
1.5.3. Real-time electrochemical monitoring of spheroids .....	33

2.	MATERIALS AND METHODS.....	36
2.1	Synthesis and characterization of VaninLP probe.....	36
2.1.1	Synthesis of compound 3.....	36
2.1.2	Synthesis of compound 4.....	36
2.1.3	Synthesis of compound 6.....	37
2.1.4	Synthesis of compound VaninLP .....	38
2.2	Preparation of stock solutions.....	39
2.3	Cell culture and spheroid fabrication.....	39
2.3.1	HepG2 cell culture (for VaninLP studies) .....	39
2.3.2.	Procedure for cell culture and MTT assay.....	40
2.3.3	MCF-7 Cell culture and spheroid fabrication .....	40
2.3.4	Spheroid fixation .....	41
2.4	Electrochemical detection of pantetheinase with VaninLP .....	41
2.4.1	Detection in biofluids (NBCS, Blood, Urine).....	41
2.4.2	Real-Time sensing and inhibition.....	42
2.5	ECL Microscopy of diffusive biocompounds in cell spheroids .	42
2.5.1	Calibration and control experiments for ECL.....	44
2.6	Diffusion simulation .....	44
2.7	Spectroscopic and spectrometric analysis.....	44
3.	RESULTS AND DISCUSSION.....	45
3.1	Probe Synthesis and physicochemical characterization.....	45
3.2.	Analytical performance of VaninLP.....	53
3.2.1.	Optimization of analytical conditions for VaninLP.....	53
3.2.2	Characterization of the VaninLP probe for the electrochemical sensing of pantetheinase .....	54
3.2.3	Characterization of the kinetic profile and selectivity of the VaninLP .....	59
3.3	Detection of pantetheinase activity in biological samples.....	61
3.3.1.	Quantitative analysis of the pantetheinase activity of tumor cell surfaces .....	61

3.3.2. Direct real-time quantification of pantetheinase activity in NBCS .....	64
3.4. Analysis of endogenous pantetheinase activity in biofluids: whole blood and urine .....	67
3.5. Characterization of 3D tumor spheroids and optimization of the ECL system.....	73
3.6. Imaging molecular diffusion from 3D spheroids via ECL .....	74
3.6.1 Visualization of co-reactant efflux from live 3D spheroids.	74
3.7. Analysis of co-reactant depletion dynamics .....	77
3.8. Characterizing the endogenous co-reactants.....	81
3.8.1. Investigating NADH as a potential co-reactant .....	83
3.8.2. Investigating GSH as the main candidate co-reactant .....	84
3.9. Platform performance and limitations: throughput and viability analysis .....	87
CONCLUSIONS .....	90
LIST OF REFERENCES.....	91
SANTRAUKA.....	108
ACKNOWLEDGEMENTS.....	125
CURRICULUM VITAE.....	126
LIST OF PUBLICATIONS AND CONFERENCES .....	127

## INTRODUCTION

Cancer is a global problem, causing one million deaths every year. According to research by the World Health Organization, the number of new cancer cases worldwide is expected to rise from 20 million in 2022 to 35 million in 2050, an increase of 77 % [1]. This increase is likely to be due to a rapidly growing and ageing human population, tobacco and alcohol consumption, obesity and pollutants in our environment. Lung cancer is the most prevalent cancer in the world, causing the highest number of deaths, followed by breast cancer, prostate cancer and rectal and colorectal cancer [2].

Cancer is defined as the uncontrolled, rapid multiplication and spread of cells throughout the body, killing healthy cells and disrupting normal organ functions [3]. Early diagnosis of cancer is very complicated, because most cancers do not cause symptoms and are undetectable in their early stages, so the disease is usually diagnosed late, when it is already advanced and difficult to treat. When cancer is detected at a late stage, it is associated with lower survival rates and aggressive treatment such as chemotherapy or surgery.

Detecting cancer at an early stage significantly improves a person's survival and the possibility of adopting more effective and less aggressive treatment methods. The point at which cancer is identified is a critical factor shaping both treatment strategies and patient survival outcomes. For instance, diagnoses made at a late stage frequently require aggressive interventions and these situations are linked with reduced survival rates [4]. In contrast, detecting cancer early on significantly boosts survival prospects. This is largely because an early diagnosis allows for the use of treatments that are not only more effective, but also frequently less demanding on the patient. While the source material clearly highlights this vital connection between diagnosis timing, treatment approaches, and survival, it doesn't provide a detailed side-by-side comparison of how different specific treatment methods affect survival rates. Therefore, the primary emphasis continues to be on early detection as the cornerstone for accessing more favorable treatment pathways and achieving better overall patient results [5]. Although scientists have recently made significant progress in early detection studies, new sensitive methods that can detect early stages of the disease are needed. Such methods would facilitate the detection of the disease and the appropriate choice of treatment. A significant challenge in oncology is the urgent requirement for new, highly sensitive methods for early cancer detection. Current approaches often fall short when cancers are in their initial, asymptomatic stages, which consequently impedes timely and precise therapeutic interventions [6]. In response, the research community is actively exploring innovative

technologies, with nanotechnology, artificial intelligence, and particularly electrochemical methods showing considerable promise [7], [8]. These efforts aim to overcome persistent limitations found in traditional diagnostic tools, such as insufficient sensitivity for early-stage disease, high operational costs, and impracticality for routine or widespread screening. Electrochemical biosensors are emerging as a compelling alternative in this landscape. They hold the potential to provide rapid and cost-effective testing characterized by high sensitivity and specificity, capable of achieving remarkably low detection limits, often in the picomolar to femtomolar range [9], [10]. Such biosensors are designed to identify key cancer-related biomarkers in bodily fluids. Furthermore, their integration with liquid biopsy platforms facilitates non-invasive and frequent monitoring, a critical component for advancing personalised medicine. Among these electrochemical techniques, electrochemiluminescence (ECL) technology is especially noteworthy. ECL-based immunoassays can attain femtomolar detection limits and have demonstrated superior performance over traditional ELISA methods in both sensitivity and speed, which is invaluable for early-stage cancer diagnostics [11].

Existing cancer diagnosis and detection methods are not sensitive enough to detect early-stage disease, and are also patient-unfriendly, time-consuming, expensive and impractical for repeat screening. Electrochemical methods are emerging as an alternative to replace the long-standing traditional methods, and their properties are very promising for improving the efficiency of cancer diagnosis and therapy monitoring [10]. Due to their high sensitivity, specificity, low detection limit and ease of use, biosensors would enable rapid, reliable and inexpensive cancer testing. Biosensors are designed to detect specific cancer-related biomarkers (proteins, DNA mutations, tumour cells) in body fluids (blood, urine) [12], [13]. By monitoring changes in biomarkers during therapy, biosensors help to track the patient's health status and to quickly modify the treatment process, thus avoiding ineffective and harmful damage to the body. The use of biosensors can be further enhanced by integrating them with 3D cell spheroid models, which more accurately replicate the behaviour and structure of tumours compared to 2D cells [14]. Combining biosensors with realistic 3D spheroid models allows for more accurate drug screening and provides deeper insights into tumor behavior [15]. This powerful integration allows for the real-time and spatially precise monitoring of dynamic cellular activities, such as metabolic processes, biomarker secretion, and responses to therapy. The crucial insights gained from this monitoring can drive progress in early cancer detection and the development of personalized treatment strategies. The grown spheroids

represent the complex microenvironment of the tumour, including nutrient and oxygen uptake, cell-to-cell interactions and barriers to drug entry [16]. Combining biosensors with electrochemiluminescence (ECL) would allow real-time monitoring of how cellular spheroids respond to drugs and changing environmental conditions *in vitro*. ECL is an advanced technique that has low background noise, high sensitivity and allows the detection of biomolecules released from spheroids [17]. ECL can determine the metabolic activity, structure and secretion of the spheroids under investigation, providing real-time information on treatment response and drug resistance.

The specific systems and methods in this work were deliberately chosen for their broad relevance and applicability in oncology. To develop a new sensing platform, we targeted the enzyme Vanin-1, a well-validated biomarker overexpressed in several human cancers, ensuring our target was clinically significant. Similarly, we used the MCF-7 cell line for our 3D spheroid studies, as it is one of the most widely used models in breast cancer research, allowing our findings to be contextualized within a vast body of literature. The core technology connecting these studies is electrochemistry, which was selected for its inherent advantages of high sensitivity, low cost, and potential for miniaturization. This choice taps into the future of diagnostics, as electrochemical assays are among the most promising for real-world biological samples. As this technology advances, devices like the ones developed here will speed up diagnosis and simplify analysis. This will ultimately make results available in minutes at the point of care, dramatically improving how we monitor cancer progression and treatment.

### **The aim of this work:**

To investigate Vanin-1 biomarker and MCF-7 cancer cell line spheroids using a synthesized VaninLP probe and electrochemiluminescence.

### **Objectives:**

1. To synthesise a VaninLP probe for the enzyme Vanin-1 and investigate its electrochemical properties.
2. To perform electrochemical tests with a synthesised probe to detect Vanin-1 enzyme in blood and urine samples.
3. To investigate co-reactants released by MCF-7 spheroids using electrochemiluminescence microscopy.

## **Scientific Novelty of the Dissertation**

The novelty of this thesis lies in the development of two complementary electrochemical platforms that address key challenges in cancer diagnostics. The first major contribution is the design, synthesis, and validation of VaninLP, the first activity-based electrochemical ratiometric probe for the enzyme Vanin-1. This work demonstrated its successful application for the direct, real-time quantification of enzyme activity in complex, unprocessed biological samples, including whole blood and on the surface of living cancer cells. The second major contribution is the pioneering use of electrochemiluminescence (ECL) microscopy to visualize endogenous, diffusive biocompounds, such as glutathione, as they are released from living 3D cancer spheroids. This established a novel, non-invasive method for the functional imaging of a tumor model's metabolic state. Together, these platforms represent a significant advance by providing new tools for both direct biomarker quantification and the functional analysis of physiologically relevant cancer models.

## **Statements for the defence**

1. The novel electrochemical probe, VaninLP, enables the sensitive, selective, and real-time quantification of pantetheinase activity in complex biological media, overcoming key limitations of traditional assays.
2. Electrochemiluminescence microscopy can be successfully employed to non-invasively visualize the release of endogenous, diffusive co-reactants (primarily glutathione) from living 3D cancer spheroids, providing a functional readout of their metabolic state.
3. Electrochemical platforms were developed to quantify pantetheinase in blood and urine and to study MCF-7 spheroid metabolism via electrochemiluminescence, enabling real-time monitoring of enzymatic biomarkers and tumor function.

## **Contribution of the Author**

The author of this dissertation was the primary researcher responsible for the experimental work, data analysis, and manuscripts preparation for the two main projects presented herein. For the first project, the author conducted the complete multi-step chemical synthesis of the VaninLP probe, prepared samples for characterization by NMR, MS, and FT-IR, and performed all electrochemical experiments. For the second project, the authors responsibilities included the growth of the 3D cancer spheroids, the manufacturing of the electrodes, and the execution of all electrochemical ECL measurements. For both studies, the author analyzed data, prepared the graphs and figures, and contributed to the preparation of the scientific manuscripts.

# 1. LITERATURE REVIEW

## 1.1. Traditional cancer detection methods

### 1.1.1. Cancer imaging methods

As the cases of cancer rise, scientists are increasingly trying to find out how to reduce it. The number of studies increases yearly and diagnostic methods improve, leading to a better understanding of the disease, and the latest technologies are enhancing the use of traditional methods [1], [18]. Traditional cancer detection methods such as imaging, histopathological analysis and molecular diagnostics play an important role in clinical oncology by detecting and determining the prevalence of the disease and by monitoring changes in cancerous lesions during treatment [19]. The main oncological diagnostic tools offering non-invasive methods to visualise tumours, stage disease and monitor treatment response are magnetic resonance imaging (MRI), computed tomography (CT) and positron emission tomography (PET) [20], [21], [22]. Magnetic resonance imaging uses a strong magnetic field and radiofrequency pulses to provide high-resolution images with clear soft tissue contrast, making it a very important technique for the detection of breast, brain and skeletal muscle tumours [23], [24], [25]. Magnetic resonance spectroscopy (MRS) is an improved version of MRI, that provides additional insights into the structure of cancer cells, their metabolic changes, which are essential for earlier detection of the affected site [26]. Although MRI is a commonly used technique, it is limited by inaccurate indications for patients who have metal implants, high cost of use and long scanning times, which is a serious problem for patients with claustrophobia [27], [28]. In contrast to MRI, computed tomography uses ionising radiation to generate fast cross-sectional images and is often used for the assessment of thoracic, abdominal and bony lesions [29]. CT is used in emergency oncology departments due to its high imaging speed, but is limited by poor soft tissue contrast and radiation exposure, which makes this method unattractive [30]. Positron emission tomography is very often combined with CT and MRI techniques, which provide information on the abnormal metabolic activity detected using radioactive tracers such as  $^{18}\text{F}$ -fluorodeoxyglucose [31]. Despite its high diagnostic value, PET has limited resolution, dependence on radioactive tracers that are short-lived and high exposure conditions, which limit its wider use [32].

While MRI, CT, and PET provide important clinical information, these imaging methods have key limitations. Their resolution is often insufficient to detect microcarcinomas or small metastases, and they may lack the sensitivity

needed for reliable early-stage cancer detection [33], [34]. PET and CT are associated with high exposure to ionising radiation and are therefore not suitable for children and adults with weak immune systems [35]. Also, these techniques require large stationary equipment and specialised staff, making them impractical for routine decentralised studies and low-resource facilities.

### 1.1.2. Histopathology and biopsy

Sample biopsy and histopathology of their ability to provide detailed cell morphology, histological assessment and molecular characterisation, remain the best choice for a definitive diagnosis of cancer today [36]. Histopathology allows tumour staging and classification based on morphological features using immunohistochemical staining, which can detect specific protein markers that help identify tumour subtypes and their therapeutic applications [37]. Although histopathology has diagnostic accuracy, it is an invasive procedure that can be associated with complications such as bleeding, infection or damage to surrounding tissues [38]. The invasive nature of biopsy limits the feasibility of this technique due to frequent sampling and the use of samples in patients with inaccessible tumour sites [39], [40]. Tumour heterogeneity is also a major limitation, as a single biopsy may not reflect the full genetic and phenotypic variability of the tumour, which may lead to misleading conclusions about the disease status [41].

### 1.1.3. Molecular biology diagnostics tools (ELISA, PCR, NGS)

Molecular biology diagnostic techniques have improved cancer diagnosis by enabling the specific detection of low levels of disease-associated nucleic acids, proteins and other biomarkers. One of the most widely used methods for the detection and quantification of tumour-associated antigens in plasma or serum is the Enzyme-Linked ImmunoSorbent Assay (ELISA) [42], [43]. ELISA has high analytical sensitivity and is relatively cost-effective, but is limited by the specificity of the antibodies and the narrow dynamic range, which can affect the accuracy and reproducibility of the assay [44], [45]. Polymerase chain reaction (PCR) methods such as quantitative PCR (qPCR) and reverse transcription PCR (RT-PCR) are essential for the detection of oncogenic mutations and viral oncogenes such as BCR-ABL1 in leukemia or human papillomavirus in cervical cancer [46], [47], [48]. PCR is a highly

sensitive method, but due to its amplification it is prone to easy contamination and false positive results [49]. Well-controlled laboratory conditions and qualified personnel are needed to avoid these problems. Next-generation sequencing (NGS) has become an indispensable tool for high-throughput sequencing of DNA and RNA fragments, which is essential for genomic profiling including the identification of point mutations, copy-number variations, gene fusions and epigenetic modifications [50], [51]. Despite the unparalleled level of analysis, NGS remains an expensive and time-consuming modality. It also requires sophisticated bioinformatics data analysis, making these methods limited to centralised laboratories with expensive equipment and difficult to access for routine clinical and point-of-care applications [52], [53].

#### 1.1.4. Limitations of traditional cancer diagnostics

While the above methods of cancer diagnosis remain essential in oncology, their application is limited by late staging, long processing times, high costs and dependence on specialised infrastructure, and the limited ability to monitor the tests in real time (Table 1) [35], [39], [51]. The problems mentioned above highlight the urgent need for alternative diagnostic platforms that are not only sensitive and accurate, but also fast, non-invasive, cost-effective and applicable at the point of care. In recent years, electrochemical biosensors have increasingly attracted the attention of researchers as promising candidates that could detect cancer markers in real time and at low cost and could be used for personalised diagnostics [9].

Table 1. Comparison of traditional cancer treatments methods.

<b>Method</b>	<b>Detections</b>	<b>Advantages</b>	<b>Limitations</b>	<b>References</b>
MRI	Tumors, soft tissue involvement, metastases.	Excellent soft tissue contrast, no ionizing radiation	Expensive, time-consuming, not for patients with metal implants	[25], [27]
CT	Tumor size, location, calcification, lymph node involvement	Fast, widely available, good for guiding biopsies	Uses ionizing radiation, less sensitive for soft tissue tumors	[20], [22], [35]
PET	Metabolically active tumors, metastases, recurrent disease	Detects cancer based on function (metabolism), very sensitive for metastases	Uses ionizing radiation, expensive, less sensitive for low-metabolic tumors	[33], [34], [35]
Histopathology	Confirms the cancer's type, grade, and local invasion by microscopically examining the biopsy sample	Provides the definitive diagnosis and cellular details essential for planning personalized therapy	Time-consuming laboratory process, quality of diagnosis depends entirely on the biopsy sample obtained	[38], [54], [55]
Biopsy	Obtains tissue or cell samples for further analysis to confirm cancer presence and type	Allows for direct sampling of the tumor, which is necessary for a conclusive diagnosis	An invasive procedure with inherent risks, potential sampling errors, and limitations for inaccessible tumors	[37], [41], [56]
ELISA	Tumor markers and cancer-related proteins in body fluids	Simple, fast, cost-effective, good for screening	Can have false positives/negatives, limited to known biomarkers	[42], [43], [44]
PCR	Specific cancer-related genes, mutations, and viruses	Extremely sensitive and specific, rapid results	High risk of contamination leading to false positives, only detects known sequences	[46], [48], [49]
NGS	Comprehensive genomic profile of a tumor (mutations, gene fusions, etc.).	Highly sensitive and comprehensive, detects known and novel genetic variants	Very expensive, time-consuming, requires specialized data analysis expertise.	[50], [51], [52]

## 1.2. Biosensors in oncology

### 1.2.1. Definition and classification of biosensors

A biosensor is defined as an analytical device that synergistically integrates a biorecognition moiety with a physicochemical transducer, allowing for the specific detection and quantification of a target analyte [57], [58]. Due to their sensitivity, specificity and ability to provide real-time data, biosensors are widely used in medical diagnostics [59]. Biosensors convert a biological recognition event into a quantifiable digital signal. This capability makes them very attractive for cancer diagnostics, where rapid and early biomarker detection is essential for effective treatment [60], [61].

Biosensors typically consist of three main components: a bio-recognition element, a transducer and a signal processor (Fig. 1.1). The bio-recognition element interacts specifically with the analyte of interest and the transducer converts this interaction into a measurable signal [62]. The signal processor then interprets and displays this signal in a user-friendly way. These components work together to provide high specificity and sensitivity in detection areas.

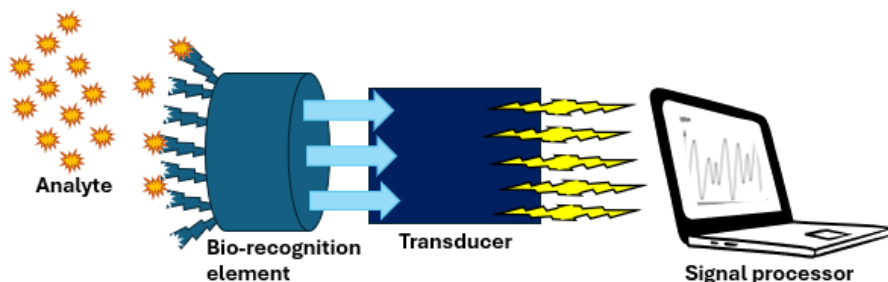


**Fig. 1.1.** Schematic diagram of biosensor components.

Based on the nature of their transmission mechanism, biosensors are generally classified into six main categories: immunosensor, enzymatic, electrochemical, optical, piezoelectric and thermoelectric (Fig. 1.2). Electrochemical biosensors measure the electrical signals generated by redox reactions and are valued for their simplicity, low cost and high sensitivity [63]. Optical biosensors detect changes in the properties of light, such as fluorescence or absorption, often using techniques such as surface plasmon resonance or interferometry [64]. Piezoelectric biosensors respond to changes in mass or the frequency of acoustic waves, making them suitable for detecting cellular events or molecular aggregation [65]. Thermal biosensors, although

less common, detect heat generated by biochemical reactions and are sometimes used in enzyme-based assays [66].

Electrochemical biosensors have shown great potential for miniaturisation and integration with portable devices, making them suitable for point-of-care applications. Their compatibility with microfabrication technologies and low power requirements make them ideal for wearable or implantable applications. In addition, advances in nanomaterial and microfluidic integration have significantly improved their analytical performance and expanded their application in complex biological matrices [67].

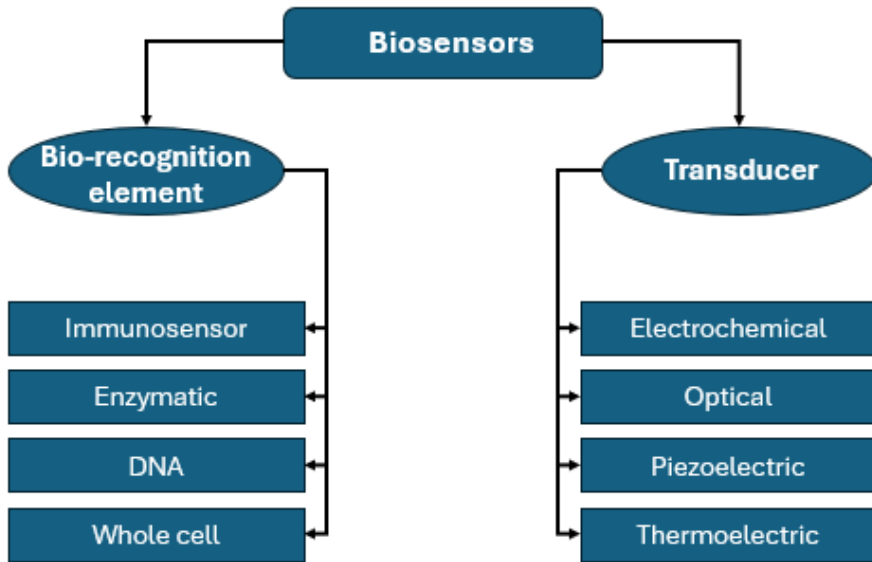


**Fig. 1.2.** Classification of biosensors based on bio-recognition element and transducer.)

### 1.2.2. Biosensor architecture: bioreceptor, transducer and signal processor

A biosensor typically consists of three functional components: a bio-recognition element or bioreceptor, a transducer and a signal processor [68]. The bioreceptor is used for molecular recognition, the transducer is needed for signal conversion and the signal processor for interpretation of the acquired data [69]. The combined action of these components translates the biochemical interaction into a readable and effective output in the form of an electrical or optical signal.

The bioreceptor is the molecular recognition element responsible for the specificity of the biosensor [70]. It can be an antibody that binds to a protein antigen, an enzyme that catalyses a specific reaction, a DNA or RNA chain that hybridises to a complementary sequence, or a synthetic molecule such as an aptamer or a molecularly imprinted polymer (MIP) [71], [72], [73]. The choice of the bioreceptor is a very important process that depends on the analyte, the sample matrix and the required sensitivity.

The transducer is responsible for converting the bio-recognition into a measurable physical signal [74]. In electrochemical biosensors, this is usually achieved by using electrodes made of precious metals or carbon-based materials, which can be further functionalised with nanostructures to improve the signal generation [75]. Transducers can detect changes in current, potential, resistance or light intensity, depending on the type of biosensor.

The signal processor takes the raw signal from the transducer, amplifies and digitises it, enabling real-time visualisation and analysis [75]. Advanced systems may use wireless modules for data transmission, as well as integrated algorithms for signal normalisation, calibration and multi-analyte comparison.

This modular architecture provides flexibility for customisation and optimisation of biosensors. It also allows for integration with microfluidic systems, enabling continuous sampling, pre-processing and multiplexed analysis in a single compact unit [76].

### 1.2.3. Applications in cancer biomarker detection

Biosensors have shown their usefulness in detecting various cancer-related biomarkers such as proteins [77], nucleic acids [78], extracellular vesicles [79], and enzymes [80]. These biomarkers play an essential role in the preventive diagnosis of cancer and the monitoring of treatment. Their presence and changes in concentration in biological fluids reflect disease progression and response to treatment, making them attractive targets for diagnosis.

Protein biomarkers such as prostate-specific antigen (PSA) and cancer antigen 125 (CA-125) have long been used in clinical practice, and electrochemical immunosensors functionalised with antibodies have been developed to detect these proteins with high sensitivity and specificity [77], [81]. Nucleic acid biomarkers, including microRNAs (miRNAs) and circulating tumour DNA (ctDNA), have attracted attention due to their high stability in the blood and their strong correlation with tumour behaviour [82].

Biosensors have also been applied to capture and analyse extracellular vesicles, such as exosomes and circulating tumour cells (CTCs), which contain fragments of proteins, RNA and DNA reflecting the molecular profile of primary tumours [83]. The biosensors integrated in the microfluidic system can distinguish exosomes by size or surface markers and simultaneously quantify their levels using electrochemical or optical detection, offering real-time analysis of tumour activity [84].

Using biosensors with liquid biopsy platforms is a powerful, non-invasive alternative to traditional tissue biopsies. This approach allows for the frequent monitoring of cancer progression, which is essential for guiding personalized treatment strategies. Enzymes such as Vanin-1 (VNN1) [12],  $\gamma$ -glutamyl transpeptidase (GGT) [85], dipeptidyl peptidase-IV (DPP-IV) [13] and alkaline phosphatase (ALP) [86] also play an important role as biomarkers for cancer diagnosis. VNN1 is highly expressed in pancreatic, colorectal and lung cancers. It is involved in tumour progression by promoting oxidative stress-induced inflammation and facilitating epithelial-mesenchymal transition (EMT), which are key metastatic processes [87]. The GGT enzyme is essential in glutathione metabolism. GGT is often elevated in liver, lung and colorectal cancers, where it enhances oxidative stress, maintains resistance to chemotherapy and contributes to tumour survival [88]. DPP-IV, which plays an important role in immune modulation and metabolic regulation, is impaired in breast, lung and pancreatic cancers, leading to impaired immune surveillance and tumour progression [89]. These enzymes are valuable not only as potential biomarkers for the early detection of cancer, but also as therapeutic targets for improving treatment strategies and patient outcomes.

#### 1.2.4. Clinical relevance and representative examples

Numerous studies and new clinical trials show the importance of biosensors in oncology. Electrochemical PSA sensors have shown improved sensitivity and faster response compared to conventional methods [90]. Biosensors for miR-155 and miR-21 have also been developed for the early detection and prognosis of various cancers [91].

In clinical trials, biosensors are of great value as they allow for rapid diagnosis, treatment selection and facilitate disease monitoring without the need for repeated invasive biopsies. For example, biosensors for breast cancer detection include human epidermal growth factor receptor 2 targeted aptamers, which allow real-time monitoring of receptor expression levels and

patient response to targeted therapies such as herceptin [92]. Similarly, prostate cancer biosensors have enabled PSA testing in primary care settings or at home, improving accessibility and patient compliance with treatment [77].

The biosensors integrated in the microfluidic system allow real-time capture and analysis of exosomes, offering minimally invasive alternatives to tissue biopsy [93]. These platforms have been used to isolate tumour-derived vesicles using specific surface proteins, followed by electrochemical or optical quantification of their nucleic acid or protein content [94]. This capability is essential to monitor tumour evolution, resistance to therapy and metastatic potential. In addition, wearable and implantable biosensors are advancing, such as glucose-based tumour metabolism sensors and flexible epidermal electronics that can detect sweat-based cancer biomarkers [95], [96]. These devices represent a shift towards continuous monitoring and integration into digital health systems.

Several biosensor platforms are clinically validated, in particular for breast, lung, colorectal and prostate cancers. Their success in the clinical setting will depend on reproducibility, biocompatibility and regulatory validation. Nevertheless, biosensors are already important in personalised medicine strategies, especially when combined with data analytics, mobile applications and AI-based interpretation systems [97], [98].

#### 1.2.5. Comparison of biosensors with traditional diagnostic methods

Electrochemical biosensors have many advantages over conventional diagnostic methods such as histopathology, imaging (MRI, CT, PET) and molecular diagnostics (ELISA, PCR). Conventional methods, although well established and clinically validated, often have several drawbacks, including high cost, the need for specialised personnel and infrastructure, long processing times and limited applicability at the point of care [34], [35], [48]. For example, imaging techniques such as MRI and PET provide valuable anatomical and functional information, but are not suitable for detecting molecular-level changes in early-stage cancers, and require expensive instrumentation and detailed clinical interpretation [33]. Similarly, histopathological analysis at biopsy remains the gold standard for cancer diagnosis, but it is invasive, time-consuming and not suitable for frequent or real-time follow-up [41], [55]. Molecular methods such as PCR and ELISA

have high sensitivity, but are usually limited by their dependence on centralised laboratories, trained personnel and complex sample preparation steps [45], [99]. In contrast, electrochemical biosensors provide rapid, label-free or minimally labelled detection using compact, inexpensive equipment, making them ideal for decentralised and point-of-care environments [97]. Their miniaturisation and integration with digital readouts allows for on-site testing and real-time data collection, which is particularly valuable in oncology, where early detection and continuous monitoring are essential. In addition, electrochemical biosensors can be adapted for multiple detection and operate efficiently in complex biological matrices without the need for sample pre-processing, offering significant advantages over traditional platforms in terms of flexibility and ease of use. These features position electrochemical biosensors not as substitutes, but as highly complementary tools that fill critical gaps in traditional diagnostics, especially in personalised medicine, resource-constrained environments, and long-term patient follow-up.

### 1.3. Principles of electrochemical detection

Electrochemical detection works based on a specific biochemical interaction, such as enzyme activity, antibody-antigen recognition or nucleic acid hybridisation, where it is converted into an electrical signal that can be measured and analysed [62]. This transformation is achieved through redox reactions taking place on the surface of the conductive electrode. When the target analyte interacts with the biorecognition element immobilised on the electrode, it causes a change in the electrochemical properties [100]. These changes are quantified as current (amperometry), potential (potentiometry) or resistance (electrochemical impedance spectroscopy), depending on the detection mode used [73], [101].

A typical electrochemical biosensor system consists of three electrodes (Fig. 1.3): the working electrode, at whose surface the analyte's redox reaction occurs, the reference electrode, which provides a stable, fixed potential for accurate measurement, and the counter electrode, which passes the current required to balance the charge at the working electrode, thus completing the circuit [102].

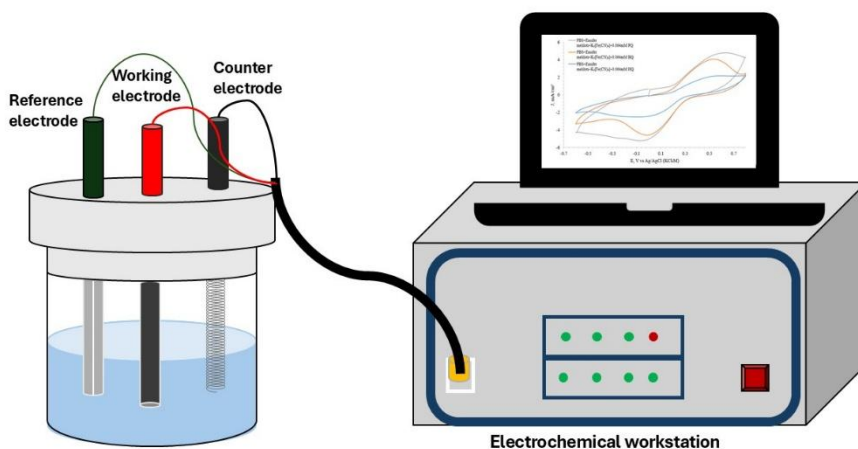


**Fig. 1.3.** Schematic illustration of a typical three- electrodes system.

Electrochemical detection is one of the most advanced technologies used for biological identification of molecules. It has several important advantages, especially for biosensors. A biological sensing element, such as an enzyme, antibody, aptamer or DNA probe, provides the system with a specific and selective response, allowing it to identify the target molecule accurately [82], [83]. When the target molecule binds to the recognition element, an electron transfer process takes place which directly or indirectly changes the charge, redox state or resistance of the electrode surface [102]. These electrochemical changes are amplified by a potentiostat, which allows them to be converted into a quantifiable signal that can be accurately measured. Electrochemical biosensors have several significant advantages, including high sensitivity, often allowing the detection of peak or femtomolar concentrations, rapid response and the possibility of miniaturisation [97]. Unlike optical systems, electrochemical sensors perform well in turbid or opaque biological samples, making them ideal for clinical matrices, such as blood, saliva and tissue fluids [12]. In addition, their simplicity and the ability to easily apply the technology to a wide range of devices, such as portable and wearable diagnostic platforms, make electrochemical detection a very attractive choice, both for research and clinical practice.

### 1.3.1. Overview of methods: cyclic voltammetry, differential pulse voltammetry, electrochemical voltammetry, amperometry and electrochemiluminescence

Electrochemical biosensors rely on a variety of signal transduction techniques to convert chemical energy into quantifiable electrical signals. Each method offers different analytical advantages, and the choice depends on the nature of the target analyte, the desired sensitivity and the operating context. Among the most widely used methods are cyclic voltammetry (CV), differential pulse voltammetry (DPV), electrochemical impedance spectroscopy (EIS) and amperometry. In recent years, electrochemiluminescence (ECL) has also gained importance in biosensors due to the combination of electrochemical control and optical signal output.

CV is the main electrochemical method used for both qualitative and semi-quantitative analysis. It involves a linear scanning of the working electrode potential while measuring the resulting current [103]. This method provides information on the redox behaviour of the system, including the reversibility of the reaction, the electron transfer kinetics and the electrochemical stability of the electrode surface [104]. DPV is based on linear scanning voltammetry by superimposing a series of voltage pulses on a potential ramp [105]. The current is measured before and after each pulse, effectively reducing background noise and increasing sensitivity. DPV is ideal for the detection of low-concentration biomarkers such as DNA, small proteins or microRNAs, often reaching detection limits in the femtomole range [106]. EIS measures the impedance (resistance and capacitance) of a biosensor system as a function of frequency in response to a small alternating voltage [101]. This label-free technique is highly sensitive to surface changes and is ideal for detecting biomolecular interactions such as antibody-antigen binding or DNA hybridisation, which do not require redox mediators [43]. EIS is widely used in sensors using aptamers, MIPs and self-assembled monolayers [107]. It also allows real-time monitoring of complex interfacial processes. Amperometric detection operates by applying a constant potential to the working electrode. The resulting current, which is generated by the oxidation or reduction of the analyte, is then measured over time [108]. Amperometry has a high temporal resolution and is commonly used in enzyme-based biosensors such as glucose or lactate sensors. It supports continuous monitoring and is well suited for wearable and implantable devices. ECL is a hybrid technique that combines electrochemical excitation with light emission. In this process, a voltage is applied to create excited states of a luminophore (e.g.  $[\text{Ru}(\text{bpy})_3]^{2+}$ ), which emits light after returning to its

ground state [14]. The ECL provides a high signal-to-noise ratio due to the absence of external light sources and background fluorescence. Its compatibility with microfluidic devices and 2D/3D cell culture platforms makes it particularly attractive for sensitive and spatially resolved biosensing in oncology [109]. ECL microscopy also allows single-cell or spheroid-level imaging, providing insights into cellular heterogeneity and tumour microenvironmental behaviour [110].

#### 1.4. Electrochemiluminescence (ECL) in cancer detection

##### 1.4.1. ECL principles and signal generation

Electrochemiluminescence is the process by which light is generated by electrochemical reactions on the surface of an electrode [17]. Unlike conventional fluorescence or chemiluminescence, which rely on external excitation sources or chemical initiators, ECL generates electronically excited particles through electrochemically induced redox reactions, thereby eliminating the need for external illumination and significantly reducing background interference [111]. The ECL process is based on the oxidation or reduction of a luminophore, e.g. tris(2,2'-bipyridyl)ruthenium(II) ( $[\text{Ru}(\text{bpy})_3]^{2+}$ ), and a suitable reactant, e.g. tripropylamine (TPrA) or L-012, that subsequently reacts to form the excited state [14], [110]. When the excited luminophore returns to the ground state, it emits a photon, producing a measurable luminescent signal [112]. The ECL reaction usually takes place at a controlled potential applied to the electrode, which allows precise spatial and temporal control of the light-emitting reaction. This mechanism enables ECL systems to achieve a high signal-to-noise ratio, because light is emitted only when a potential is applied and the emission is localised at the electrode surface [113]. The intensity of the emitted light is directly proportional to the amount of analyte present, making ECL a powerful quantitative tool for biosensor applications. Due to its controllability, high sensitivity and compatibility with aqueous biological environments, ECL has become a leading electrochemical biosensing technique, especially for the detection of small cancer biomarkers [114]. Its flexibility also allows multiplexing and integration into microfluidic chips, 3D cell culture platforms and imaging systems, making it highly applicable to modern diagnostic and research applications.

### 1.4.2. Luminophores and co-reactants

The performance and sensitivity of ECL systems is highly dependent on the choice of luminophores and co-reactants, which together generate the electronically excited materials responsible for light emission [115]. The most commonly used and well-studied ECL luminophore is tris(2,2'-bipyridyl)ruthenium(II) ( $[\text{Ru}(\text{bpy})_3]^{2+}$ ) [116]. This complex exhibits excellent photostability, reversible electrochemical behaviour and strong emission in aqueous media, making it ideal for biosensor applications. During electrochemical oxidation,  $[\text{Ru}(\text{bpy})_3]^{2+}$  forms  $[\text{Ru}(\text{bpy})_3]^{3+}$  at the electrode surface, which subsequently reacts with a reduced form of the co-reactant, such as tripropylamine (TPrA), to produce an excited state of  $[\text{Ru}(\text{bpy})_3]^{2*}$ , which emits a photon [112], [116]. In recent years, other luminophores have attracted attention for their unique properties. These include luminol derivatives, especially for the detection of reactive oxygen species, nanocrystalline quantum dots, and carbon nitride-based materials that broaden the emission spectrum and allow multiplexed detection. Additionally, L-012, a more efficient analogue of luminol, is becoming increasingly popular in biological research. It is particularly useful for detecting reactive oxygen and nitrogen species, because of its enhanced light signal and its excellent compatibility with cellular systems [117], [118].

Co-reactants play an important role in ECL performance and can significantly affect the sensitivity and selectivity of the system. Common co-reactants include TPrA, hydrogen peroxide, oxalate and ascorbic acid, each with unique redox properties and compatibility with different analytes and electrode materials [119], [120]. The choice of co-reactant is often tailored to the target molecule, the window of action potential and the presence of interfering substances in complex biological matrices [121].

Importantly, both luminophores and co-reactants can be immobilised or encapsulated on the electrode surface using nanomaterials, polymers or hydrogel matrices. This increases the stability of the ECL signal, improves the localisation of the signal and allows the development of reusable or permanent monitoring systems. Advances in the chemistry of luminophores and co-reactants are further expanding the capabilities of ECL-based biosensors, especially in multiplexed, high-throughput and cell-compatible formats.

### 1.4.3. ECL in cancer diagnostics

Electrochemiluminescence has emerged as a highly effective analytical technique for the detection of cancer-related biomarkers [122]. Due to its high sensitivity and range for analytical material, it can be used for early-stage diagnostics and personalised medicine applications [123]. ECL immunoassays are based on antibody-antigen interactions and  $[\text{Ru}(\text{bpy})_3]^{2+}$  or luminol-derived tags and can reach the limits of detection of femtomoles, surpassing traditional ELISA in both sensitivity and speed [124], [125]. One of the main applications of ECL in oncology is the detection of tumour-associated proteins such as prostate-specific antigen [126], carcinoembryonic antigen (CEA) [127] and alpha-fetoprotein (AFP) [128]. In addition to proteins, ECL platforms have been successfully applied to detect nucleic acid biomarkers including miRNA [129], ctDNA [130], and mutations in specific genes associated with different types of cancer. Hybridisation-based detection, where DNA or RNA probes are immobilised on the surface of an electrode and hybridised to target sequences, leading to the emission of ECLs, is often used in these studies. Using nanomaterials and signal amplification strategies, such as exonuclease-mediated cycling or catalytic hairpin assembly, these platforms can detect ultra-small amounts of genetic material in blood or other biological fluids. In addition, ECL has been applied to monitor the activity of cancer-related enzymes such as ALP [131], matrix metalloproteinase (MMP) [132] and telomerase, which are involved in tumour invasion, metastasis and proliferation [133]. Changes in ECL intensity due to enzyme-mediated release of co-reagents or substrate modifications are measurable, allowing a dynamic and functional assessment of disease status.

In addition, commercial diagnostic platforms such as Roche's Elecsys<sup>®</sup> system have already integrated ECL-based detection for clinical use, providing reliable, automated tumour marker panel testing in centralised laboratories. These systems demonstrate the clinical maturity of ECL and highlight its reliability, reproducibility and scalability [134]. Recent innovations include the integration of ECL biosensors on microfluidic chips and lab-on-a-chip devices for multiplexed cancer biomarker analysis at the point of care. These miniaturized systems reduce reagent consumption, shorten analysis time and support decentralised diagnostics [135]. As the need for rapid and minimally invasive cancer diagnostics continues to grow, ECL-based technologies offer a compelling solution that bridges the gap between clinical laboratory infrastructure and bedside or remote screening.

#### 1.4.4. ECL microscopy and live cell imaging

Electrochemiluminescence microscopy is an innovative extension of traditional luminescence that allows spatially resolved imaging of biochemical processes on electrode surfaces [136]. Unlike conventional fluorescence microscopy, ECL microscopy eliminates the need for external light sources or filters, thus avoiding problems such as photobleaching and autofluorescence, which are common in imaging biological samples [14], [111]. ECL emission is precisely controlled by the applied potential, which limits the generation of light to specific areas of the electrode surface. This unique feature provides high spatial resolution, low background noise and temporal control, making electrochemiluminescence microscopy ideal for dynamic imaging of biochemical reactions and cellular events [15], [115].

An important advance in ECL microscopy is its application in live cell imaging, especially in 3D tumour models such as spheroids and organoids [109], [112]. These multicellular constructs more accurately mimic the *in vivo* tumour microenvironment, including gradients of oxygen, nutrients and signalling molecules. ECL microscopy has been used to detect cell-secreted analytes such as reactive oxygen species (ROS), metabolites or enzyme activity in a non-invasive and label-free manner [126]. For example, imaging of breast cancer (MCF-7) spheroids using  $[\text{Ru}(\text{bpy})_3]^{2+}$  and L-012 allowed researchers to spatially detect ROS production in the spheroid and to observe the metabolic changes during drug exposure (Fig. 1.4) [109], [111]. This approach allows for a real-time functional readout of cellular state, which is essential for drug screening and cancer heterogeneity studies. Also, ECL microscopy platforms have been combined with microelectrode arrays and microfluidic systems to monitor single cells or localised microenvironments in 3D tissues [135]. This allows high-throughput and multiplexed imaging of biochemical processes at the single cell or subcellular level, providing insights into tumour behaviour, invasion and resistance mechanisms. The ability to image patient-derived spheroids using ECL microscopy opens up new possibilities for personalised medicine, where drug efficacy and biomarker dynamics can be assessed in a patient-specific context.



**Fig. 1.4.** An ECL imaging strategy for detecting diffusible biocompounds from 3D cell spheroids using  $[Ru(bpy)_3]^{2+}$  [109].

## 1.5. 3D cell culture models in cancer research

### 1.5.1. Justification for the use of 3D and 2D cultures

Traditional two-dimensional (2D) cell cultures (Fig. 1.5) have long served as the basis for *in vitro* assays for cancer drug screening and molecular pathway studies, but have poor reproducibility in the *in vivo* tumour microenvironment [137]. Cultures on flat media result in unnatural morphology and altered gene and protein expression. They also lack cell-cell interactions, which are essential for the reproducibility of tumour behaviour [138]. In contrast to 2D cell models, 3D cellular structures such as spheroids or organoids provide a physiologically and morphologically closer structure that better mimics natural tumour behaviour [138], [139]. These patterns promote the development of oxygen, nutrient and pH gradients, mimic tissue stiffness and support the formation of hypoxic nuclei characteristic of avascular tumour zones [137], [138]. As a result, cancer cells in 3D cultures exhibit a more realistic response to stimuli, including drug treatment, stress signals, and immune interactions [140], [141]. The use of 3D models is particularly important for pre-clinical drug evaluations as they provide predictive accuracy for drug efficacy and toxicity that is often lacking in 2D systems. In addition, 3D cultures reveal important aspects of tumour biology, such as invasion, metastasis, resistance mechanisms and heterogeneity, which are largely absent or underestimated in monolayer cultures [137]. This shift

from 2D to 3D systems reflects a broader trend in oncology research towards functional and spatial modelling of tumours, which is essential for the development of personalised medicine and precision therapy.

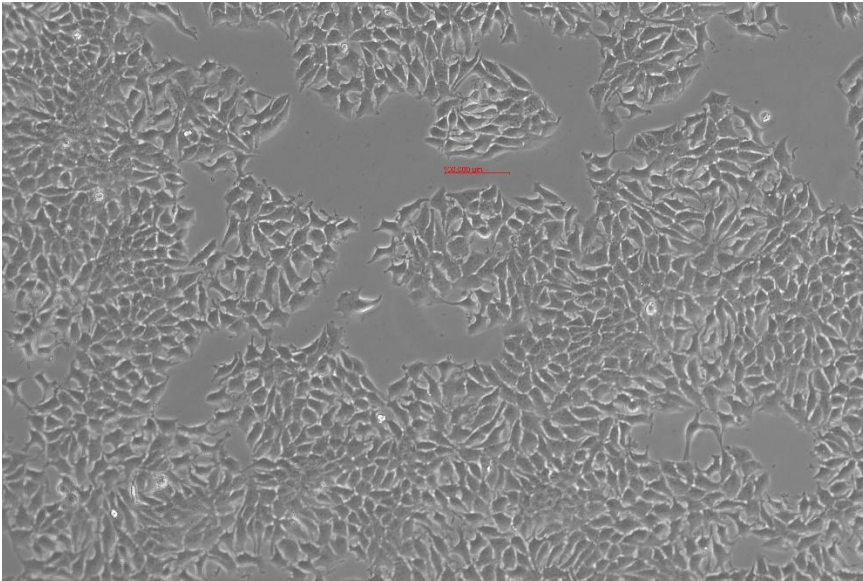


**Fig. 1.5.** Morphology of MCF-7 cells grown in a two-dimensional (2D) monolayer culture, as observed under an optical microscope.

### 1.5.2. Tumour spheroids and organoids: structure and function

Tumour spheroids (Fig. 1.6) and organoids are the two main types of three-dimensional (3D) cell culture models that accurately mimic the structural and functional properties of tumours *in vivo* [142]. Although both systems aim to reproduce the tumour microenvironment, they differ in their complexity, cellular diversity and applications. Tumour spheroids are typically derived from cancer cell lines or primary tumour cells aggregated into spherical micro-tissues, while organoids are stem cell- or tissue-derived constructs that self-organise into miniature, multicellular structures capable of mimicking the organ's intrinsic architecture and functions [143], [144].

Spheroids are well-suited for modeling solid tumors, particularly their early, non-vascularized growth stages. This is because they effectively mimic key features of real tumors, such as a compact cellular structure, radial gradients of oxygen and nutrients, and the development of a hypoxic core [137], [139], [141]. The peripheral layers of spheroids contain actively

proliferating cells, while the interior contains quiescent or necrotic cells, creating a spatially heterogeneous microenvironment that mimics the pathophysiological conditions of tumour tissues [145]. In addition to oxygen and nutrient gradients, spheroids promote extensive cell-cell and extracellular matrix (ECM) interactions that are important regulators of gene expression, differentiation, drug resistance and metastatic potential [146], [147]. Such interactions are absent in 2D cultures where cells grow in monolayers without mechanical or spatial constraints. The presence of functional ECM and tight junctions in 3D models also influences cell polarity, signal transduction pathways and drug permeability, allowing for more accurate and clinically meaningful data [146], [147], [148]. In contrast, organoids have an even greater complexity as they replicate not only the architecture of primary tissue cells, but also their functional outcomes. Organoids derived from patient tumours can maintain genomic integrity, heterogeneity and tissue-specific markers, making them invaluable tools for personalised medicine, drug testing and genetic screening [149], [150]. Although organoids are more technically challenging to create and maintain than spheroids, they provide a more accurate model of tumour biology [151].

Overall, both spheroids and organoids are advanced *in vitro* platforms for studying tumour progression, therapy resistance and biomarker expression in an environment very similar to that of tumours *in vivo*. Their structural and functional properties make them ideal models for integrating biosensors to monitor dynamic cellular processes such as metabolite secretion, enzymatic activity and drug response in real time.

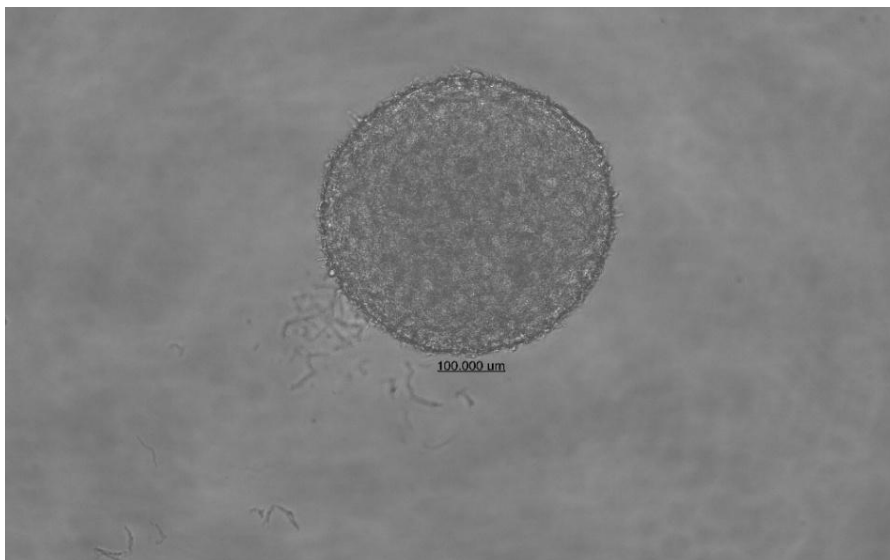


**Fig. 1.6.** An image of a mature MCF-7 spheroid taken under an optical microscope after 5 days of *in vitro* culture.

### 1.5.3. Real-time electrochemical monitoring of spheroids

Real-time electrochemical monitoring of spheroids using electrochemical techniques has opened up new opportunities to dynamically assess tumour behaviour, therapeutic response and biomarker secretion [152]. In contrast to traditional endpoint assays, which provide a static snapshot of cellular status, electrochemical biosensors allow continuous, non-invasive and quantitative assessment of the metabolites and signalling molecules secreted by cells in spheroid structures [153], [154]. This capability is particularly important for simulating *in vivo* tumour conditions, where the biochemical environment changes rapidly in response to stimuli such as hypoxia, drug exposure or nutrient deprivation [155]. A variety of electrochemical methods, including amperometry, cyclic voltammetry (CV), differential pulse voltammetry (DPV) and electrochemical impedance spectroscopy, can be used for real-time detection. These techniques allow for the monitoring of many redox-active species, from reactive oxygen species (ROS) to key metabolites like glucose and lactate [156], [157], [158]. For example, amperometric sensors integrated near or inside spheroids have been used to monitor ROS fluctuations in breast cancer models, providing insights into oxidative stress during chemotherapy [154]. In addition, EIS has been used to assess cell adhesion, proliferation and viability in spheroids embedded in

hydrogels, where changes in impedance reflect the dynamics of cell processes over time [111], [154].

Sensor integration strategies vary depending on the application. Flat electrodes placed under the spheroids facilitate fabrication and ensure optical compatibility, but may limit access to the molecules emitted from the core [111]. Embedded microelectrodes, electrodes encapsulated in hydrogels or perfused microfluidic channels may be used to improve contact with the spheroid microenvironment [122]. These configurations are valuable for capturing early biochemical changes and for creating feedback loops for drug screening or toxicity studies. In addition, the spatial and temporal resolution of electrochemical sensors allows accurate profiling of secretion patterns, providing a more detailed picture of tumour heterogeneity and functional compartmentalisation. For example, glucose and lactate sensors revealed metabolic gradients across the spheroid diameter, highlighting the transition from proliferative to hypoxic and necrotic zones [157], [158]. Such data are difficult to obtain with traditional biochemical assays, making locally monitored measures particularly important.

Electrochemiluminescence (ECL) imaging has emerged as a powerful tool for monitoring secreted metabolites and biomolecules in 3D tumour models, providing chemical specificity and spatial resolution. ECL allows real-time, non-destructive visualisation of dynamic biochemical processes, such as oxidative stress, enzymatic activity and metabolic signalling, which are critical for cancer development and treatment response [109], [157]. The main advantage of ECL is the spatially and temporally restricted generation of light emission, which reduces background interference and allows the detection of analytes at extremely low concentrations [14]. Luminophores such as  $[\text{Ru}(\text{bpy})_3]^{2+}$ , L-012 or luminol derivatives used in combination with reactive co-reactants or enzyme substrates allow the detection of localised chemical changes related to cell function [121], [133]. For example, L-012 has been used to image ROS released by MCF-7 breast cancer spheroids during chemotherapy, revealing concentration gradients at the spheroid surface and core.

ECL microscopy systems often have transparent or semi-transparent electrodes to allow both optical and electrochemical access. Spheroids are placed directly on the electrode or suspended in a microfluidic channel aligned with the ECL sensor [135]. As analytes diffuse from the spheroid into the electrode environment, the ECL luminophore reacts and produces localised light, which is captured by sensitive detectors such as CCD cameras or photomultipliers (Fig. 1.4) [109]. These images allow quantification of analyte concentrations, monitoring of temporal changes and visualisation of

biochemical gradients in a 3D structure. ECL imaging is particularly valuable for real-time assessment of therapeutic efficacy. Shortly after treatment begins, we can detect changes in ROS, enzyme activity, or the secretion of cancer-specific metabolites. This provides a functional readout that complements standard viability assessments, offering a more nuanced understanding of the treatment response [111], [137], [155].

## 2. MATERIALS AND METHODS

### 2.1 Synthesis and characterization of VaninLP probe

#### 2.1.1 Synthesis of compound 3

Compound 3 (Scheme 1) was synthesized following a modified procedure reported by Ma's group [159]. In an oven-dried, 2-neck round-bottomed flask containing 950 mg of compound 1 (Calcium-D-pantothenate; Sigma-Aldrich, USA & TCI, Japan) and 93.5 mg of (1S) -(+)-10-camphorsulfonic acid (CSA; Sigma-Aldrich, USA & TCI, Japan), 15 mL of trifluoroacetic acid (TFA; Sigma-Aldrich, USA & TCI, Japan) was added and dropwise at 0 °C until all solids dissolved. Then the TFA was removed by evaporation under reduced pressure to yield colorless oil. To this oil, 20 mL of dichloromethane (DCM; Sigma-Aldrich, USA & TCI, Japan) and 2.25 g of anisaldehyde dimethyl acetal (Sigma-Aldrich, USA & TCI, Japan) were added and the resulting solution was stirred at room temperature for 8 hours. The reaction was subsequently quenched with 1 M aqueous sodium carbonate (30 mL) (TCI, Japan), and the precipitate that formed was removed by filtration. The filtrate was acidified to pH 4.5 with acetic acid (TCI, Japan), and the product was extracted with DCM. The combined organic layers were dried over anhydrous magnesium sulfate (MgSO<sub>4</sub>; TCI, Japan) filtered, and concentrated under reduced pressure. This procedure yielded compound 3 as a white solid (1.3 g, 55 % yield), which was used in the subsequent step without further purification.

#### 2.1.2 Synthesis of compound 4

Following a procedure reported by Lin's group [85], Compound 4 (Scheme 1) was synthesized in a one-pot, two-step reaction from Compound 3. To a solution of compound 3 (1.00 g, 0.244 mmol, 1.0 eq) in anhydrous DCM (10 mL), N-hydroxysuccinimide (0.42 g, 0.365 mmol, 1.5 eq) (NHS; Sigma-Aldrich, USA & TCI, Japan) and 1-ethyl-3-(3-dimethylaminopropyl) carbodiimide (0.70 g, 0.365 mmol, 1.5 eq) (EDC; Sigma-Aldrich, USA & TCI, Japan) were added. The reaction mixture was stirred at room temperature under a nitrogen atmosphere overnight. Extract using 10 mL ethyl acetate (EA; Sigma-Aldrich, USA & TCI, Japan) dilute with water (2x20 mL), collect the organic layer and dried using magnesium sulfate. To the same flask, a solution of 4-aminobenzyl alcohol (0.533 g, 0.488 mmol, 2.0 eq)

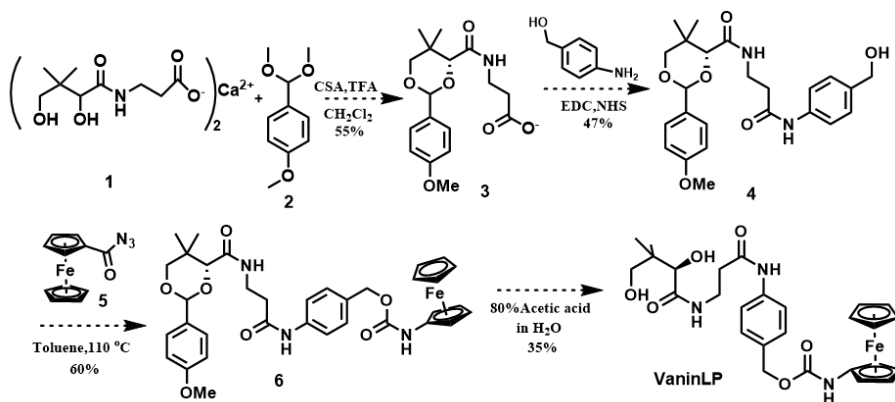
(Sigma-Aldrich, USA & TCI, Japan) in anhydrous DCM (20 mL) was added, and the stirring was continued for an additional overnight period at room temperature. Following completion, the reaction mixture was poured into a separatory funnel and washed with water (3x). The organic layer was then separated and collected for further processing. The workup procedure involved drying the organic phase over anhydrous MgSO<sub>4</sub>, followed by filtration. After concentrating the filtrate under reduced pressure, the crude product was purified via flash chromatography (silica gel), using a 1:1 solvent system. (v/v) mixture of EA and hexanes (Hex; Sigma-Aldrich, USA & TCI, Japan) to yield Compound 4 as a light-yellow foamy product (0.855 g, 47 % yield).

### 2.1.3 Synthesis of compound 6

Compound 6 was synthesized following a literature procedure Lin's group [85]. We added compound 4 (0.80 g, 0.155 mmol, 1.0 eq), compound 5 (Scheme 1) (0.55 g, 0.187 mmol, 1.2 eq), and 4 mL of toluene (Sigma-Aldrich, USA & TCI, Japan ) to a double-necked round-bottomed flask fitted with a reflux condenser. The reaction mixture was heated to 90 °C and stirred for 2.5 hours under a nitrogen atmosphere. After cooling to room temperature, silica gel was added directly to the flask, and the solvent was removed under reduced pressure to adsorb the crude product onto the silica. The material was then purified by flash chromatography, eluting with a 3:4 (v/v) mixture of EA and Hex, to afford Compound 6 as a brownish-red solid (0.588 g, 60 % yield)

### 2.1.4 Synthesis of compound VaninLP

The synthesis of VaninLP was performed by dissolving compound 6 (130 mg, 0.25 mmol) in 80 % aqueous acetic acid (1 mL) in a round-bottomed flask. The solution was then stirred at room temperature for 2 hours under a nitrogen atmosphere. Once the reaction was complete, the mixture was diluted with water and extracted three times with DCM. The combined organic layers were washed sequentially with a saturated aqueous potassium carbonate ( $K_2CO_3$ ; Sigma-Aldrich, USA) solution and brine, dried over anhydrous sodium sulfate ( $Na_2SO_4$ ; Sigma-Aldrich, USA), filtered, and the solvent was removed under reduced pressure. The resulting crude product was then purified by flash column chromatography on silica gel, using a 1:4 mixture of methanol and DCM as the eluent. This procedure yielded VaninLP as a yellow crystalline solid (118 mg, 35 % yield).



**Scheme 1.** Synthesis of VaninLP [85].

## 2.2 Preparation of stock solutions

All experimental solutions were based on a 0.1 M HEPES buffer (pH 7.0), prepared from HEPES powder (Sigma-Aldrich, USA) and NaOH pellets (TCI, Japan). A primary stock solution of the pantetheinase (R&D Systems, Inc, USA) enzyme was made in this buffer at 1  $\mu\text{g}/\text{mL}$ , stored in aliquots at -80 °C, and diluted to working concentrations of 0.1  $\mu\text{g}/\text{mL}$  and 0.01  $\mu\text{g}/\text{mL}$  as needed.

For the VaninLP probe, a 5 mM stock was created by dissolving it in the HEPES buffer and mixing it 1:1 (v/v) with Dimethyl sulfoxide (DMSO; Sigma-Aldrich, USA & TCI, Japan) for use in assays, while a separate 10 mM stock was prepared directly in DMSO for other applications.

For biological sample analysis, blood and urine were diluted with the HEPES buffer to final concentrations of 50 % and 20 % (v/v), respectively.

## 2.3 Cell culture and spheroid fabrication

### 2.3.1 HepG2 cell culture (for VaninLP studies)

Human liver cancer HepG2 cells (from the Institute of Biochemical and Biomedical Engineering at the National Taipei University of Technology, Taiwan) were maintained in Modified Eagle Medium (MEM) supplemented with 10 % fetal bovine serum (FBS; Gibco USA) and a 1 % antibiotic solution (penicillin, streptomycin, amphotericin). The cells were cultured in a humidified incubator at 37 °C with a 5 % CO<sub>2</sub> atmosphere. For routine passaging at approximately 90 % confluency, cells were washed with PBS, detached with trypsin (1 mL, 5 min, 37 °C), and neutralized with fresh medium. The cell suspension was then pelleted by centrifugation (1000 rpm, 5 min, 4 °C), resuspended in fresh medium, and counted using the Trypan blue exclusion method before being used for experiments.

### 2.3.2. Procedure for cell culture and MTT assay

To assess cytotoxicity using an MTT assay (Thermo Scientific, USA), HepG2 cells were seeded into a 24-well plate at a density of  $1 \times 10^6$  cells/mL and allowed to adhere overnight. The culture medium was then replaced with test solutions. The experimental group was treated with 50  $\mu$ M VaninLP in 0.1 M HEPES buffer (pH 7.0), while the blank control group received an equivalent small volume of DMSO in the same buffer. After incubating for time points of 2, 4, and 6 hours, the solutions were removed. MTT reagent (5 mg/mL stock solution in PBS) was then added to each well, followed by a 3-hour incubation in the dark at 37 °C. Finally, the resulting purple formazan crystals were dissolved in isopropanol, and the absorbance was measured at 562 nm. Cell viability was calculated relative to the control group using the formula below, and cytotoxicity was determined by subtracting this value from 100 %.

$$\text{Cell Viability (\%)} = \frac{OD (\text{sample})}{OD (\text{control})} \times 100 \%$$

Where:

*OD (sample)* is the absorbance of cells treated with VaninLP

*OD (control)* is the absorbance of cells treated with the DMSO

### 2.3.3 MCF-7 Cell culture and spheroid fabrication

MCF-7 human breast cancer cells, (Institute of Development, Aging and Cancer at Tohoku University, Japan), were routinely cultured in RPMI 1640 medium (Nacalai Tesque, Japan) supplemented with 10 % FBS (Gibco, USA) and 1 % penicillin-streptomycin (Nacalai Tesque, Japan). The cells were maintained in a humidified incubator at 37 °C with a 5 % CO<sub>2</sub> atmosphere. To generate spheroids, a cell suspension was prepared and dispensed into U-shaped 96-well plates (Sumitomo Bakelite, Japan) at densities ranging from 100 to 5000 cells in each 200  $\mu$ L well. These plates were then cultured from 1 to 7 days to allow for spheroid self-assembly. Following the growth period, the fully formed spheroids were collected and washed twice with PBS (-) (Nacalai Tesque, Japan) and once with the ECL assay solution before use.

### 2.3.4 Spheroid fixation

For control experiments, a set of MCF-7 spheroids was chemically fixed to serve as a non-viable reference. This was achieved by incubating the spheroids in a 4 % paraformaldehyde (PFA) (Thermo Scientific, USA) solution for one hour, followed by a one-hour wash in fresh PBS to remove any residual PFA. Both these fixed spheroids and a parallel set of unfixed (live) spheroids were then stained with Propidium Iodide (PI) using a commercial Double Staining Kit (Dojindo, Japan), following the manufacturer's protocol. Finally, the stained spheroids were imaged and observed under a Nikon ECLIPSE Ti2 fluorescence microscope (Nikon, Japan).

## 2.4 Electrochemical detection of pantetheinase with VaninLP

All electrochemical measurements were performed on a CHI 611D (CH Instruments, USA) electrochemical workstation using a standard three-electrode cell. The electrochemical cell was comprised of three electrodes: a glassy carbon – working electrode (GCE) with a 0.071 cm<sup>2</sup> surface area, a platinum wire – counter electrode and an Ag/AgCl – reference electrode saturated in KCl. Before each experiment, the GCE surface was polished with sequential alumina slurries (0.5, 0.3 and 0.05 microns) and rinsed thoroughly with deionized water.

CV scans were conducted from -0.3 V to +0.6 V at a rate of 0.05 V/s. DPV was performed from -0.3 V to +0.4 V with a pulse amplitude of 0.05 V, a pulse width of 0.05 s., and a quiet time of 2 s. Unless stated otherwise, all tests were run three times at 37 °C in a 0.1 M HEPES buffer (pH 7.0) containing 0.5 % DMSO.

### 2.4.1 Detection in biofluids (NBCS, Blood, Urine)

The pantetheinase activity in various biological fluids was measured using the VaninLP probe. In each assay, the biological sample was incubated with 50 μM VaninLP in a total volume of 1 mL of 0.1 M HEPES buffer (pH 7.0), with specific conditions adjusted for each sample type. For Newborn Bovine Calf Serum, 50 μL of serum was treated with 100 μM 1,4-dithiothreitol (DTT; Thermo Scientific, USA) and incubated at 37 °C for 30

minutes. Blood samples used a larger volume of 500  $\mu\text{L}$  with 50  $\mu\text{M}$  DTT under the same incubation conditions. In contrast, the assay for urine involved 200  $\mu\text{L}$  of the sample with 50  $\mu\text{M}$  DTT, but was maintained at room temperature for 30 minutes. Following their respective incubations, all samples were analyzed by DPV.

#### 2.4.2 Real-Time sensing and inhibition

The pantetheinase reaction in biofluids was monitored in real-time by recording DPV measurements every 5 to 10 minutes. For inhibition studies, this procedure was modified by including 1  $\mu\text{M}$  pantetheinase inhibitor RR6 (Sigma-Aldrich, USA), which was added either at the start of the reaction or after 30 minutes of progress.

#### 2.5 ECL Microscopy of diffusive biocompounds in cell spheroids

An ITO working electrode covered with an insulation film (Elegrip tape with 10 holes, Denka Adtecs, Japan) and a PDMS chamber was used (Fig. 2.1A). This was placed under an inverted microscope (ECLIPSE Ti2-U, Nikon) with an EM-CCD camera (ImagEM X2, Hamamatsu Photonics). A Pt wire counter electrode and an Ag/AgCl (sat. KCl) reference electrode were connected to a potentiostat (CompactStat, Ivium Technologies)

The experiments were conducted using a custom electrochemical cell designed for simultaneous microscopic observation. The core of this setup was an indium tin oxide (ITO) slide serving as the working electrode. This electrode was masked with an insulating Elegrip tape that featured an array of 10 micro-holes, and a PDMS chamber was attached to hold the sample solution (Fig. 2.1B).

This entire electrode assembly was mounted on the stage of a Nikon ECLIPSE Ti2-U inverted microscope, and images were captured with an ImagEM X2 EM-CCD camera (Fig. 2.1C) (Hamamatsu Photonics). A platinum wire counter electrode and an Ag/AgCl reference electrode saturated in KCl were also placed within the PDMS chamber to complete the electrochemical circuit. The entire three-electrode system was controlled by a CompactStat potentiostat (Fig. 2.1D) (Ivium Technologies).

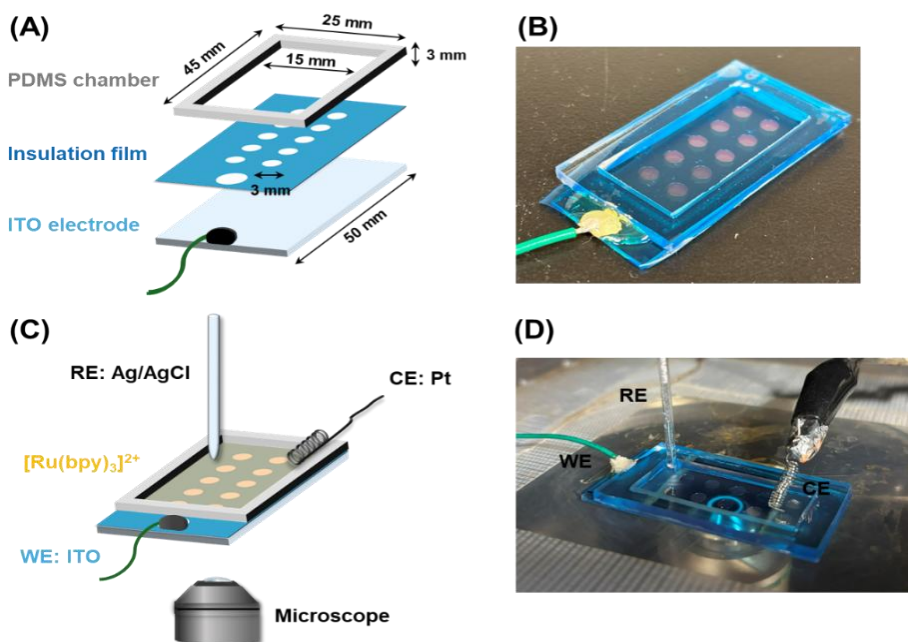


**Fig. 2.1.** Overview of the electrochemical device. (A) Fabrication involved masking an ITO electrode with a 10 – hole insulating film to define the working electrodes. (B) Photograph of the fabricated device. (C) Schematic illustration of the cell, defining the reference and counter electrodes. (D) Image of the complete electrochemical cell assembly [109].

For ECL imaging, the device chamber was filled with a PBS solution containing 5 mM  $[\text{Ru}(\text{bpy})_3]^{2+}$  (Sigma-Aldrich, USA) and MCF-7 spheroids were carefully placed inside. The benchmark luminophore,  $[\text{Ru}(\text{bpy})_3]^{2+}$ , was selected for its high stability, robust ECL efficiency in aqueous solutions, and relatively low toxicity, making it the ideal and most reliable choice for validating these live-cell assays. The experiment was initiated by applying a potential step from 0 V to 1.2 V while simultaneously beginning a 15-second camera exposure.

This applied potential served a dual purpose: it oxidized the ruthenium complex to generate ECL light and induced electroporation in the spheroids to allow biocompounds to diffuse inside. The resulting grayscale ECL images were processed using ImageJ software (NIH, USA), where the maximum intensity value from each image was extracted for quantitative analysis and graphing.

### 2.5.1 Calibration and control experiments for ECL

To quantify the response of key biological analytes, calibration curves were generated for both NADH (FUJIFILM Wako Pure Chemical Corporation, Japan) and reduced glutathione (FUJIFILM Wako Pure Chemical Corporation, Japan). This was done by preparing a series of standards in PBS containing a fixed concentration of 5 mM  $[\text{Ru}(\text{bpy})_3]^{2+}$  and varying amounts of either NADH (0  $\mu\text{M}$  – 1000  $\mu\text{M}$ ) or GSH (0 mM – 5 mM). The ECL signal for each standard was then measured under identical experimental conditions.

To further investigate the electrochemical mechanism, CV was used. The CVs for 1 mM NADH and 1 mM GSH were recorded at a scan rate of 100 mV/s, both in the presence and absence of 5 mM  $[\text{Ru}(\text{bpy})_3]^{2+}$ , to clarify their interaction with the ECL coreactant.

### 2.6 Diffusion simulation

Numerical simulations were developed to model molecular diffusion using COMSOL Multiphysics® software (ver. 5.4). The model was constructed in a 2D axisymmetric space, and the Transport of Diluted Species module was employed to describe the physics. A diffusion coefficient of  $1 \times 10^{-9} \text{ m}^2/\text{s}$  was assigned to the species of interest. A time-dependent study was then conducted to simulate the evolution of the concentration profile over time (Fig. 3.34).

### 2.7 Spectroscopic and spectrometric analysis

$^1\text{H}$  NMR spectra were recorded on a Bruker Avance III 300 spectrometer (300 MHz) at the instrument centre of the National Taipei University of Technology, Taiwan. Additional spectra were acquired on a Bruker Avance III 500 spectrometer (500 MHz) at the Taipei Medical University instrument centre, Taiwan. Mass spectrometry analysis was conducted on a Micromass LCT device at National Taiwan University, Taiwan.

### 3. RESULTS AND DISCUSSION

#### 3.1 Probe Synthesis and physicochemical characterization

The synthesis of the ratiometric electrochemical probe, VaninLP, was accomplished through a four-step route beginning with Calcium-D-pantothenate (compound 1), as outlined in Scheme 1. The first step focused on protecting the diol group of compound 1. This was achieved through an acid-catalyzed reaction with 4-methoxybenzaldehyde dimethyl acetal, which successfully formed the corresponding acetal, Compound 3, as a white solid in 55 % yield.

The structure of this protected intermediate was rigorously confirmed by  $^1\text{H}$  NMR spectroscopy (Fig. 3.1). The successful installation of the protecting group was immediately evident from several new, diagnostic signals. The presence of the para-substituted aromatic ring was confirmed by two distinct doublets between 6.5 – 7.5 ppm. Furthermore, a sharp singlet at 5.44 ppm was characteristic of the newly formed acetal proton ('g'), while another singlet at 3.8 ppm corresponded to the three protons of the methoxy group ('a').

All other observed signals were fully consistent with the rest of the molecular structure. The amide proton appeared as a broad signal around 6.8 ppm, and protons on the aliphatic backbone were observed in their expected regions. Most notably, a prominent signal at 1.0 ppm, integrating to six protons, confirmed that the gem-dimethyl group from the starting material remained intact. Taken together, this NMR data provides clear and definitive evidence for the successful formation of compound 3.

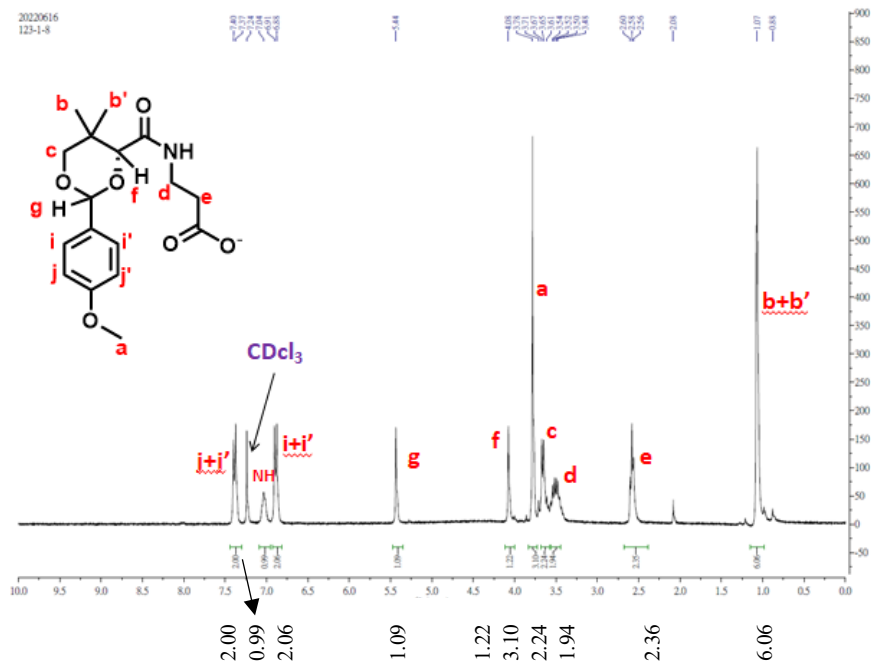


**Fig. 3.1**  $^1\text{H}$  NMR spectrum of compound 3.  $^1\text{H}$  NMR (300 MHz,  $\text{CDCl}_3$ )  $\delta$  7.49 – 7.21 (m, 2H), 6.98 (d,  $J = 36.1$  Hz, 1H), 6.89 (d,  $J = 8.8$  Hz, 2H), 5.44 (s, 1H), 4.08 (s, 1H), 3.78 (s, 3H), 3.66 (q,  $J = 11.5$  Hz, 2H), 3.51 (dd,  $J = 12.8, 6.3$  Hz, 2H), 2.58 (t,  $J = 6.1$  Hz, 2H), 0.97 (d,  $J = 56.1$  Hz, 6H) [12].

In the next synthetic step, compound 3 underwent an amide coupling reaction with 4-aminobenzyl alcohol. The reaction, which utilized EDC and NHS as coupling agents, successfully produced compound 4 as a light-yellow foam with a 47 % yield.

The structure of compound 4 was rigorously verified by  $^1\text{H}$  NMR spectroscopy (Fig. 3.2). The successful incorporation of the 4-aminobenzyl alcohol group was immediately clear from several new diagnostic signals. Two new doublets appeared in the aromatic region (7.2 – 7.6 ppm) corresponding to this new moiety's aromatic protons ('k+k' and 'l+l'), alongside a singlet for its benzylic protons ('m') at 4.63 ppm. Crucially, the formation of the new amide bond was confirmed by the appearance of an amide proton ('NH') signal around 8.03 ppm.

Furthermore, the spectrum confirmed that the rest of the molecule remained intact after the reaction. The characteristic signals for the acetal protecting group, including its own aromatic protons ('i+i' and 'j+j') and the acetal and methoxy protons ('g' and 'a'), were still present. The signals

corresponding to the original pantothenate backbone, most notably the prominent gem-dimethyl group (“b+b’”), were also retained. The integration of all protons was consistent with the proposed structure, confirming the successful synthesis of compound 4.

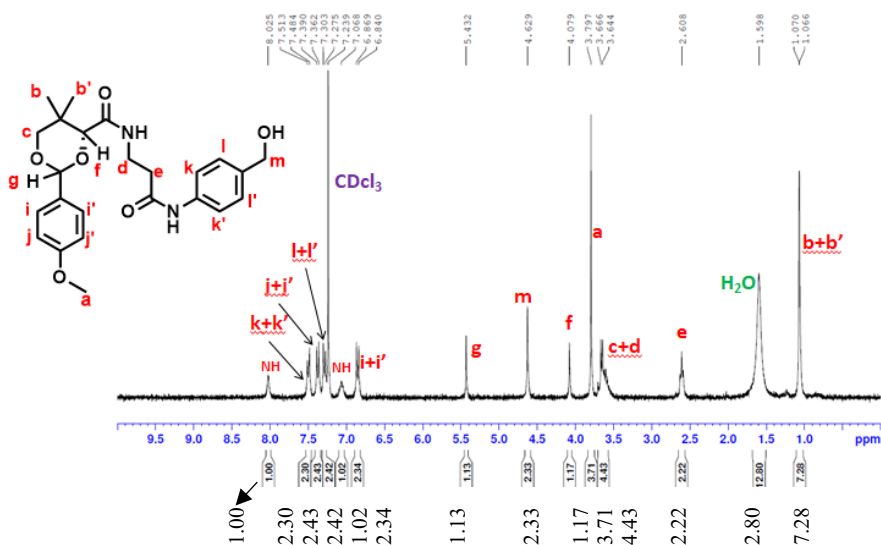


**Fig. 3.2.**  $^1\text{H}$  NMR spectrum of compound 4.  $^1\text{H}$  NMR (300 MHz,  $\text{CDCl}_3$ )  $\delta$  8.025 (s, 1H), 7.53 (d,  $J = 8.6$  Hz, 2H), 7.50 – 7.24 (m, 4H), 7.13 – 7.07 (m, 1H), 6.87 (d,  $J = 8.7$  Hz, 2H), 5.43 (s, 1H), 4.63 (s, 2H), 4.08 (s, 1H), 3.8 (s, 3H), 3.69 (d,  $J = 6.4$  Hz, 4H), 2.64 (s, 2H), 1.10 (s, 6H) [12].

The structure of the synthesized intermediate, compound 6, was comprehensively established through spectroscopic and spectrometric analysis. The  $^1\text{H}$  NMR spectrum was fully consistent with the proposed structure, with all proton signals appearing in their expected locations (Fig. 3.3). FT-IR spectroscopy was used to further confirm the structure by identifying key functional groups (Fig. 3.5). The analysis showed a strong  $\text{C}=\text{O}$  stretching vibration at  $1695\text{ cm}^{-1}$ , which evidenced the formation of the new carbamate bond, while an N-H amine stretch was also observed at  $3400\text{ cm}^{-1}$ . The identity of the compound was definitively confirmed by ESI mass spectrometry, which showed a molecular ion peak  $[\text{M}]^+$  at  $m/z$  669.21, matching the calculated exact mass for the formula  $\text{C}_{35}\text{H}_{39}\text{FeN}_3\text{O}_7$  (Fig. 3.4).

This fully characterized product was obtained by reacting compound 4 with azidoferroccene in a key step designed to install the ferrocene reporter and

a self-immolative linker (Scheme 1). The reaction proceeded efficiently to yield compound 6 as a brownish-red solid in 60 % yield.

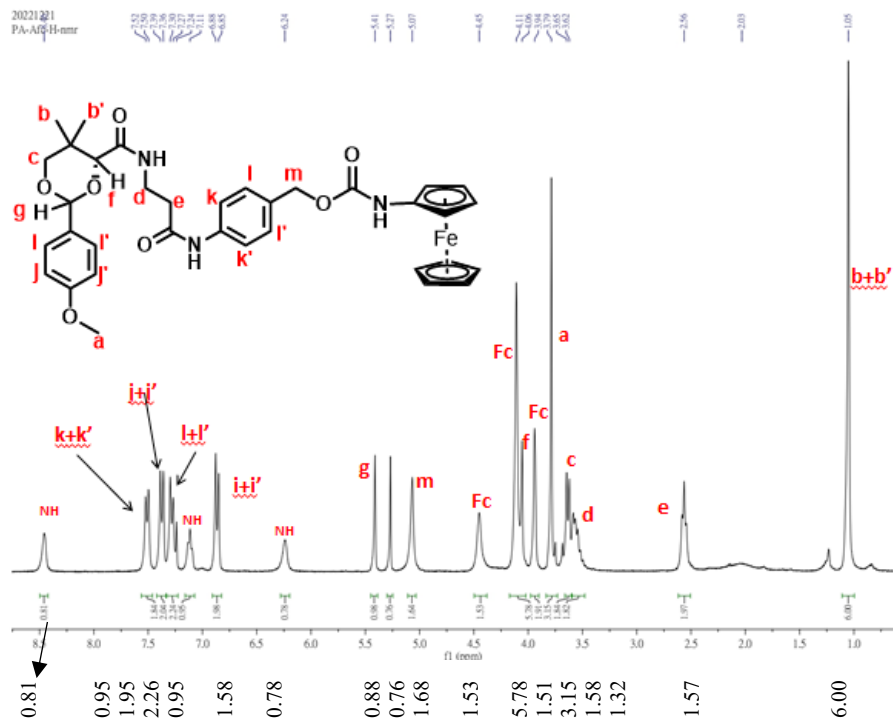


**Fig. 3.3.**  $^1\text{H}$  NMR spectrum of compound 6.  $^1\text{H}$  NMR (300 MHz,  $\text{CDCl}_3$ )  $\delta$  8.46 (s, 1H), 7.51 (d,  $J = 7.8$  Hz, 2H), 7.37 (d,  $J = 8.2$  Hz, 2H), 7.33 – 7.23 (m, 2H), 7.11 (s, 1H), 6.86 (d,  $J = 8.3$  Hz, 2H), 6.24 (s, 1H), 5.41 (s, 1H), 5.27 (s, 1H), 5.07 (s, 2H), 4.45 (s, 2H), 4.08 (d,  $J = 15.9$  Hz, 6H), 3.94 (s, 2H), 3.79 (s, 3H), 3.63 (d,  $J = 7.4$  Hz, 2H), 3.59 – 3.48 (m, 2H), 2.56 (s, 2H), 1.05 (s, 6H) [12].

The  $^1\text{H}$ NMR spectrum of compound 6 (Fig. 3.3) provided comprehensive structural confirmation, with signals corresponding to every part of the complex molecule. Evidence that the core structure remained intact during the reaction was clear, as protons from the pantothenate backbone and the 4-methoxybenzylidene acetal group (‘a’, ‘b+b’, ‘c’, ‘d’, ‘e’, ‘f’, ‘g’, ‘i+i’, ‘j+j’) were all observed in their expected regions.

Crucially, the spectrum also showed a distinct set of new signals that verified the successful incorporation of the ferrocene-containing moiety. The

most definitive of these were the characteristic signals for the ferrocenyl (Fc) protons, which were clearly visible in the 4.0 ppm – 4.5 ppm region. This was further supported by the appearance of new aromatic ('k+k', 'l+l') and benzylic ('m') protons belonging to the 4-aminobenzyl linker unit. Additionally, multiple amide and carbamate (NH) proton signals were observed between 6.0 ppm and 8.5 ppm. The integration of all peaks was fully consistent with the assigned structure, confirming the successful synthesis of compound 6.

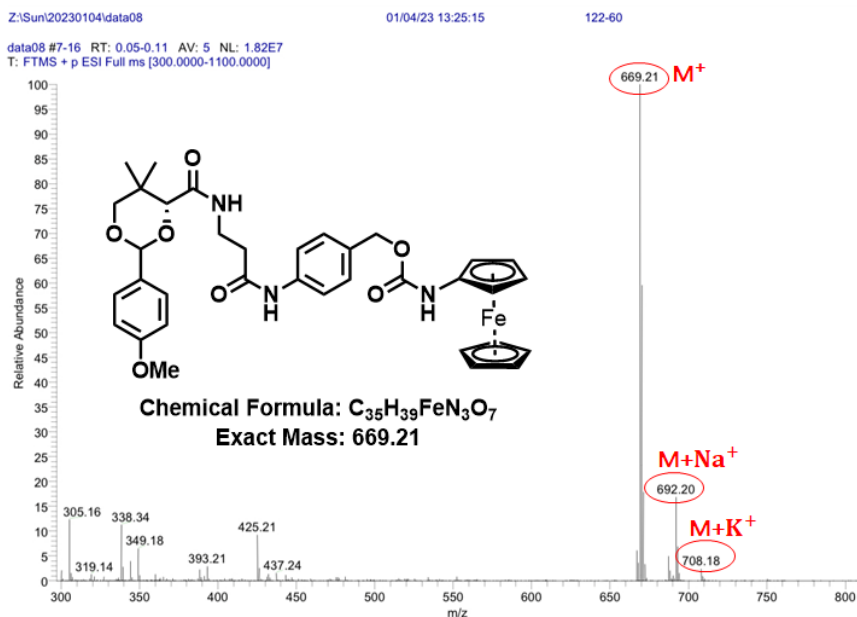


**Fig. 3.4.** Mass spectrum of compound 6 [12].

Electrospray ionization mass spectrometry (ESI-MS) provided definitive confirmation of the molecular weight for compound 6 (Fig. 3.4). The mass spectrum clearly showed a prominent molecular ion peak ( $[M]^+$ ) at  $m/z$  669.21, which is in excellent agreement with the calculated exact mass for the proposed formula,  $C_{35}H_{39}FeN_3O_7$ . The assignment was further corroborated by the presence of characteristic sodium and potassium adduct ions. These were observed as  $[M+Na]^+$  at  $m/z$  692.20 and  $[M+K]^+$  at  $m/z$  708.18, respectively, providing additional strong support for the structure of compound 6.

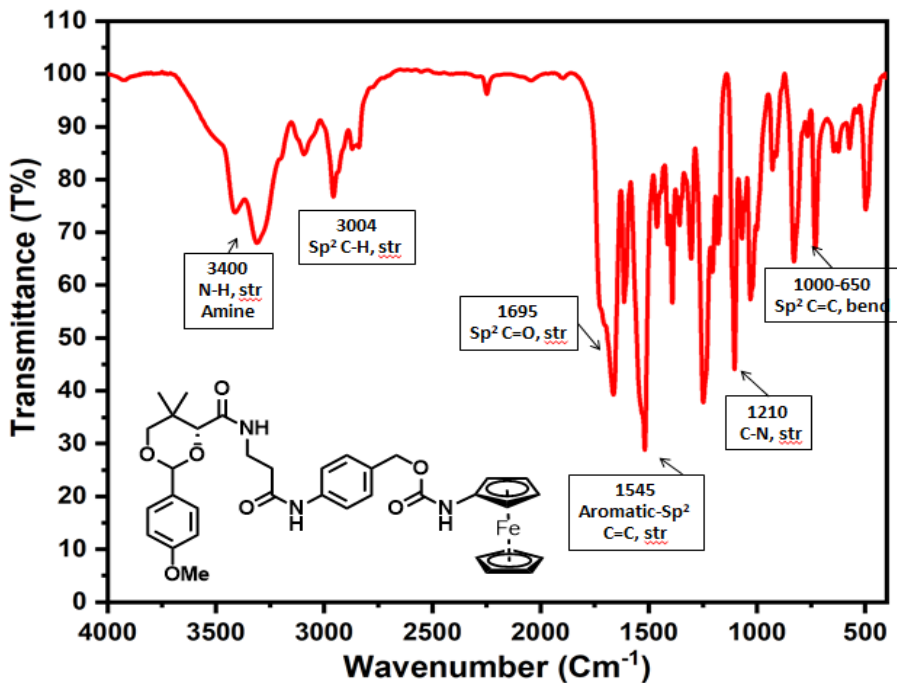
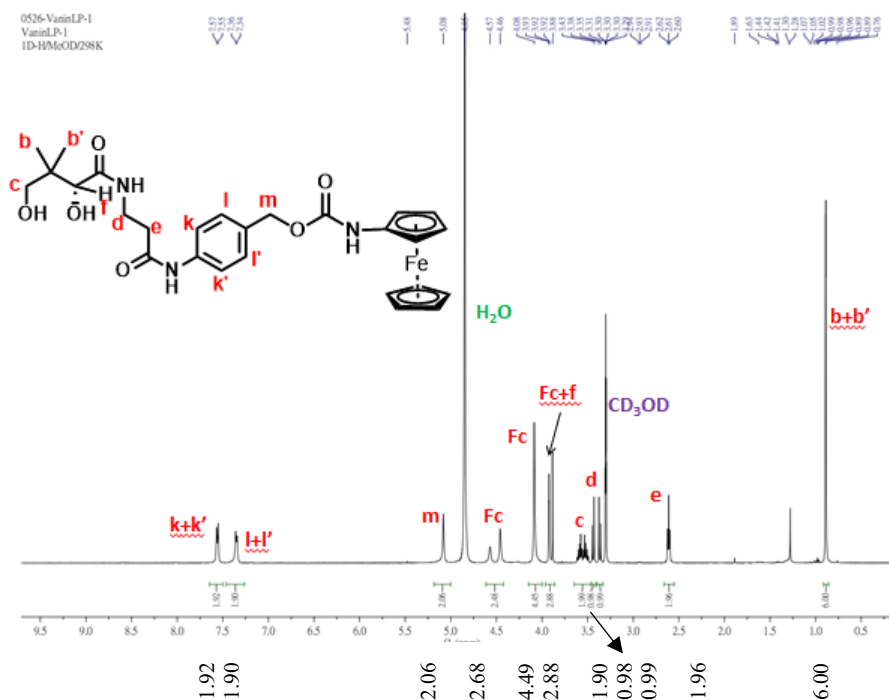


Fig. 3.5. FT-IR spectrum of compound 6 [12].

The functional group composition of compound 6 was verified by Fourier-Transform Infrared (FT-IR) spectroscopy, which displayed all the expected characteristic absorption bands. In the high-frequency region, a broad band centered at  $3400\text{ cm}^{-1}$  confirmed the presence of N-H stretching vibrations from the amide and carbamate groups, while a peak at  $3004\text{ cm}^{-1}$  corresponded to aromatic C-H stretching. Crucially, a strong absorption at  $1695\text{ cm}^{-1}$  was assigned to the CO stretching of the carbonyl groups, providing clear evidence for the newly formed carbamate linkage. The presence of aromatic rings was further supported by C=C stretching and bending vibrations around  $1545\text{ cm}^{-1}$  and in the  $1000 - 650\text{ cm}^{-1}$  region, respectively. A C-N stretching band was also identified at  $1210\text{ cm}^{-1}$ . Collectively, these spectral data are fully consistent with the proposed structure, confirming the successful incorporation of all intended functional moieties in compound 6.

The synthesis concluded with the final deprotection step to yield the target probe, VaninLP. The acetal protecting group of compound 6 was successfully removed using 80 % aqueous acetic acid, affording VaninLP as a yellow crystalline solid with a 35 % yield. The structural integrity and purity of this final compound were unequivocally established through a comprehensive analysis by  $^1\text{H NMR}$ , FT-IR, and ESI-Mass Spectrometry.



**Fig. 3.6.**  $^1\text{H}$  NMR spectrum of compound – VaninLP.  $^1\text{H}$  NMR (500 MHz, MeOD)  $\delta$  7.56 (d,  $J$  = 8.2 Hz, 2H), 7.34 (d,  $J$  = 7.8 Hz, 2H), 5.08 (s, 2H), 4.52 (s, 2H), 4.06 (d,  $J$  = 70.3 Hz, 6H), 3.88 (s, 2H), 3.71 – 3.46 (m, 2H), 3.44 (d,  $J$  = 10.9 Hz, 1H), 3.37 (d,  $J$  = 10.9 Hz, 1H), 3.30 (dt,  $J$  = 3.2, 1.6 Hz, 4H), 2.61 (t,  $J$  = 6.5 Hz, 2H), 0.89 (d,  $J$  = 1.0 Hz, 6H) [12].

The spectroscopic data provided definitive proof that the deprotection reaction was successful. In the  $^1\text{H}$  NMR spectrum (Fig. 3.6), the most critical observation was the complete disappearance of the signals previously assigned to the 4-methoxybenzylidene protecting group, including the characteristic acetal proton ('g') and aromatic protons ('i+i', 'j+j'). Complementing this finding, the FT-IR spectrum (Fig. 3.7) showed the appearance of a new, strong, and broad absorption band centered at  $3450\text{ cm}^{-1}$ , which is characteristic of O-H stretching from the newly formed diol. Both NMR and IR data confirmed that the rest of the molecules framework remained perfectly intact during the reaction. Most importantly, the key components, the ferrocene reporter and the carbamate linker, displayed their expected characteristic signals, such as the ferrocene protons at 4.0 – 4.8 ppm in the NMR and the C=O stretch at  $1695\text{ cm}^{-1}$  in the IR.

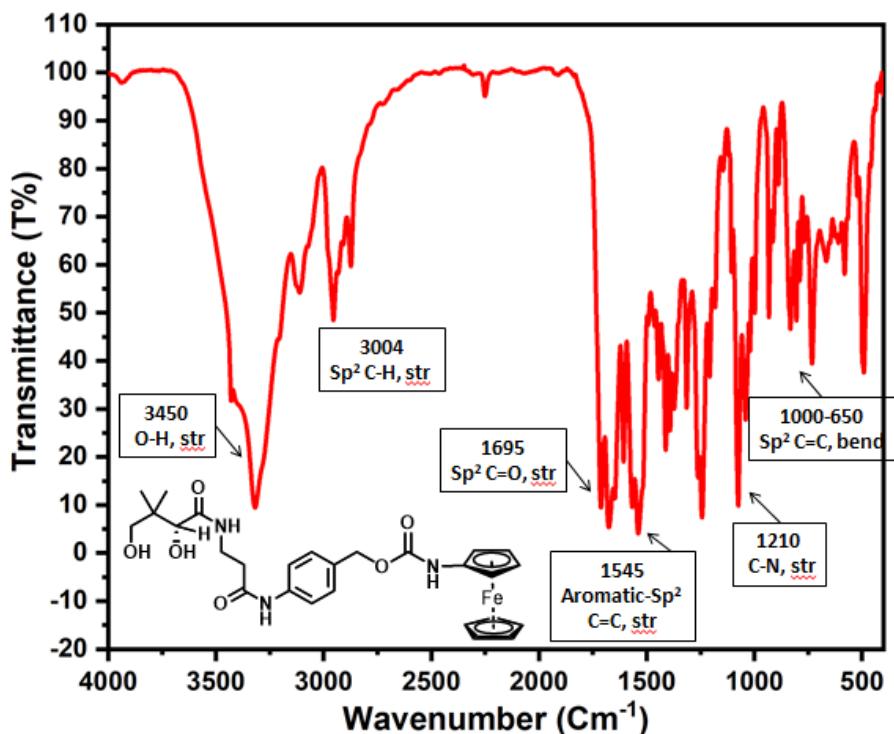
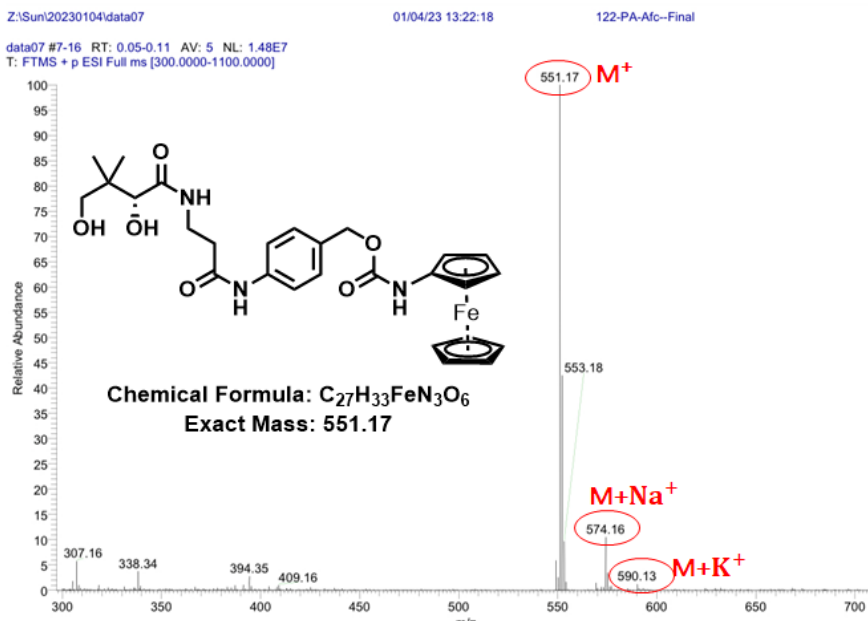


Fig. 3.7. FT-IR spectrum of compound – VaninLP [12].

Finally, Electrospray Ionization Mass Spectrometry (ESI-MS) was used to confirm the precise molecular weight and formula of the VaninLP probe (Fig. 3.8). The mass spectrum featured a prominent molecular ion peak  $[M]^+$  at  $m/z$  551.17, which is in excellent agreement with the calculated exact mass for the proposed formula,  $C_{27}H_{33}FeN_3O_6$ . The assignment was further corroborated by the presence of characteristic sodium ( $[M+Na]^+$  at  $m/z$  574.16) and potassium ( $[M+K]^+$  at  $m/z$  590.13) adducts, providing definitive confirmation of the final products identity.



**Fig. 3.8.** Mass spectrum of compound – VaninLP [12].

## 3.2. Analytical performance of VaninLP

### 3.2.1. Optimization of analytical conditions for VaninLP

The performance of an electrochemical biosensor is highly sensitive to assay conditions like pH and co-solvent concentration. Therefore, we optimized both the pH and the percentage of DMSO to maximize the signal response for pantetheinase detection. To do this, the electrochemical performance of the VaninLP probe was tested across a range of pH values in the presence of 25 ng/mL pantetheinase and 0.5 % DMSO (v/v), as shown in Figures Fig. 3.9A and Fig. 3.9B. The investigation revealed that the highest electrochemical current was achieved at pH 7.0 using a 0.5 % DMSO concentration. Accordingly, a 0.1 M HEPES buffer at pH 7.0 containing 0.5 % DMSO was selected as the optimal supporting electrolyte for all subsequent experiments.

First, the optimal concentration of whole blood for the assay was determined. We found that increasing the blood volume beyond a 50 % (v/v) dilution did not improve the electrochemical signal. This is likely because higher concentrations of whole blood introduce excess non-conductive components that can interfere with the electrolyte solution and reduce its conductivity. Therefore, a 50 % (v/v) blood sample was selected to ensure a

strong sample signal while maintaining the ideal electrochemical environment.

Next, we determined the optimal incubation time for the enzymatic reaction. A solution containing 50  $\mu\text{M}$  of the VaninLP probe and 25 ng/mL of pantetheinase in the optimized HEPES/DMSO buffer was monitored for 120 min. using DPV (Fig. 3.9C). The results showed that the electrochemical signal increased steadily from the start of the reaction and reached AF maximum peak at 30 minutes, after which the signal gradually declined. Based on this, an incubation time of 30 minutes was chosen for all subsequent experiments to ensure maximum signal generation.

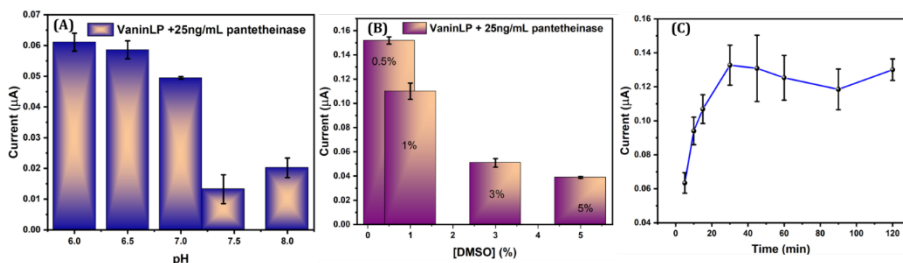


**Fig. 3.9.** Optimization of the analytical conditions for the VaninLP probe. The plots show the dependence of the electrochemical signal on (A) solution pH and (B) DMSO concentration. (C) A time-course plot illustrates the signal generation over 120 minutes. All measurements were conducted in a DMSO/HEPES buffer [12].

### 3.2.2 Characterization of the VaninLP probe for the electrochemical sensing of pantetheinase

To begin, we characterized the electrochemical response of the VaninLP probe to pantetheinase activity. We used CV to compare the probes redox profile in its initial, inactive state versus its state after enzymatic reaction (Fig. 3.10A). The VaninLP probe demonstrated a clear electrochemical switching mechanism. In its initial, inactive state, the probe produced a single sharp redox signal at +0.17 V (Fig. 3.10A, curve a). Upon activation by pantetheinase, this original signal was nearly extinguished, and a new, prominent redox couple emerged at -0.08 V (Fig. 3.10A, curve b). This new signal at -0.08 V served as definitive proof of the probes activation, as it was identical to the redox potential of the pure AF reporter molecule, shown for comparison in Fig. 3.10A (curve c) [160]. This observed switch in the redox

potential is therefore characteristic of the reversible, one-electron transfer of the ferrocene/ferrocenium (Fc/Fc<sup>+</sup>) redox couple [161], [162], [163], [164].

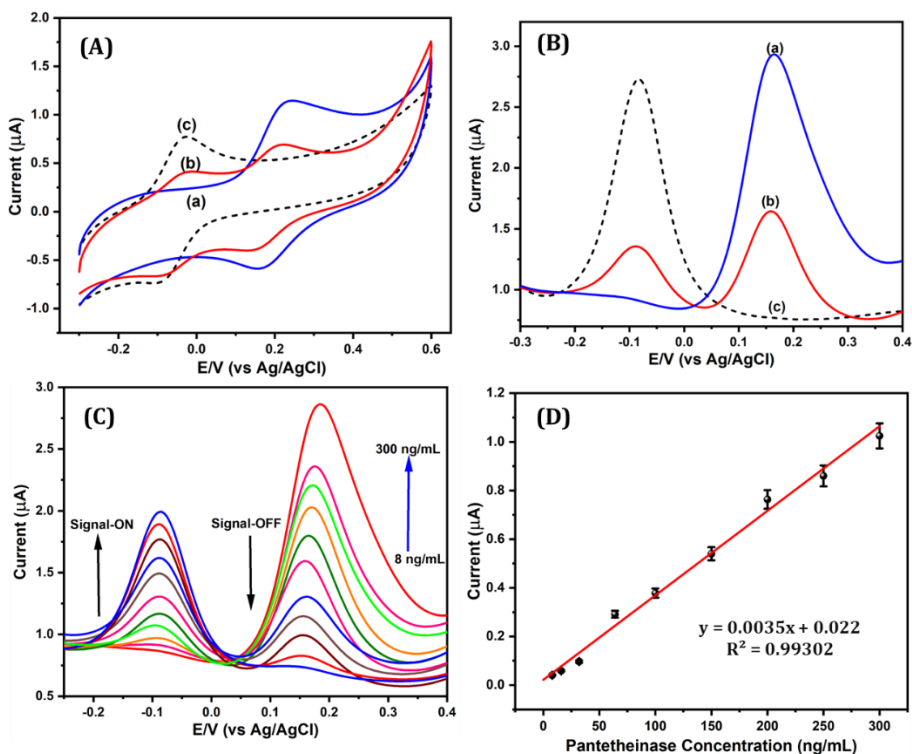
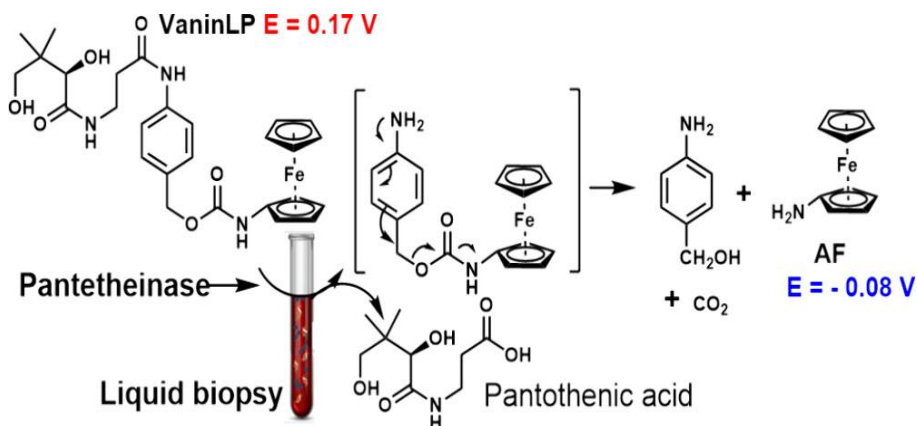


**Fig. 3.10.** Electrochemical characterization of the VaninLP probe. (A, B) The probes response to 120 ng/mL pantetheinase as measured by both (A) CV and (B) DPV. Each plot compares the probe alone (a), the probe with enzyme (b), and the pure AF reporter for reference (c). (C) A DPV dose-response curve showing the signal from 50 μM VaninLP with increasing concentrations of pantetheinase (8 – 300 ng/mL). (D) The corresponding calibration plot derived from the data in (C). All measurements were conducted in a DMSO/HEPES buffer (pH 7.0) at 37 °C [12].

Then we used DPV to analyze the probes signal response (Fig. 3.10B). In the absence of the enzyme, the inactive VaninLP probe produces a single, clear oxidation peak at +0.17 V (Fig. 3.10B curve a). When pantetheinase was added, the probe responded with a clear signal switch. The original oxidation peak at +0.17 V decreased significantly, while a new peak simultaneously appeared at a lower potential of -0.08 V (Fig. 3.10B, curve b). The addition of pantetheinase caused a clear transformation of the electrochemical signal. The initial peak at +0.17 V was greatly diminished, and in its place, a new

oxidation peak emerged at  $-0.08$  V (Fig. 3.10B, curve b). This new oxidation peak at  $-0.08$  V was a perfect match for the signal produced by the pure AF reporter (Fig. 3.10B, curve c). This finding confirms the identity of the released reporter and validates the results previously observed with cyclic voltammetry [163], [164]. These results strongly support the proposed self-immolative mechanism. The pantetheinase-catalyzed reaction cleaves the VaninLP probe to release the AF reporter. As this released reporter is an electron-rich species, it is more easily oxidized, which fully explains the appearance of the new signal at a much lower potential (Scheme 2).

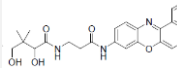
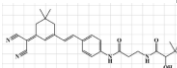
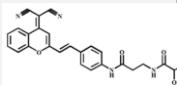
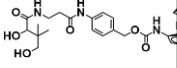


**Scheme 2.** Schematic illustration of the detection mechanism for pantetheinase using the VaninLP probe [12].

To see how well the probe could detect different amounts of the enzyme, we set up a dose-response experiment. A solution of  $50$   $\mu\text{M}$  VaninLP was incubated with a range of Vanin-1 concentrations employing the previously established optimal conditions and recorded the resulting current using DPV (Fig. 3.10C). As the pantetheinase concentration increased from  $8$   $\text{ng/mL}$  to  $300$   $\text{ng/mL}$ , the resulting anodic current from the AF reporter ( $I_{pa}$ ) showed a clear linear increase. Correspondingly, the signal from the original, uncleaved VaninLP probe decreased, confirming the probes ratiometric behavior. Plotting the anodic peak current ( $I_{pa}$ ) at  $-0.08$  V against the pantetheinase concentration revealed a strong linear relationship across the range of  $8$   $\text{ng/mL}$  to  $300$   $\text{ng/mL}$  (Fig. 3.10D). Based on the calibration data, the limit of detection (LOD) for the assay was calculated to be  $2.47$   $\text{ng/mL}$  (using the  $3\sigma/\text{slope}$  method). Notably, we believe this work represents the first electrochemical method developed for monitoring pantetheinase activity that provides a direct, digital signal readout. Furthermore, the VaninLP probe demonstrates a highly competitive analytical performance. Its calculated LOD ( $2.47$   $\text{ng/mL}$ ) is

comparable to or surpassing recently published methods optical methods, which have published LODs of  $1.5 \times 10^{-4}$  U/mg, 4.7 ng/mL, 0.37 ng/mL, and 0.69 ng/mL, respectively (Table 2). In summary, our VaninLP probe successfully enables the quantitative tracking of the direct quantification of pantetheinase activity. Furthermore, its electrochemical nature makes it highly suitable for miniaturization, highlighting its potential for development into a next-generation point-of-care sensing system.

**Table 2.** Comparison of VaninLP with other assays for pantetheinase activity [12].

Method	Assay time	Merits	Limitations	LOD	Real sample	$K_m$	Reference
ELISA	1hr	Highly sensitive, specific, and reproducible	Time-consuming since it needs specialised chemicals, a specialised apparatus to transform the signal, and multiple washing procedures.	-	Serum and urine	-	[165]
Colorimetry	30 min	Extremely easy to use, economical, and sensitive	Lack of reusability, other interferences include bubbles in the sample cells or tubes, turbidity of the sample, and sample color	$1.5 \times 10^{-4}$ U/mg	-	28 $\mu$ M	[166]
Fluorescence-1 CV-PA 	60 min	Both in vitro and in vivo imaging, highly sensitive and selective.	Not suitable for turbid samples and necessitates the use of an additional device to convert the optical signal to a digital signal.	4.7 ng/mL	Blood serum	78 $\mu$ M	[167]
Fluorescence-2 TMN-PA 	60 min			0.37 ng/mL	Cells and in vivo imaging	0.937 $\mu$ M	[168]
Fluorescence-3 DCM-PA 	40 min			0.69 ng/mL	Cells and in vivo imaging	3.356 $\mu$ M	[169]
Electrochemical: VaninLP 	30 min	Rapid, simple, sensitive, selective, in situ analysis in live cells	Also depends on 0.5% organic solvent	2.47 ng/mL	Whole blood, urine, and FBS	2.38 $\mu$ M	This work

### 3.2.3 Characterization of the kinetic profile and selectivity of the VaninLP

The selectivity of the VaninLP probe was subsequently investigated to ensure its response was specific to pantetheinase and not affected by other common biological molecules. To do this, we tested for cross-reactivity by incubating the probe with a wide panel of potentially interfering species typically found in liquid biopsy specimens. This comprehensive panel included several categories of substances: inorganic salts (copper chloride, magnesium chloride, ferrous chloride, calcium chloride), common metabolites and antioxidants (ascorbic acid, dopamine, uric acid, L-cysteine, glutathione, glucose, creatine, urea, H<sub>2</sub>O<sub>2</sub>), the substrate precursor calcium pantothenate, a wide range of amino acids (valine, phenylalanine, tryptophan, asparagine, threonine, sarcosine, alanine, lysine, glycine, proline, and arginine) and other potentially cross-reactive enzymes (gamma-glutamyl transferase, esterase, and leucine aminopeptidase). As shown in Fig. 3.11, none of the potentially interfering species induced an electrochemical signal at -0.08 V when incubated with the VaninLP probe. This result demonstrates the high selectivity of our probe, confirming that the signal at -0.08 V is generated specifically by the activity of pantetheinase. To determine the probes affinity for the enzyme, we performed kinetic studies (Fig. 3.11 B – D). From these experiments, the Michaelis-Menten constant ( $K_m$ ) for VaninLP was calculated to be 2.38  $\mu$ M, with an apparent maximum velocity ( $V_{max}$ ) of 1.25 nM/min/ng. This calculated  $K_m$  value indicates a strong binding affinity between VaninLP and pantetheinase. As shown in Table 2, this affinity is comparable to or greater than (i.e., has a lower  $K_m$  than) most previously reported chromogenic probes and other known substrates for the enzyme. To confirm the probes specificity, we evaluated its response against a wide range of common biological molecules. The results (Fig. 3.11A) demonstrate that the VaninLP probe is highly selective, responding only to pantetheinase and not to any of the potential interfering species tested. To confirm the probes specificity, we tested its cross-reactivity against a comprehensive panel of substances typically found in biological specimens. This diverse panel included several categories of potential interferents, starting with inorganic salts like copper, magnesium, and ferrous chloride. We also tested against common metabolites and antioxidants such as ascorbic acid, dopamine, uric acid, L-cysteine, and glutathione, as well as glucose, creatine, urea, and H<sub>2</sub>O<sub>2</sub>. To ensure specificity against its own precursor, calcium pantothenate was included. Finally, the probe was challenged with a wide range of amino acids

(including valine, lysine, and arginine) and other potentially cross-reactive enzymes like gamma-glutamyl transferase, esterase, and leucine aminopeptidase.

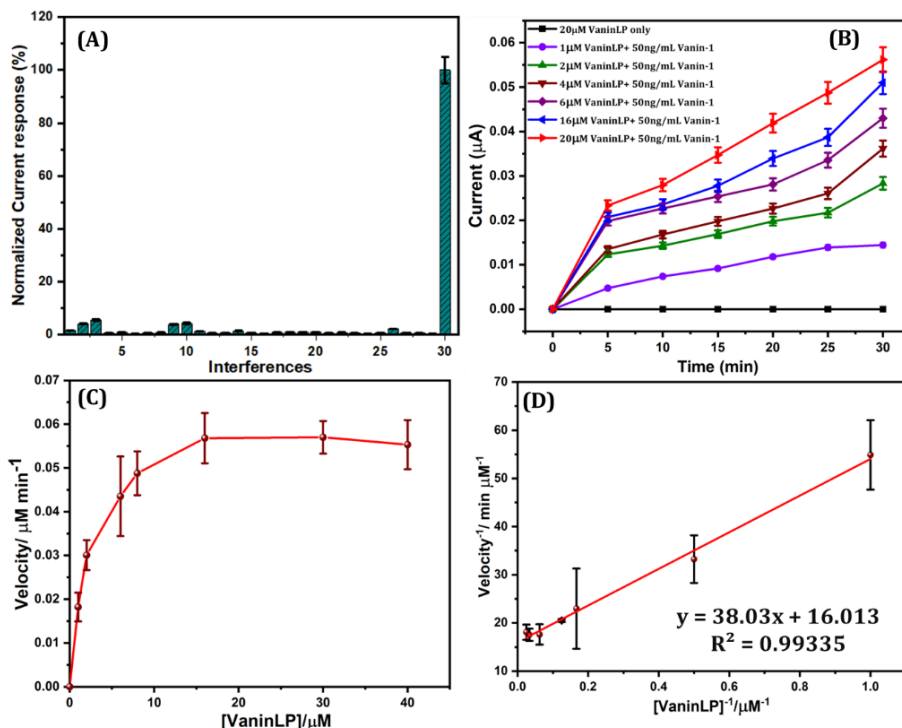


**Fig. 3.11.** Selectivity and kinetic analysis of the VaninLP. (A) A selectivity assay showing the DPV signal of the VaninLP probe (50 µM) in the presence of 30 different biological species. A significant response is observed only for pantetheinase (30), demonstrating the probes high specificity (From right to left: 1. ascorbic acid, 2. dopamine, 3. uric acid, 4.L-cysteine, 5. glutathione, 6. glucose, 7. creatine, 8. urea, 9. copper chloride, 10. valine, 11. phenylalanine, 12. tryptophan, 13. asparagine, 14. threonine, 15. sarcosine, 16. calcium pantathienate, 17. alanine, 18. magnesium chloride, 19. lysine, 20. ferrous chloride, 21. glycine, 22. proline, 23. arginine, 25. calcium chloride, 26. GGT, 27. esterase, 28. leucine aminopeptidase, 29. H<sub>2</sub>O<sub>2</sub>, 30. pantetheinase respectively). (B) Kinetic curves showing the change in current over time at various probe concentrations (1 – 20 µM/mL), both with and without pantetheinase. (C) The Michaelis-Menten plot, showing reaction rate versus VaninLP concentration. (D) The corresponding Lineweaver-Burk (double reciprocal) plot [12].

### 3.3 Detection of pantetheinase activity in biological samples

#### 3.3.1. Quantitative analysis of the pantetheinase activity of tumor cell surfaces

Pantetheinase is a key ectoenzyme found on the surface of various tumor cells and is also recognized as a valuable biomarker for diagnosing kidney injury. Furthermore, it is implicated in several pathological processes, including the damage of the epithelial barrier and the proliferation and spread of tumor cells [170], [171]. Therefore, the ability to quantitatively measure pantetheinase activity could be a valuable tool for assessing the effectiveness of tumor treatments. As a crucial first step, we needed to ensure our probe was not itself toxic to cells. To this end, we performed a standard MTT assay to evaluate the cytotoxicity of VaninLP using a HepG2 human liver cancer cell line. The VaninLP probe demonstrated excellent biocompatibility. Results from the MTT assay (Fig. 3.12) show that after a 6-hour incubation with a high concentration of the probe (50  $\mu$ M), over 94 % of HepG2 cells remained viable. This confirms that VaninLP is a suitable tool for analyzing live cells without inducing significant toxicity.

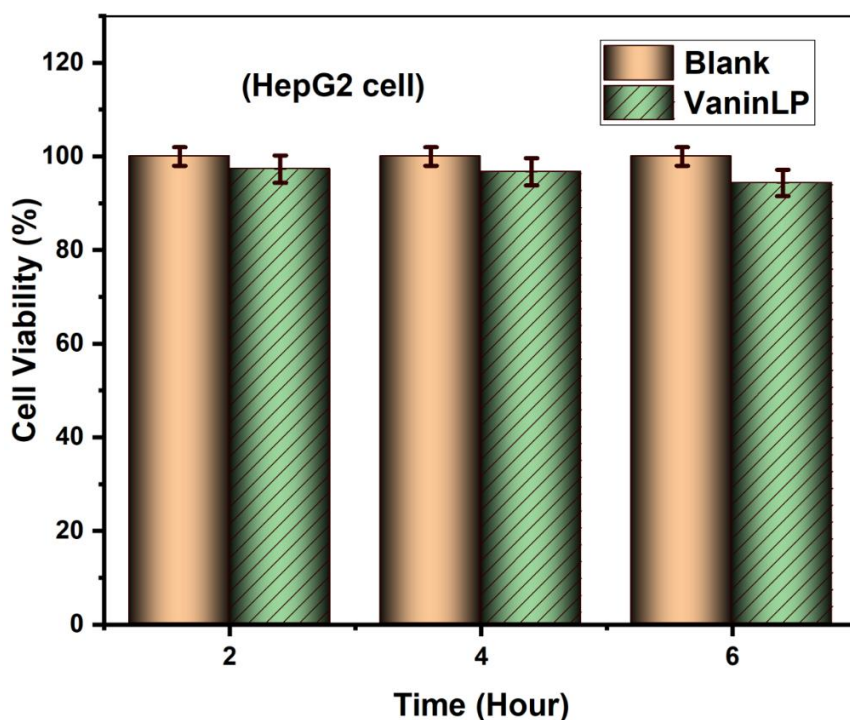


**Fig. 3.12.** Cell viability of HepG2 cells following treatment with and without the VaninLP probe [12].

Then we used DPV to detect pantetheinase activity directly on live HepG2 cells. While control cells alone showed no signal, cells incubated with the VaninLP probe for 5 hours generated a clear oxidation peak at -0.08 V (Fig. 3.14B). We quantified this signal using our calibration plot (Fig. 3.13), determining the activity was equivalent to 3.36 ng/mL of pantetheinase (Table 3).

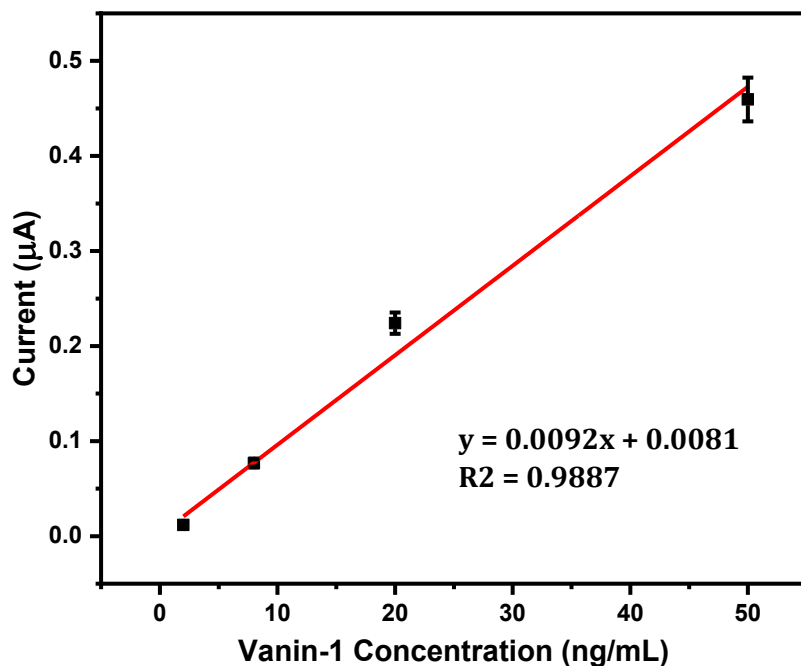


**Fig. 3.13.** Calibration plot used for the quantification of pantetheinase activity from HepG2 cells. The plot shows the DPV current response versus pantetheinase concentration after a 5 – hour incubation [12].

To validate our method in a complex biological sample, we ran a spiking experiment. We added known concentrations of pantetheinase (1 and 2 ng/mL) to assay mixtures already containing HepG2 cells. The total measured activities were 4.32 ng/mL and 5.34 ng/mL, respectively, confirming the probes ability to detect added enzyme (Fig. 3.14B, curves c, d). The results from this spiking experiment demonstrated the high accuracy of our method. The measured activity values were all within 2.0 % error of the expected values, confirming that the VaninLP probe can reliably quantify pantetheinase activity directly in living cells (Fig. 3.14A). Our platform successfully demonstrates the direct quantification of pantetheinase activity on the cell surface. Because pantetheinase is an important anticancer drug target, this

method ability to immediately detect changes in its activity makes it a promising tool for screening new therapeutic inhibitors.

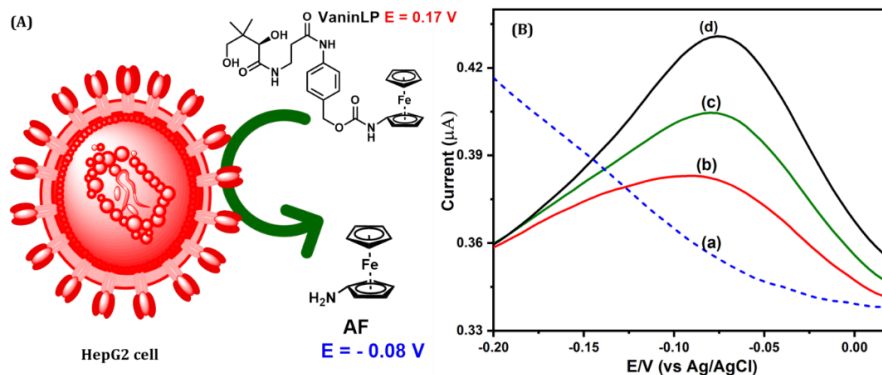


**Fig. 3.14.** Live-cell detection of pantetheinase activity. (A) Schematic illustration of the VaninLP probe profiling pantetheinase on the surface of HepG2 cells. (B) Corresponding DPV results showing the signal from control cells (a), the detection of endogenous enzyme activity (b), and the response to spiked amounts of pantetheinase (c, d) [12].

**Table 3.** Quantification of Pantetheinase in Spiked HepG2 Cell Samples [12].

Real samples	Spiked pantetheinase (ng/mL)	Measured current ( $\mu\text{A}$ )	Measured Pantetheinase (ng/mL)*	Percent error (%)**
<b>HepG2 cells</b>				
Cell: Probe + HEPES	-	0.039 $\pm$ 0.02	3.36 $\pm$ 0.05	-
Cell: Probe + HEPES + pantetheinase spike-1	1.00	0.048 $\pm$ 0.12	4.34 $\pm$ 0.04	2
Cell: Probe + HEPES + pantetheinase spike-2	2.00	0.057 $\pm$ 0.04	5.32 $\pm$ 0.03	2

\*Reported pantetheinase values were adjusted according to the dilution factor to reflect pantetheinase values in HepG2 cell samples.

\*\*Percent error (%) =  $\frac{\text{Measured pantetheinase value with spike (observed)} - \text{pantetheinase value with spike (theoretical)}}{\text{pantetheinase spike value}} \times 100$

### 3.3.2. Direct real-time quantification of pantetheinase activity in NBCS

Given that pantetheinase activity is known to be present in serum [168], we next sought to validate our probes performance in a similarly complex biological matrix. Based on the excellent selectivity demonstrated by VaninLP in our interference studies, we applied our method for the direct measurement of pantetheinase activity in real NBCS samples. As a baseline control, a sample of NBCS was first analyzed by itself. After a 30 – min. incubation at 37 °C, no significant current was detected at the -0.08 V potential, as expected (Fig. 3.15A, curve a). In contrast, when NBCS was incubated with the VaninLP probe for 30 minutes, a specific electrochemical signal was generated (Fig. 3.15A, curve b). Using our standard calibration plot (Fig. 3.10D), we quantified this response, determining the pantetheinase activity to be equivalent to 3.2 µg/mL. Significantly, this value is similar to the concentration measured using a conventional fluorescence-based method, which validates the accuracy of our approach [172]. To confirm the signal was enzyme-specific, we added RR6, a selective pantetheinase inhibitor. As expected, the presence of 100 µM RR6 significantly reduced the electrochemical signal from the NBCS and VaninLP mixture (Fig. 3.15A, curve c). The successful inhibition by RR6 does more than just confirm the signals specificity, it also establishes our platform as a powerful tool for screening potential pantetheinase inhibitors directly in serum. In a separate experiment, we further validated the probes quantitative response by spiking serum samples with 0.6 µg/mL and 1.2 µg/mL of pantetheinase. As expected, this resulted in a corresponding increase in the signal at -0.08 V (Fig. 3.15A, curves d, e). Using the standard calibration curve, the total pantetheinase activities in these spiked samples were quantified as 3.82 µg/mL and 4.45 µg/mL, respectively (Table 4). These measurements were in excellent agreement with the expected values, showing a calculation error of less than 4.0 %.

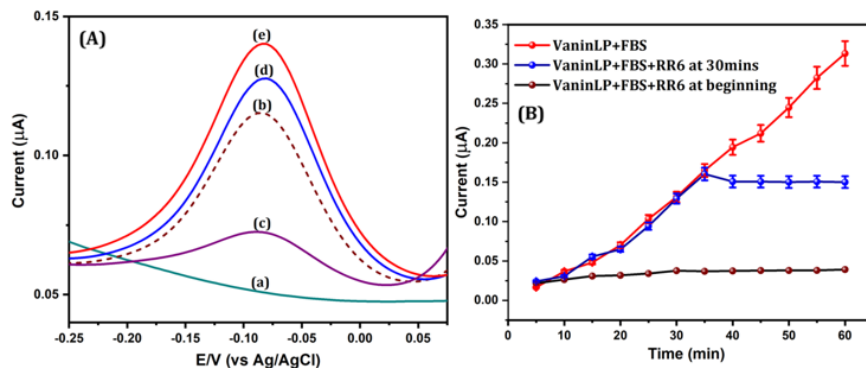


**Fig. 3.15.** Detection and real-time monitoring of pantetheinase activity in Newborn Bovine Calf Serum. (A) DPV curves comparing several conditions: the baseline signal of NBCS alone (a), the detection of endogenous activity after adding the VaninLP probe (b), inhibition of the signal by RR6 (c) and the response to samples spiked with known concentrations of pantetheinase (d, e). (B) Real-time monitoring of the enzymatic reaction. The plot compares the current response over 60 minutes for the standard reaction (no RR6) versus reactions where the inhibitor RR6 was added at the beginning ( $t=0$ ) or after 30 minutes [12].

We next demonstrated the probes ability to track the enzymatic activity of pantetheinase in serum in real time and to track the effects of inhibition (Fig. 3.15B). In the standard reaction, the electrochemical signal was measured every 5 minutes, revealing a clear increase over the 60 min. period as the enzyme acted on the VaninLP probe (red curve). The individual DPV curves from this time course experiment are displayed in Fig. 3.16. To show how inhibition could be monitored, the experiment was repeated with the selective inhibitor, RR6. When RR6 was added at the beginning of the reaction ( $t=0$ ), it completely prevented any signal from being generated (black curve). In a final experiment, when RR6 was added after 30 minutes to an already active reaction, the signal generation immediately ceased and began to decline (Fig. 3.15B, blue curve). These results confirm that our platform can dynamically track both the progression and inhibition of pantetheinase activity.

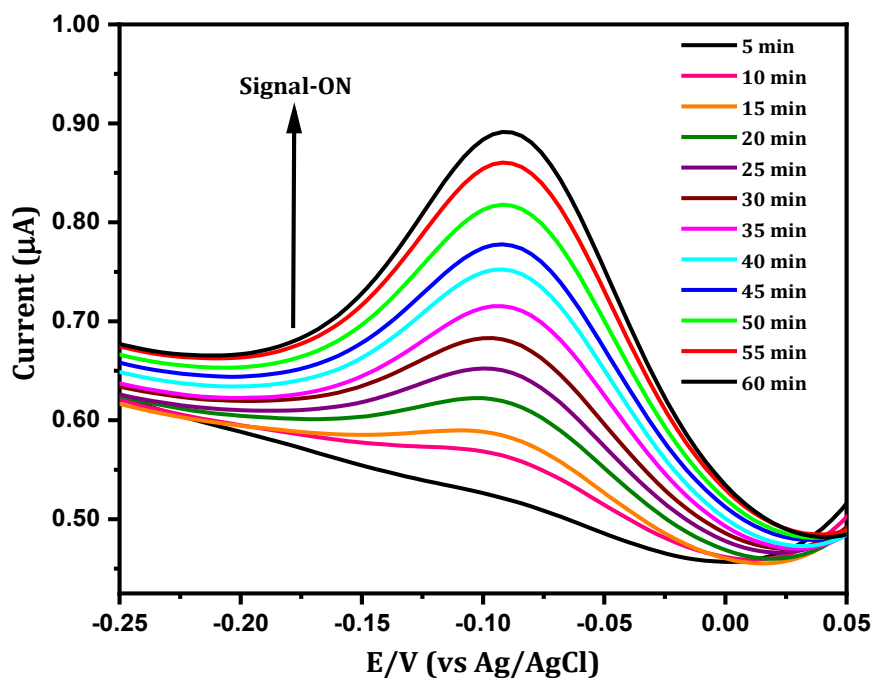


**Fig. 3.16.** Real-time DPV monitoring of endogenous pantetheinase activity in Newborn Bovine Calf Serum [12].

This work successfully demonstrates that the VaninLP probe can quantitatively assess the functional activity of pantetheinase in complex biological samples, such as serum, and monitor it in real time. This capability is particularly significant, because pantetheinase is an important pharmacological target and a biomarker for early-stage kidney damage [170], [173]. Therefore, our platforms ability to dynamically track this activity positions VaninLP as a valuable tool for screening and evaluating new pantetheinase inhibitors.

**Table 4.** Quantification of pantetheinase in spiked NBCS samples [12].

Real samples	Spiked pantetheinase ( $\mu\text{g/mL}$ )	Measured current ( $\mu\text{A}$ )	Measured pantetheinase ( $\mu\text{g/mL}$ )*	Percent error (%)**
NBCS				
NBCS: Probe + HEPES	-	$0.582 \pm 0.02$	$3.20 \pm 0.03$	-
NBCS: Probe + HEPES + pantetheinase spike-1	0.6	$0.690 \pm 0.03$	$3.82 \pm 0.06$	2.87
NBCS: Probe + HEPES + pantetheinase spike-2	1.2	$0.800 \pm 0.01$	$4.45 \pm 0.22$	3.83

\*Reported pantetheinase values were adjusted according to the dilution factor to reflect pantetheinase values in NBCS samples.

\*\*Percent error (%) =  $\frac{\text{Measured pantetheinase value with spike (observed)} - \text{pantetheinase value with spike (theoretical)}}{\text{pantetheinase spike value}} \times 100$

### 3.4. Analysis of endogenous pantetheinase activity in biofluids: whole blood and urine

The presence of atypical pantetheinase concentrations in clinical samples such as blood and urine is directly associated with significant health issues, particularly in oncology. For instance, patients diagnosed with bladder or pancreatic cancer show significantly elevated concentrations of circulating pantetheinase in their plasma and urine relative to healthy individuals controls [174]. Pantetheinase also shows great promise as a biomarker for acute kidney injury. For patients at high risk, a key diagnostic strategy involves monitoring the enzymes activity in their blood and urine. Building on this, we investigated whether our VaninLP probe could meet this need by directly detecting pantetheinase activity in whole blood and urine samples with only minimal pretreatment. The control sample, consisting of 50 % (v/v) whole blood incubated alone for 30 minutes at 37 °C, showed no electrochemical a signal at cathodic potentials, when analyzed by DPV (Fig. 3.17A, curve a). In contrast, when the VaninLP probe was incubated directly with a whole blood sample, it produced a significant current response with a peak potential identical to that of the pure AF reporter (Figure 3.17A, curve b). Using the calibration plot (Fig. 3.10D), we quantified this signal and determined the endogenous pantetheinase activity in the blood to be 314.2 ng/mL. To confirm that the signal was enzyme-specific, the experiment was repeated in the presence of the pantetheinase inhibitor, RR6. As expected, the addition of RR6 to the whole blood and VaninLP mixture effectively suppressed the electrochemical current response (Fig 3.17A, curve c).

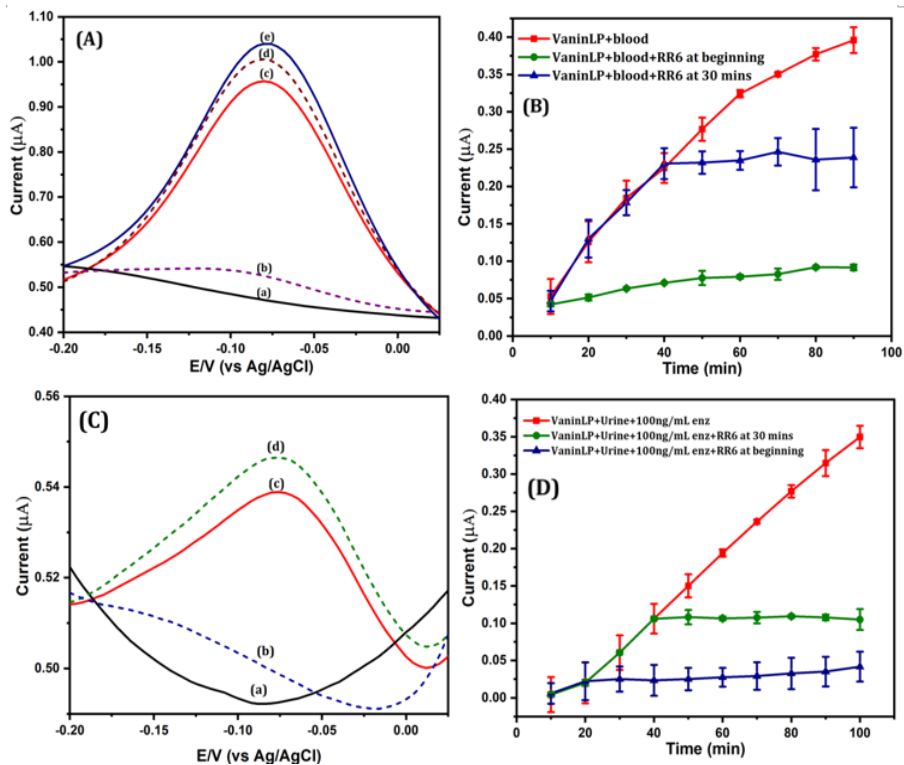


**Fig. 3.17.** Direct detection and real-time monitoring of pantetheinase activity in whole blood and urine. Analysis in whole blood (A, B). (A) DPV curves comparing the electrochemical signal from a control sample (a), the detection of endogenous activity (b), inhibition by RR6 (c), and samples spiked with pantetheinase (d, e). A real-time plot tracking the reaction progress and showing the effect of adding the inhibitor RR6 at the start ( $t=0$ ) or after 30 minutes. Analysis in urine (C, D). (C) DPV curves comparing the signal from a control sample (a), the detection of endogenous activity (b), and samples spiked with pantetheinase (c, d). (D) The corresponding real-time plot showing the reaction progress and the effect of the inhibitor RR6 [12].

To further validate the methods performance in whole blood, we ran a spiking experiment. Adding 30 ng/mL and 36 ng/mL of pantetheinase to the blood and VaninLP mixture resulted in a clear, corresponding increase in the electrochemical signal. By referencing the standard curve, the total pantetheinase activities in these spiked samples were quantified as 344.6 ng/mL and 349.8 ng/mL, respectively (Table 5). These measurements demonstrate high accuracy, with a calculation error of less than 5.0 % relative

to the known spiked amounts. It is generally understood that pantetheinase activity in serum is primarily from GPI-80, a secreted form of the enzyme, with levels in healthy individuals reported to be around 100 ng/mL [175]. However, a significant knowledge gap exists for whole blood, as there are no reports on its total pantetheinase levels, which would include both the secreted enzyme, and the enzyme present on cell surfaces like erythrocytes. In this work, we have successfully developed a method for the direct detection and quantification of pantetheinase in whole blood, eliminating the need for complex serum or plasma separation steps. Our current efforts are now focused on collecting additional blood samples to formally validate the performance of our method against existing analytical techniques.

**Table 5.** Spike and recovery analysis of pantetheinase in whole blood and urine samples [12].

Real samples	Spiked pantetheinase (ng/mL)	Measured current ( $\mu$ A)	Measured pantetheinase (ng/mL)*	Percent error (%)**
<b>Whole blood</b>				
Blood: Probe + HEPES (1:1 (v/v) dilution)	-	0.572 $\pm$ 0.03	314.2 $\pm$ 0.13	-
Blood: Probe + HEPES + pantetheinase spike-1 (1:1)	30.00	0.625 $\pm$ 0.02	344.6 $\pm$ 0.31	1.33
Blood: Probe + HEPES + pantetheinase spike-2 (1:1)	36.00	0.634 $\pm$ 0.11	349.8 $\pm$ 0.30	1.11
<b>Urine</b>				
Urine: Probe + HEPES (1:5 (v/v) dilution)	-	-	-	-
Urine: Probe + HEPES + pantetheinase spike-1 (1:5)	50.00	0.035 $\pm$ 0.04	48.55 $\pm$ 0.02	2.90
Urine: Probe + HEPES + pantetheinase spike-2 (1:5)	55.00	0.039 $\pm$ 0.03	54.3 $\pm$ 0.03	1.27

\*Reported pantetheinase values were adjusted according to the dilution factor to reflect pantetheinase values in whole blood and urine samples.

\*\*Percent error (%) =  $\frac{\text{Measured pantetheinase value with spike (observed)} - \text{pantetheinase value with spike (theoretical)}}{\text{pantetheinase spike value}} \times 100$

We then extended our analysis to 20 % (v/v) urine samples. First, we tested for any endogenous pantetheinase activity. As shown in Fig. 3.17C, neither the urine sample alone (curve a) nor the urine incubated with the VaninLP probe (curve b) produced any significant electrochemical signal. Under normal physiological conditions, pantetheinase levels in urine are typically very low or undetectable. For example, one study reported a median level of just 0.33 (interquartile range 0–2.6) ng/mg creatine. However, these

levels can become significantly elevated in certain pathological states, such as in terminally ill patients [176]. Although endogenous activity was low, spiking urine samples containing the VaninLP probe with 50 ng/mL and 55 ng/mL of pantetheinase produced a distinct current response in the negative potential region, as expected (Fig. 3.17C, curves c–e). Quantification of these spiked urine samples using the calibration curve yielded pantetheinase concentrations of 48.55 ng/mL and 54.3 ng/mL, respectively (Table 5, Fig. 3.18). Collectively, these findings demonstrate that the VaninLP probe can reliably and for the direct measurement of pantetheinase activity even in complex, turbid samples like whole blood and urine. Crucially, the electrochemical signal is highly robust, as the detection peak potential remains stable and is not altered by the sample matrix.

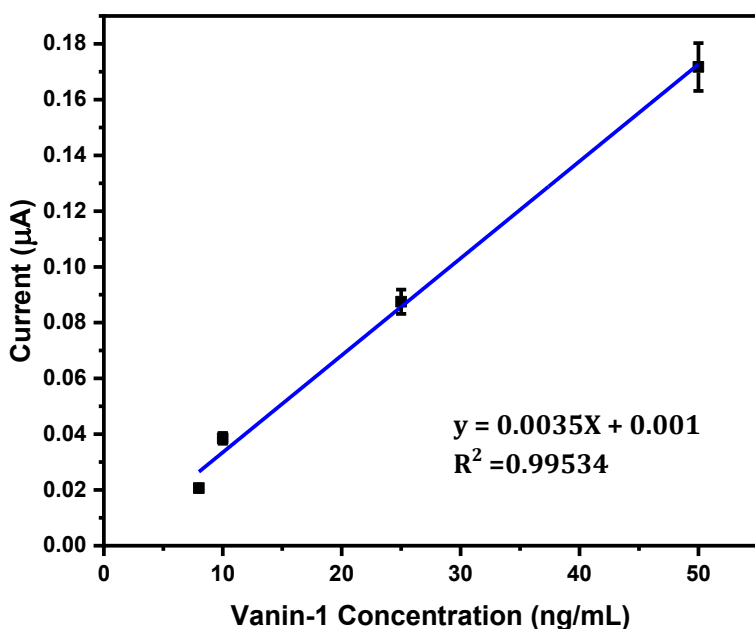


**Fig. 3.18.** Calibration plot used for the quantification of pantetheinase in urine samples. The plot shows the current response versus pantetheinase concentration after a 30 – minutes incubation [12].

We also demonstrated the platforms ability to track pantetheinase activity in real time directly within whole blood samples. To achieve this, VaninLP was incubated with 50 % whole blood under optimal conditions, and the electrochemical response was recorded by DPV every 10 minutes. The resulting kinetic plot is shown in Fig. 3.17B (red curve), with the corresponding individual DPV scans displayed in Fig. 3.19.

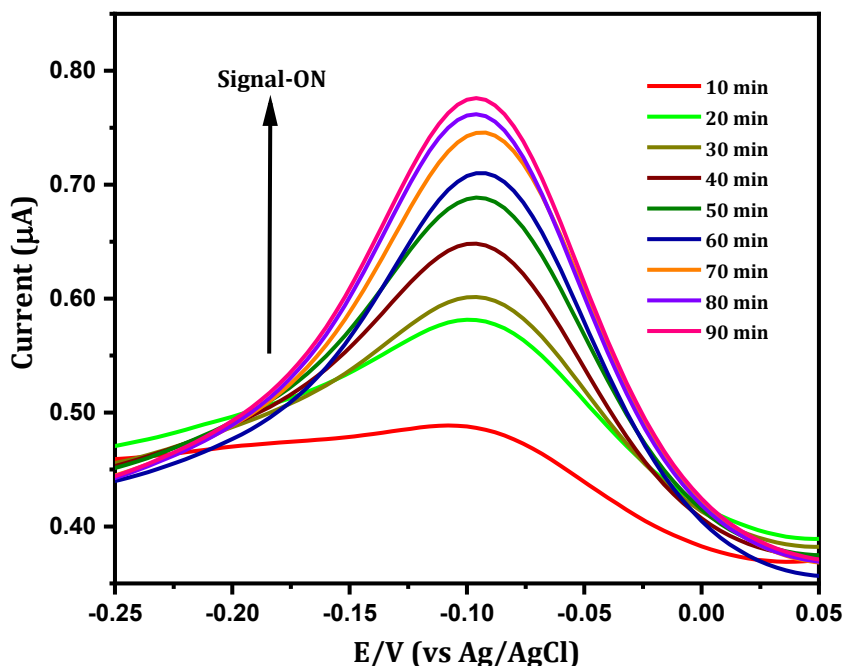


**Fig. 3.19.** Individual DPV scans from the real-time monitoring of pantetheinase activity in whole blood [12].

To demonstrate real-time inhibition in a blood sample, we monitored the reaction in the presence of the inhibitor, RR6, under two different conditions (Figure 3.17B). When RR6 was added at the start of the assay ( $t=0$ ), it completely blocked the enzymatic reaction, and no signal was generated over the entire monitoring period (green curve). In the second case, when RR6 was added to an already active reaction at the 30-min. mark, the signal generation immediately ceased and began to decline (blue curve). We then conducted a parallel set of real-time monitoring experiments in urine, because normal urine contains very low levels of the enzyme, each sample was first spiked with 100 ng/mL of pantetheinase to generate a measurable signal. The standard, uninhibited reaction was then monitored by DPV every 10 minutes, showing the expected signal increase over time (Figure 3.17D, red curve). The individual DPV scans from this experiment are provided in Figure 3.20.

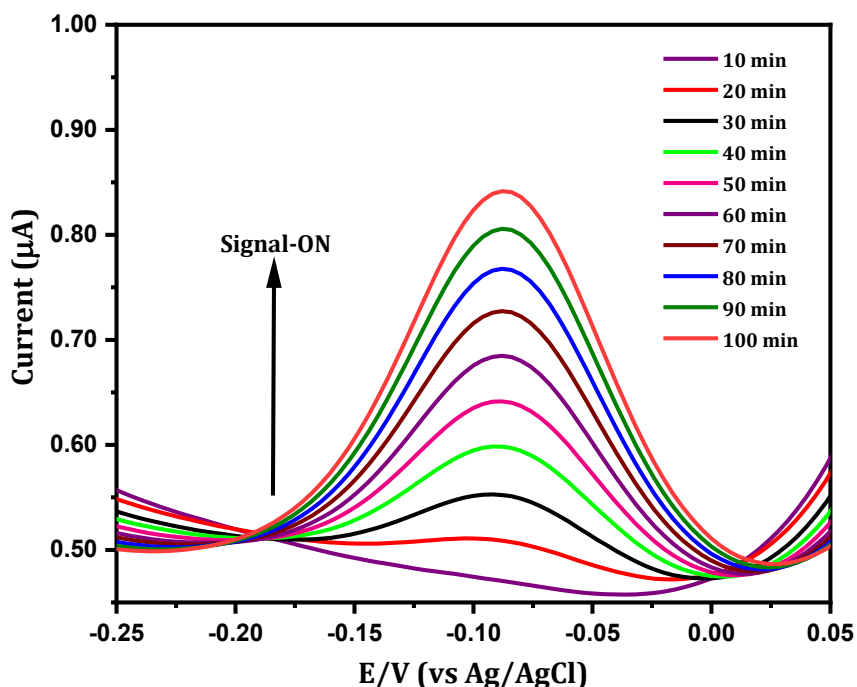


**Fig. 3.20.** DPV scans from the real-time monitoring of pantetheinase activity in spiked urine samples [12].

The inhibition pattern in the spiked urine samples mirrored the results observed in whole blood. When the inhibitor RR6 was added at the start of the reaction ( $t=0$ ), it completely prevented any signal generation (Fig. 4D, blue curve). Likewise, when RR6 was added to an active reaction at the 30-min. mark, the signal immediately began to decrease instead of continuing to rise (Fig. 3.17D, green curve).

The clinical utility of measuring pantetheinase is significant, as abnormal levels in blood or urine can indicate kidney damage and directly correlate with the severity of malaria. According to the World Health Organization, the need for new diagnostic tools for malaria is particularly urgent. In 2021 alone, the disease caused an estimated 247 million cases and 619000 deaths worldwide, with 95 % of this burden falling on the African region.

Tragically, 80 % of these fatalities occurred in children under the age of five, underscoring the critical need for accessible and rapid diagnostic technologies [177]. In many of the regions most affected by these diseases, limited access to clinical facilities creates an urgent need for simple and convenient diagnostic tools for patient monitoring. Current methods for detecting pantetheinase, which rely on color changing reagents, fall short of

this need. They require lab-based equipment to separate serum from whole blood and involve additional sample pretreatment steps, making them slow and impractical for point of care use. Our electrochemical probe, VaninLP, was designed to overcome these specific challenges. In stark contrast, it allows for the direct analysis of whole blood samples, eliminating the need for sample processing and significantly simplifying the detection procedure. By enabling the direct quantification of pantetheinase, our platform has significant potential for managing diseases like kidney injury and malaria, where it can inform dosage decisions, assess treatment efficacy, and monitor for recurrence. Given its quantitative digital output, which surpasses basic analytical procedures, our platform is also a promising candidate for future development into a point-of-care tool for applications such as the post-treatment surveillance of cancer.

### 3.5. Characterization of 3D tumor spheroids and optimization of the ECL system

MCF-7 spheroids were selected as a well-established and easily produced 3D cancer model for this proof of concept study. Following a 5 – day culture period, an initial seeding of 5000 cells reliably formed spherical spheroids with a consistent average diameter of  $565 \pm 8 \mu\text{m}$  (Fig. 3.22A).

To ensure robust signal acquisition, we first optimized the camera exposure time for our ECL imaging experiments. An analysis of ECL intensity versus exposure time revealed that the signal increased linearly up to 15 seconds, after which it plateaued due to detector saturation (Fig. 3.21). Therefore, an exposure time of 15 sec. was selected for all subsequent experiments to achieve the maximum signal to noise ratio without saturation.

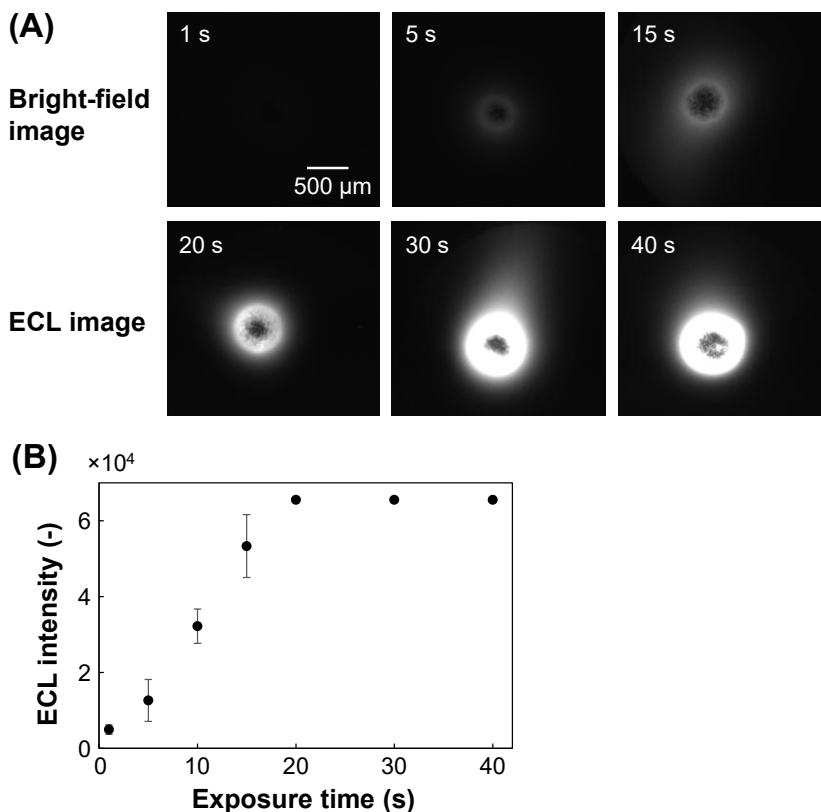


**Fig. 3.21.** Optimization of camera exposure time for ECL imaging of spheroids. (A) Representative ECL images of a 7-day old spheroid (initially seeded with 5000 cells) captured using various exposure times from 1 – 40 s. (B) The corresponding plot of ECL intensity versus exposure time. Data are shown as the mean of three independent experiments ( $n = 3$ ) [109].

### 3.6. Imaging molecular diffusion from 3D spheroids via ECL

#### 3.6.1 Visualization of co-reactant efflux from live 3D spheroids

We then performed ECL imaging on the live spheroids using the  $[\text{Ru}(\text{bpy})_3]^{2+}$  reporter. Interestingly, the resulting signal was not confined to the spheroid itself, but was detected in an area extending approximately 200  $\mu\text{m}$  from its edge (Figure 3.22B, C). This indicates that the signal is generated by biocompounds that are released from the spheroid and act as co-reactants in the surrounding solution. To validate this diffusion based mechanism, we calculated an expected diffusion distance ( $d$ ) of approximately 170  $\mu\text{m}$  (using the formula  $d = \sqrt{2Dt}$  and assuming a diffusion coefficient ( $D$ ) of  $1 \times 10^{-9}$

m<sup>2</sup>/s). This theoretical value is in excellent agreement with our experimental observation. We also noted that within the spheroid, the ECL intensity was lower at the center than at the edge, likely due to diffusion limitations. The ECL images revealed distinct granules of approximately 20 μm in diameter, consistent with the size of individual cells, suggesting our method can resolve single-cell activity at the spheroid surface (Fig. 3.22B). This observation supports a mechanism where [Ru(bpy)<sub>3</sub>]<sup>3+</sup>, generated at the electrode, diffuses to the cells and triggers a catalytic ECL reaction. The lower signal intensity observed at the spheroids center is also consistent with this model, as reagent diffusion into the dense core would be limited.

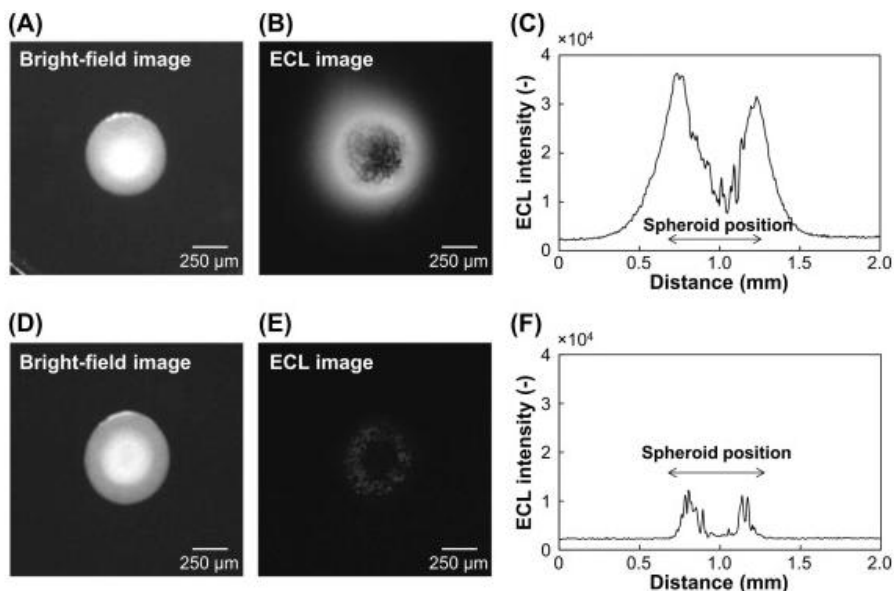


**Fig. 3.22.** Analysis of ECL signal generation in living versus fixed spheroids. Bright-field images (A, D), ECL images (B, E), and corresponding cross-sectional intensity profiles (C, F) are shown for both living and fixed MCF-7 spheroids. Spheroids were cultured for 5 days from an initial seeding number of 5000 cells [109].

As seen in the bright-field image (Fig. 3.22D), the chemically fixed spheroids exhibited subtle changes in both size and morphology when compared to their living counterparts. In stark contrast to the living spheroids, no ECL signal was detected in the area surrounding the fixed spheroid. As a result, the overall ECL intensity was dramatically lower (Fig. 3.22E and Fig. 3.23). To check the integrity of the fixed cells, we stained them with propidium iodide (PI), a dye that binds to DNA (Fig. 3.24). The successful staining confirmed two things: first, that the fixation process made the cell

membranes permeable enough for small molecules like PI to enter, and second, that larger components like DNA were successfully retained inside the cells. Based on these results, we conclude that the absence of an ECL signal from the fixed spheroids is due to the loss or inactivation of the necessary biocompounds. We propose two complementary reasons for this: either the small co-reactant molecules were flushed out of the permeabilized cells during the fixing and washing steps, or they were chemically immobilized by cross-linking with the PFA fixative. Although the overall ECL signal from the fixed spheroids was very low, a faint, granular pattern could still be resolved, although much weaker than the signal from living spheroids (Fig. 3.23). We hypothesize that this residual signal originates from non-diffusive biocompounds (e.g., larger molecules or proteins) that were chemically cross-linked and trapped within the cells by the PFA treatment. In contrast, the majority of the small, diffusive co-reactants were likely washed away during the process, which accounts for the dramatic overall decrease in ECL intensity.

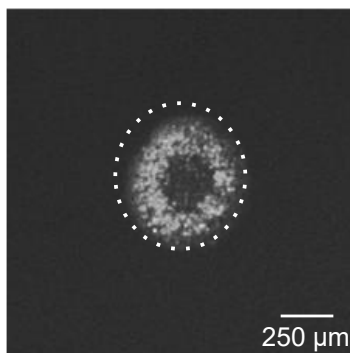


**Fig. 3.23.** Residual ECL activity in a fixed spheroid. A brightness-enhanced ECL image reveals faint, granular signals remaining after chemical fixation, which are attributed to non-diffusive biocompounds. The spheroid boundary is outlined by the white dotted circle [109].

To identify the granular features seen in our ECL images, we performed correlative fluorescence microscopy using propidium iodide (PI), a dye that stains the nuclei of individual cells (Fig. 3.24). The fluorescence image revealed a granular pattern corresponding to single cells, creating a high degree of surface roughness. This pattern was visually identical to the one observed in the ECL images, allowing us to conclude that the ECL granules also represent the activity of individual cells on the spheroid surface.

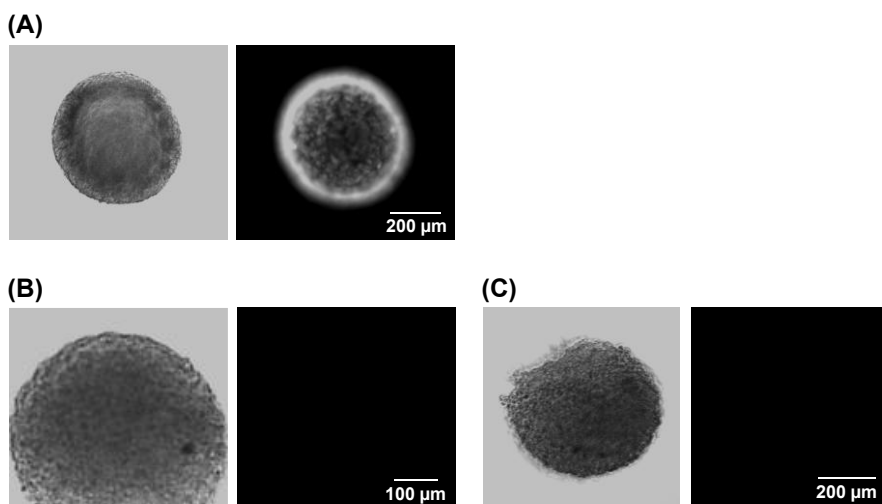


**Fig. 3.24.** Propidium iodide (PI) staining to assess membrane permeability in fixed versus unfixed MCF-7 spheroids. The figure compares phase-contrast (left) and fluorescence (right) images of (A) a spheroid fixed with 4 % paraformaldehyde and (B) an unfixed, living spheroid. The strong PI signal in the fixed spheroid indicates that the fixation process permeabilized the cell membranes, allowing the dye to enter and stain the DNA, while the living spheroid remains unstained [109].

### 3.7. Analysis of co-reactant depletion dynamics

We next investigated the stability of the ECL signal over repeated measurements (Fig. 3.25). The results showed that the ECL intensity from living spheroids gradually decreased with each subsequent imaging cycle (Fig. 3.25A). After seven consecutive measurements, the signal had diminished to a level comparable to that of a fixed, non-viable spheroid. This signal depletion indicates that the pool of available biocompounds is finite, likely because they either diffuse away from the spheroid into the bulk solution or are consumed during the irreversible electrochemical reaction.

It is noted that the variability between spheroid measurements, as indicated by the error bars in Figure 3.25B, is relatively high. This is a consistent feature observed throughout these biological experiments (also see Figs. 3.27B and 3.28B) and is likely due to the inherent biological heterogeneity of 3D cell models. Even when cultured under identical conditions, individual spheroids can exhibit slight differences in size, cell number, and metabolic state, leading to variations in the quantity of

biocompounds released upon electroporation. Therefore, this variability reflects the biological reality of the system rather than a limitation of the measurement techniques precision.

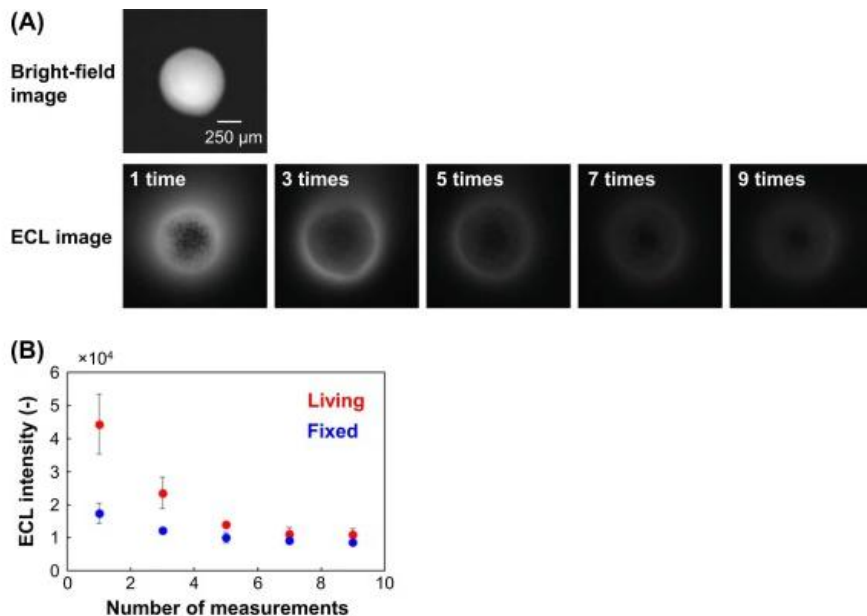


**Fig. 3.25.** ECL signal stability over repeated measurements of a living spheroid. (A) A series of bright-field and ECL images taken during seven consecutive measurements (at 1-minute intervals) of a single 7-day old spheroid, which was grown from an initial 5000 cells.

(B) The corresponding plot shows the decrease in the maximum ECL intensity with each subsequent measurement. Data are presented as the mean of three independent experiments ( $n = 3$ ) [109].

The observation that the ECL signal diminishes with repeated measurements suggests the co-reactants come from a finite, depletable source rather than being continuously secreted. Therefore, it is unlikely that the signal originates from secreted species like ROS or dopamine. Instead, we propose that the co-reactants are intracellular biocompounds that are released through temporary pores created in the cell membrane by the 1.2 V potential, a process known as electroporation. To investigate this signal depletion further, we ran a control experiment using a simple 1 mM GSH solution (Fig. 3.26). We observed an initial drop in ECL intensity, the second measurement was 77 % of the first, but the signal remained stable and constant in all subsequent cycles. These results indicate that the electrode experiences only minor, initial fouling that quickly stops. Since this small, temporary effect cannot explain

the dramatic and sustained signal loss seen with the spheroid (Fig. 3.25B), we attribute that decrease primarily to the depletion of biocompounds as they diffuse away from the spheroid, not to significant electrode fouling.

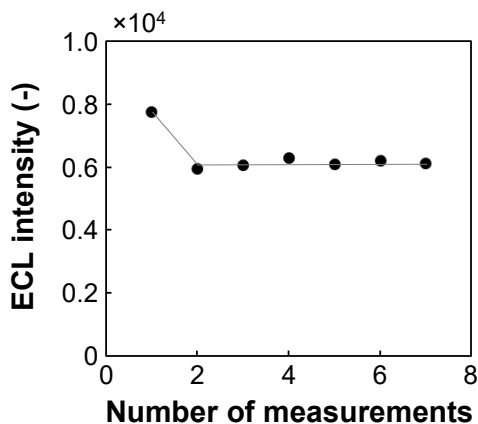


**Fig. 3.26.** ECL signal stability during repeated measurements of a 1 mM GSH solution. The plot shows the change in ECL intensity over consecutive measurement cycles. Each cycle consisted of a 15 sec. potential step and camera exposure, followed by a 1 minute recovery period. The solution contained 1 mM GSH and 5 mM  $[\text{Ru}(\text{bpy})_3]^{2+}$  in PBS [109].

We next investigated how the spheroid culture period affects the ECL signal. As expected, bright-field imaging confirmed that the spheroids grew larger with longer culture times (Fig. 3.27A). A direct correlation was observed between spheroid size and signal strength, as the ECL intensity increased correspondingly (Fig. 3.27A and B). This result suggests that larger, more developed spheroids contain a greater total amount of the diffusive biocompounds required for the reaction.

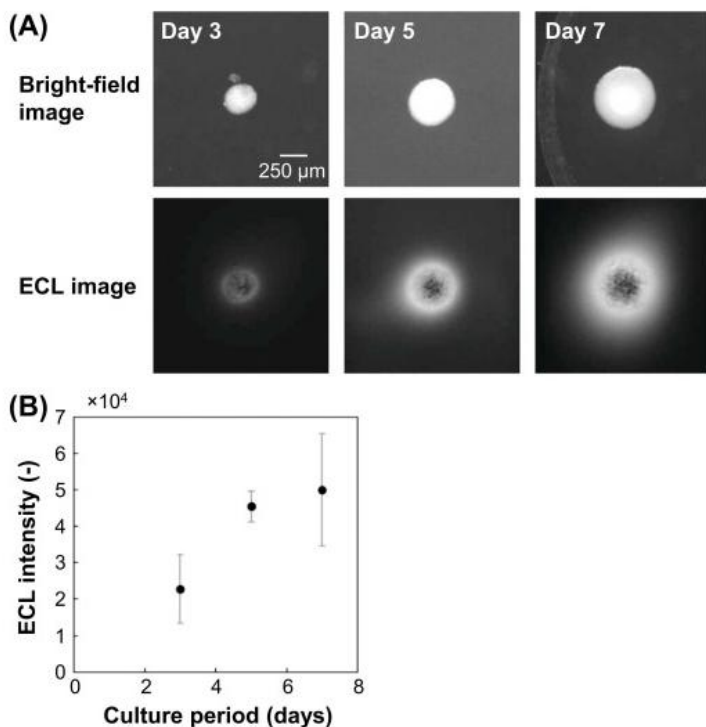


**Fig. 3.27.** Effect of culture period on spheroid growth and ECL signal intensity. (A) Bright-field and ECL images of spheroids (initially seeded with 1000 cells) after being cultured for 3, 5, and 7 days. (B) The corresponding plot shows the increase in maximum ECL intensity as a function of the culture period. Data are presented as the mean of three independent experiments ( $n = 3$ ) [109].

Interestingly, we found that the initial cell seeding number did not significantly affect the final ECL intensity (Figs. 3.28A and B). While the starting number of cells varied, the ultimate signal remained largely the same across the groups. This suggests that the total amount of diffusive biocompounds within a spheroid is primarily determined by the culture period, rather than the initial seeding density.

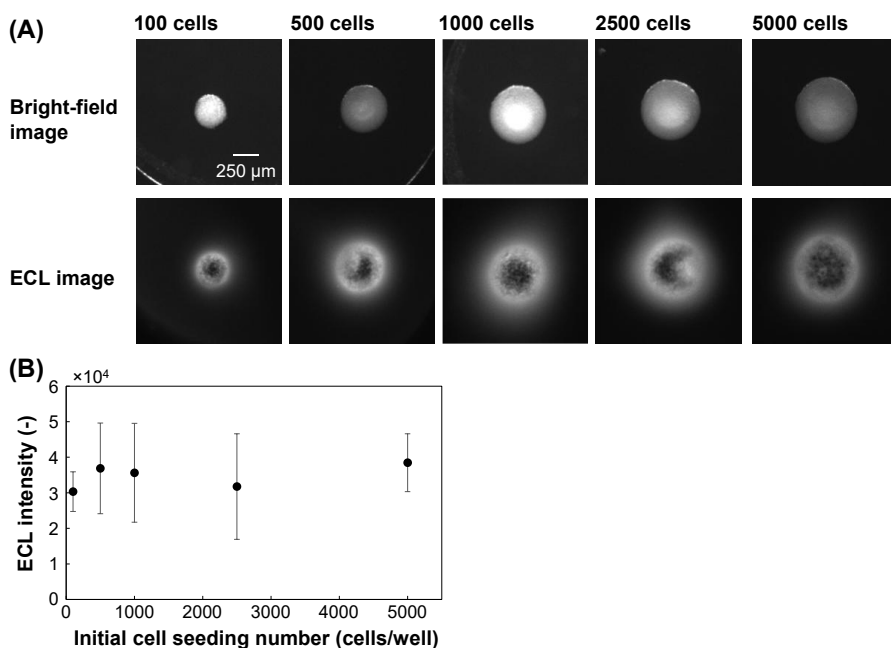


**Fig. 3.28.** Effect of initial cell seeding number on the ECL intensity of living spheroids. (A) Representative bright-field and ECL images of 7 day old spheroids grown from various initial cell numbers (ranging from 100 cells to 5000 cells). (B) The corresponding plot shows the maximum ECL intensity as a function of the initial seeding number. Data are presented as the mean from 4 – 5 independent experiments [109].

### 3.8. Characterizing the endogenous co-reactants

In an attempt to identify the specific biocompounds, we tried a strategy to immobilize them directly onto the electrode surface. This involved placing living spheroids on the electrode and allowing them to dry, with the goal of fixing the leaking co-reactants in place (Fig. 3.29A). However, this method proved unsuccessful. While subsequent ECL imaging did show a faint signal, it was localized only to the edges of the dried spheroids (Figs. 3.29B and C). This indicates that the biocompounds were not sufficiently immobilized on the ITO surface, which prevented any further analysis with this approach. To investigate potential endogenous co-reactants and to determine if quantitative analysis of their concentrations was feasible, calibration processes were performed. Standard solutions of both NADH and GSH were analyzed to generate calibration plots that correlate their respective concentrations with

the measured ECL intensity (Fig. 3.31C and Fig. 3.32C). These calibrations were subsequently used as a basis to estimate the effective concentration of biocompounds being released from the spheroids at the electrode surface.

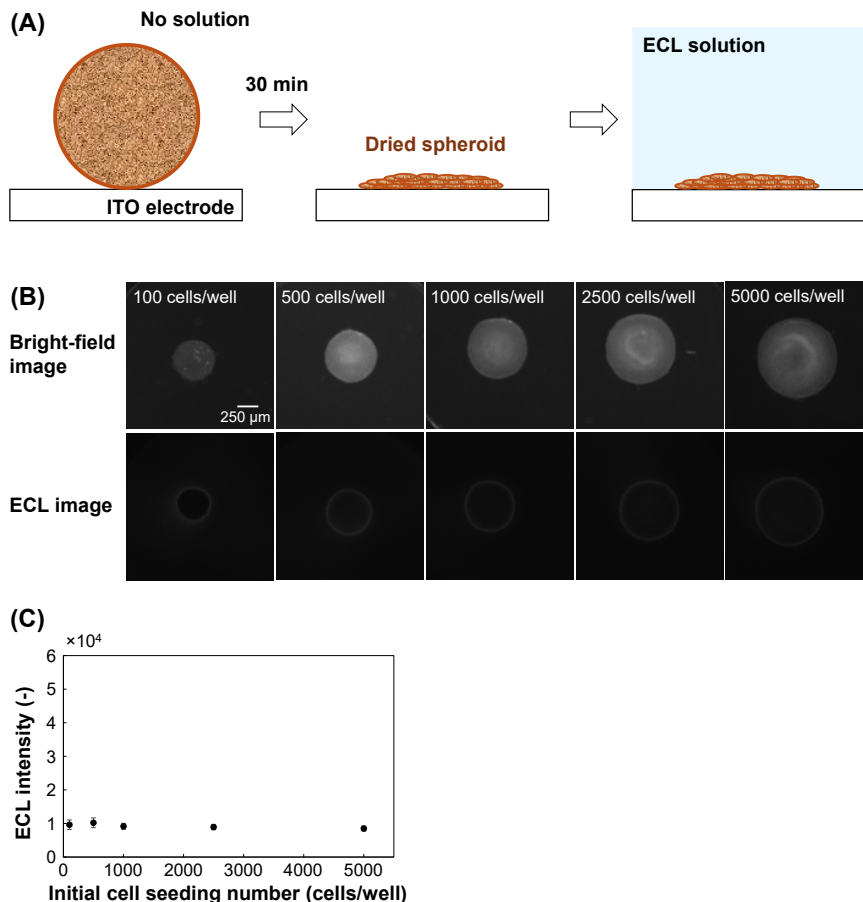


**Fig. 3.29.** ECL imaging of dried spheroids in an attempt to immobilize co-reactants. (A) A schematic illustrating the experimental setup where spheroids were dried directly onto the electrode surface. (B) Representative bright-field and ECL images of the resulting dried spheroids. The spheroids were grown for 7 days from an initial seeding of 100 cells – 5000 cells. The images are representative of three independent experiments ( $n = 3$ ) [109].

### 3.8.1. Investigating NADH as a potential co-reactant

Based on its high intracellular concentration and its established role as a co-reactant for the  $[\text{Ru}(\text{bpy})_3]^{2+}$  ECL system [178], we hypothesized that NADH was the primary biocompound driving the signal. To begin testing this, we verified via cyclic voltammetry that the reaction was electrochemically feasible, confirming that both NADH and the ruthenium complex are oxidized at our operating potential of 1.2 V (Fig. 3.30).

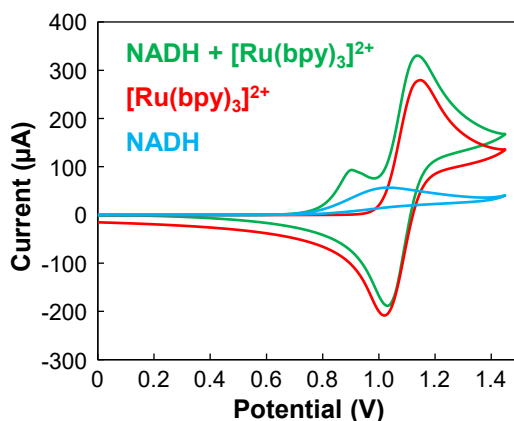


**Fig. 3.30.** Cyclic voltammograms comparing the electrochemical behavior of NADH and  $[\text{Ru}(\text{bpy})_3]^{2+}$ . The figure shows CVs recorded at 100 mV/s for solutions of: (a) 1 mM NADH alone (blue curve), (b) 5 mM  $[\text{Ru}(\text{bpy})_3]^{2+}$  alone (red curve), and (c) a mixture of both (green curve). The slight shift in the NADH oxidation peak when measured alone is likely an artifact caused by minor electrode fouling [109].

Furthermore, the interaction between NADH and the ruthenium complex displayed the classic features of an electrocatalytic (EC) mechanism. In the presence of NADH, we observed a slight increase in the oxidation current of  $[\text{Ru}(\text{bpy})_3]^{2+}$  alongside a corresponding decrease in the reduction current of its oxidized form. This behavior is consistent with the catalytic pathway illustrated in Fig. 3.31A, as compared to the direct oxidation pathway shown in Fig. 3.31B [178]. To test our hypothesis that NADH was the primary co-reactant, we used the ECL assay and an NADH calibration curve to quantify the total signal from the spheroids (Fig. 3.31C). Assuming all of the signal was generated by NADH, this calculation yielded an intracellular concentration in the range of 2 mM – 7 mM. However, this value is more than an order of magnitude higher than the accepted physiological concentration of

NADH ( $168 \mu\text{M} \pm 49 \mu\text{M}$ ) [179]. This significant discrepancy strongly indicates that other abundant biocompounds must be the main co-reactants responsible for the ECL signal.

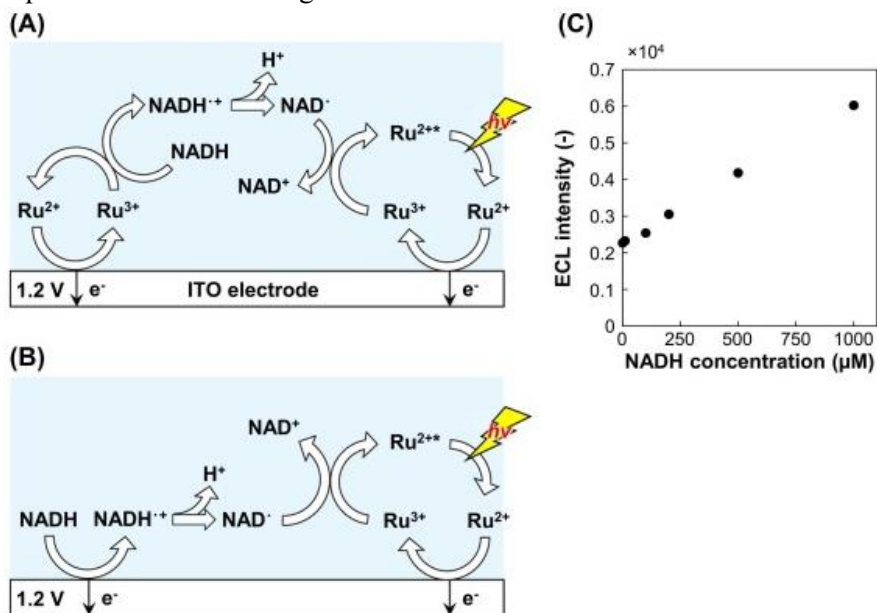


**Fig. 3.31** Analysis of NADH as a co-reactant for the  $[\text{Ru}(\text{bpy})_3]^{2+}$  ECL system. (A, B) Schematic illustrations comparing the two predicted ECL reaction mechanisms: the (A) catalytic and (B) direct oxidation pathways. (C) An experimental calibration plot showing the ECL intensity as a function of NADH concentration. Data are presented as the mean of three experiments ( $n = 3$ ) [109].

### 3.8.2. Investigating GSH as the main candidate co-reactant

Given its high intracellular concentration, we next investigated glutathione (GSH) as another potential co-reactant. While other ECL methods for GSH detection exist, they are typically cathodic or ‘signal-off’ anodic assays [180], [181], [182]. To our knowledge, a ‘signal-on’ anodic ECL assay using  $[\text{Ru}(\text{bpy})_3]^{2+}$  has not yet been reported. Therefore, we explored this novel approach, and the predicted reaction schemes are illustrated in Fig. 3.32A and B.

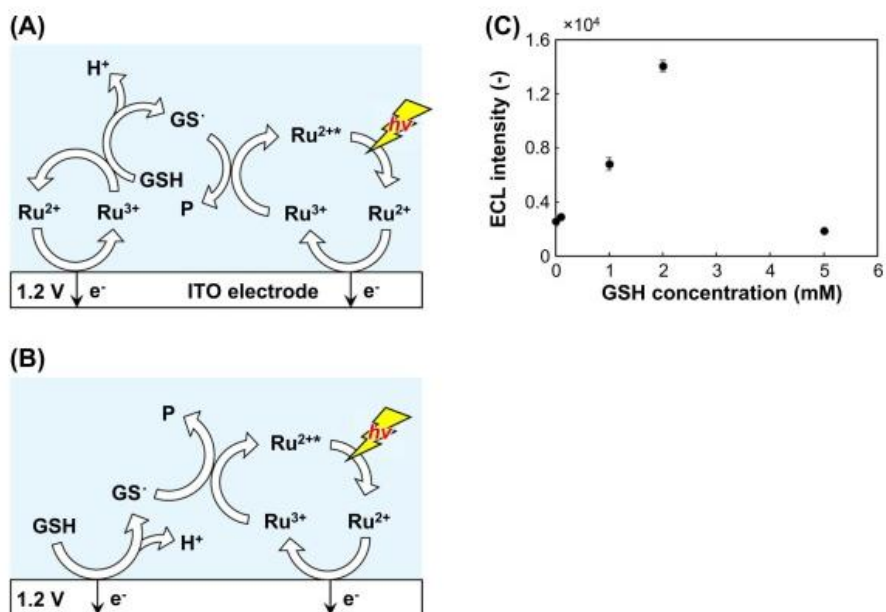


**Fig. 3.32.** Analysis of GSH as a co-reactant for the  $[\text{Ru}(\text{bpy})_3]^{2+}$  ECL system. (A, B) Schematics comparing the two predicted ECL reaction mechanisms: (A) catalytic and (B) direct oxidation pathways. (C) The corresponding experimental calibration plot showing ECL intensity as a function of GSH concentration ( $n = 3$ ) [109].

When we generated the ECL calibration curve (Fig. 3.32C), the signal increased linearly with GSH concentrations up to 2 mM. However, at a higher concentration of 5 mM, the signal dramatically decreased due to a known quenching effect caused by excess GSH [183]. Although the bell shaped calibration curve complicated precise quantification, we could still estimate the concentration of GSH responsible for the signal to be greater than 2 mM. This value falls squarely within the known physiological range of intracellular GSH (1 – 10 mM) [184], providing strong evidence that GSH is a primary co-reactant in our system. A simplified diffusion simulation was then performed for further discussion.

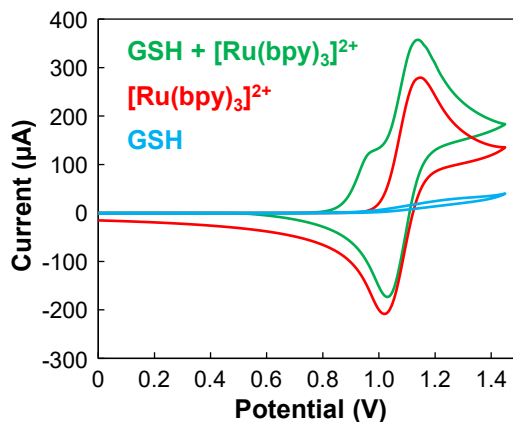


**Fig. 3.33.** CV analysis of the interaction between GSH and  $[\text{Ru}(\text{bpy})_3]^{2+}$ . The figure compares the cyclic voltammograms (scan rate: 100 mV/s) of: 1 mM GSH alone (blue curve), 5 mM  $[\text{Ru}(\text{bpy})_3]^{2+}$  alone (red curve), and a mixture of both (green curve) [109].

For the diffusion simulation, we set the initial intracellular GSH concentration to 10 mM. This value was chosen because it represents the highest end of the physiological range reported in previous studies. We then simulated the diffusion process for 15 sec. to generate the final concentration profile shown in Fig. 3.34. The simulation predicted a concentration gradient of GSH diffusing from the spheroid. The concentration was highest at the point of contact with the electrode (approx. 4 mM) and decreased with distance, reaching about 2 mM at a location 250  $\mu\text{m}$  from the spheroids center. Significantly, this area of high simulated GSH concentration ( $\sim 250 \mu\text{m}$  away) directly corresponds to the region where the maximum ECL intensity was experimentally observed (Fig. 3.22, Fig. 3.25), providing a strong link between our model and our empirical results. The simulation therefore predicts that even under the most generous conditions, the GSH concentration in the primary detection area would not exceed 2 mM. This is a crucial finding, as this concentration range (0 mM – 2 mM) falls perfectly within the linear portion of our experimental GSH calibration curve, confirming that our ECL method is well-suited for quantifying GSH if it is the primary co-reactant. These results also offer an alternative explanation for the low ECL intensity observed at the spheroids center (Fig. 3.22, Fig. 3.25). The high intracellular concentration of GSH in the dense core may be causing a self-quenching effect on the ECL reaction.

We acknowledge, however, that our current data only identifies GSH as a strong candidate for the primary co-reactant, and more direct proof is

needed. Therefore, future work will focus on providing definitive validation. We are planning experiments using GSH synthesis inhibitors and genetic knockdown approaches to conclusively determine the role of GSH in this system.

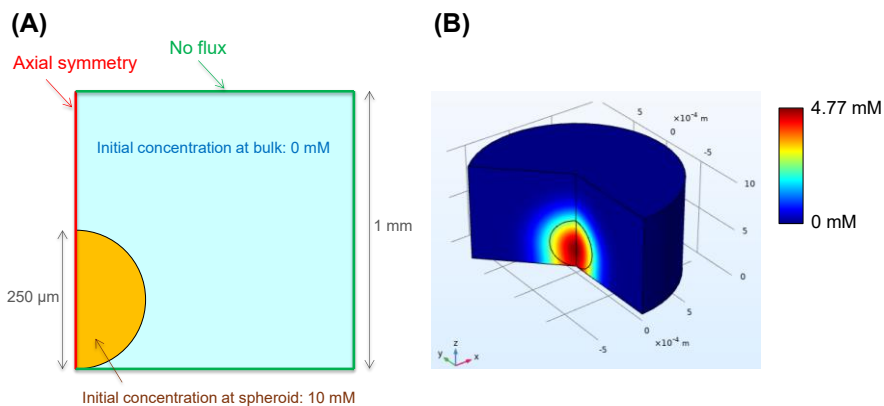
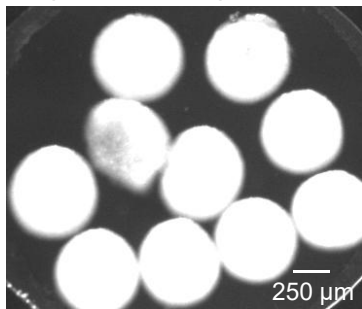


**Fig. 3.34.** Diffusion simulation of cellular compounds in spheroids. (A) A schematic of the 2D axisymmetric model showing the geometry and the initial and boundary conditions used. (B) The resulting concentration profile of the compound after 15 seconds of diffusion. The model assumes a simplified diffusion coefficient of  $1 \times 10^{-9} \text{ m}^2/\text{s}$  in all areas [109].

### 3.9. Platform performance and limitations: throughput and viability analysis

A significant advantage of our ECL microscopy method over conventional techniques, such as scanning electrochemical microscopy (SECM) and electrode arrays, is its potential for high-throughput analysis. Unlike those methods, which often measure one sample at a time, ECL microscopy visualizes electrochemical reactions across a wide field of view. This unique capability allowed us to successfully evaluate multiple spheroids simultaneously using only a single working electrode, as demonstrated in Fig. 3.35.

**Bright-field image**



**ECL image**

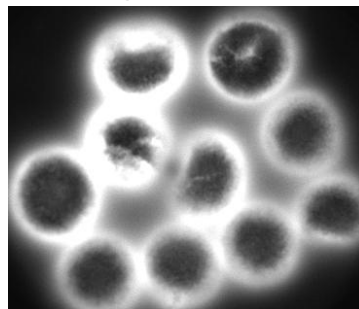


**Fig. 3.35.** Demonstration of high-throughput ECL imaging of multiple living spheroids. The image shows the simultaneous analysis of several 7 days spheroids, each grown from an initial seeding of 5000 cells [109].

A potential limitation of our method is the use of electroporation to release the intracellular co-reactants, as this process could affect cell viability. This might complicate continuous, long-term monitoring of a single spheroid over extended periods. However, our initial viability assessments are encouraging. As shown in Fig 3.36, we found that cells within the spheroids remained viable and retained their ability to proliferate even after undergoing the complete ECL assay procedure.

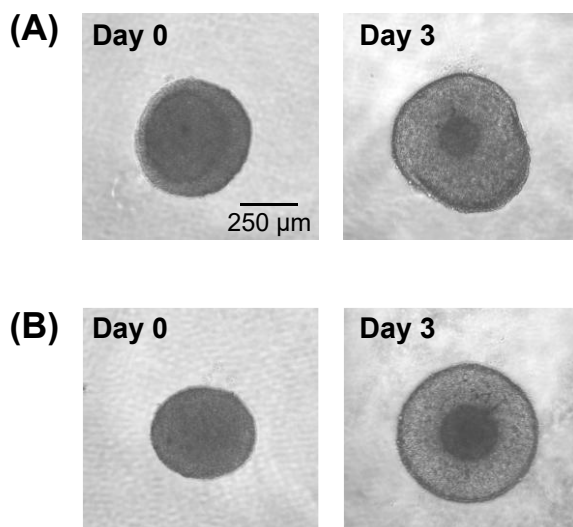


**Fig. 3.36.** Assessment of spheroid viability and proliferation after repeated ECL analysis. The figure compares the continued growth of two spheroids over an additional 3 days period. (A) A spheroid that was previously subjected to 10 cycles of ECL imaging. (B) An untreated control spheroid from the same batch. Both spheroids were initially grown for 3 days from 5000 cells [109].

Propidium Iodide (PI) staining results further support this finding (Fig. 3.24). The lack of PI uptake by cells after the assay indicates that the pores created by the applied potential were transient and that the cell membranes recovered their integrity shortly after the voltage was removed. This confirms that the method does not cause significant, permanent membrane damage. While these results are promising, we recognize two primary limitations of the current method that warrant further investigation. The first is the non-specific detection of co-reactants, as the probe measures a collective pool of molecules rather than a single species. The second is the potential for cell viability to be impacted by the combined effects of electroporation and the  $[\text{Ru}(\text{bpy})_3]^{2+}$  luminophore. Therefore, a more detailed analysis of long-term cell viability is a critical next step for future studies.

Future efforts will focus on improving selectivity through electrode surface modification and enhancing cytocompatibility, potentially by immobilizing the luminophore onto the electrode.

## CONCLUSIONS

This work successfully developed two novel electrochemical platforms for cancer analysis. These platforms enable sensitive biomarker detection and the analysis of 3D spheroids, holding significant potential for both clinical diagnostics and fundamental research.

1. VaninLP, a pioneering ratiometric electrochemical probe, was developed to measure the activity of pantetheinase (Vanin-1). The probe operates via a ratiometric signal-on mechanism, with its electrochemical peak shifting from +0.17 V to a new reporter signal at -0.08 V upon enzymatic reaction. It demonstrated strong enzyme affinity with a Michaelis constant ( $K_m$ ) of 2.38  $\mu\text{M}$ , a performance comparable to or better than existing fluorescent probes

2. The VaninLP probe proved highly effective for direct analysis in complex biofluids. Operating as a DPV-based platform, it achieved a high sensitivity with a limit of detection of 2.47 ng/mL and a wide linear range (8–300 ng/mL,  $R^2=0.993$ ). Crucially, this performance allows for the quantitative, real-time monitoring of Vanin-1 activity in unprocessed human blood and urine, eliminating the need for sample pretreatment and highlighting its value as a potential diagnostic tool.

3. This work introduces a novel ECL microscopy method to visualize diffusive biocompounds from 3D cancer spheroids via electroporation. Calibration experiments with MCF-7 spheroids identified glutathione as the primary endogenous co-reactant for the  $[\text{Ru}(\text{bpy})_3]^{2+}$  signal, showing sensitivity in the low-millimolar range (up to 2 mM). This technique offers a new functional imaging tool for assessing the metabolic state of 3D tumor models.

In summary, this thesis developed two powerful electrochemical strategies for cancer analysis. The VaninLP probe enables direct, sensitive biomarker detection in biofluids, while the ECL microscopy method provides a new functional imaging tool for 3D tumor models. Future work will focus on adapting the VaninLP probe for disposable, low-volume formats and refining the ECL method's selectivity for specific biomarkers in advanced models like spheroids and organoids

## LIST OF REFERENCES

- [1] J. Zugazagoitia, C. Guedes, S. Ponce, I. Ferrer, S. Molina-Pinelo, and L. Paz-Ares, 'Current Challenges in Cancer Treatment', *Clin. Ther.*, vol. 38, no. 7, pp. 1551–1566, July 2016, doi: 10.1016/j.clinthera.2016.03.026.
- [2] M. López-Gómez, E. Malmierca, M. de Górgolas, and E. Casado, 'Cancer in developing countries: The next most preventable pandemic. The global problem of cancer', *Crit. Rev. Oncol. Hematol.*, vol. 88, no. 1, pp. 117–122, Oct. 2013, doi: 10.1016/j.critrevonc.2013.03.011.
- [3] R. Kaur, A. Bhardwaj, and S. Gupta, 'Cancer treatment therapies: traditional to modern approaches to combat cancers', *Mol. Biol. Rep.*, vol. 50, no. 11, pp. 9663–9676, Nov. 2023, doi: 10.1007/s11033-023-08809-3.
- [4] C.-Y. Huang, D.-T. Ju, C.-F. Chang, P. Muralidhar Reddy, and B. K. Velmurugan, 'A review on the effects of current chemotherapy drugs and natural agents in treating non-small cell lung cancer', *BioMedicine*, vol. 7, no. 4, p. 23, 2017, doi: 10.1051/bmdcn/2017070423.
- [5] D. Crosby *et al.*, 'Early detection of cancer', *Science*, vol. 375, no. 6586, p. eaay9040, Mar. 2022, doi: 10.1126/science.aay9040.
- [6] R. C. Fitzgerald, A. C. Antoniou, L. Fruk, and N. Rosenfeld, 'The future of early cancer detection', *Nat. Med.*, vol. 28, no. 4, pp. 666–677, Apr. 2022, doi: 10.1038/s41591-022-01746-x.
- [7] M. Cemazar and G. Sersa, 'Recent Advances in Electrochemotherapy', *Bioelectricity*, vol. 1, no. 4, pp. 204–213, Dec. 2019, doi: 10.1089/bioe.2019.0028.
- [8] Y. Zhang, M. Li, X. Gao, Y. Chen, and T. Liu, 'Nanotechnology in cancer diagnosis: progress, challenges and opportunities', *J. Hematol. Oncol. J Hematol Oncol*, vol. 12, no. 1, p. 137, Dec. 2019, doi: 10.1186/s13045-019-0833-3.
- [9] Y. Cao, J. Xia, L. Li, Y. Zeng, J. Zhao, and G. Li, 'Electrochemical Biosensors for Cancer Diagnosis: Multitarget Analysis to Present Molecular Characteristics of Tumor Heterogeneity', *JACS Au*, vol. 4, no. 12, pp. 4655–4672, Dec. 2024, doi: 10.1021/jacsau.4c00989.
- [10] J. Wang, 'Electrochemical biosensors: Towards point-of-care cancer diagnostics', *Biosens. Bioelectron.*, vol. 21, no. 10, pp. 1887–1892, Apr. 2006, doi: 10.1016/j.bios.2005.10.027.
- [11] A. Zhang *et al.*, 'Sandwich-format ECL immunosensor based on Au star@BSA-Luminol nanocomposites for determination of human chorionic gonadotropin', *Biosens. Bioelectron.*, vol. 101, pp. 219–226, Mar. 2018, doi: 10.1016/j.bios.2017.10.040.
- [12] N. Kumaragurubaran *et al.*, 'Development of an Activity-Based Ratiometric Electrochemical Switch for Direct, Real-Time Sensing of Pantetheinase in Live Cells, Blood, and Urine Samples', *ACS Sens.*,

- vol. 9, no. 10, pp. 5436–5444, Oct. 2024, doi: 10.1021/acssensors.4c01658.
- [13] N. Kumaragurubaran *et al.*, ‘Development of an activity-based ratiometric electrochemical substrate for measuring circulating dipeptidyl peptidase-IV/CD26 in whole blood samples’, *Biosens. Bioelectron.*, vol. 283, p. 117538, Sept. 2025, doi: 10.1016/j.bios.2025.117538.
- [14] K. Ino *et al.*, ‘Recent advances in electrochemiluminescence sensing for in vitro cell analysis: a review’, *Anal. Sci.*, Feb. 2025, doi: 10.1007/s44211-025-00723-x.
- [15] X. Li *et al.*, ‘A novel ECL biosensor for the detection of concanavalin A based on glucose functionalized NiCo<sub>2</sub>S<sub>4</sub> nanoparticles-grown on carboxylic graphene as quenching probe’, *Biosens. Bioelectron.*, vol. 96, pp. 113–120, Oct. 2017, doi: 10.1016/j.bios.2017.04.050.
- [16] K. Hiramoto *et al.*, ‘Recent Advances in Electrochemiluminescence-Based Systems for Mammalian Cell Analysis’, *Micromachines*, vol. 11, no. 5, Art. no. 5, May 2020, doi: 10.3390/mi11050530.
- [17] K. Hiramoto *et al.*, ‘Recent Advances in Electrochemiluminescence-Based Systems for Mammalian Cell Analysis’, *Micromachines*, vol. 11, no. 5, Art. no. 5, May 2020, doi: 10.3390/mi11050530.
- [18] C. Pucci, C. Martinelli, and G. Ciofani, ‘Innovative approaches for cancer treatment: current perspectives and new challenges’, *ecancermedicalscience*, vol. 13, p. 961, Sept. 2019, doi: 10.3332/ecancer.2019.961.
- [19] Y. Ming *et al.*, ‘Progress and Future Trends in PET/CT and PET/MRI Molecular Imaging Approaches for Breast Cancer’, *Front. Oncol.*, vol. 10, Aug. 2020, doi: 10.3389/fonc.2020.01301.
- [20] U. Haberkorn and S. O. Schoenberg, ‘Imaging of lung cancer with CT, MRT and PET’, *Lung Cancer*, vol. 34, pp. 13–23, Dec. 2001, doi: 10.1016/S0169-5002(01)00369-5.
- [21] A. Pulumati, A. Pulumati, B. S. Dwarakanath, A. Verma, and R. V. L. Papineni, ‘Technological advancements in cancer diagnostics: Improvements and limitations’, *Cancer Rep.*, vol. 6, no. 2, p. e1764, 2023, doi: 10.1002/cnr2.1764.
- [22] H. Schoder, M. Gonen, and B. Franklin, ‘Screening for Cancer with PET and PET/CT: Potential and Limitations’, 2007.
- [23] D. Le Bihan, ‘Diffusion MRI: what water tells us about the brain’, *EMBO Mol. Med.*, vol. 6, no. 5, pp. 569–573, May 2014, doi: 10.1002/emmm.201404055.
- [24] F. M. McQueen, ‘Magnetic resonance imaging in early inflammatory arthritis: what is its role?’, *Rheumatology*, vol. 39, no. 7, pp. 700–706, July 2000, doi: 10.1093/rheumatology/39.7.700.
- [25] Vijayalaxmi, M. Fatahi, and O. Speck, ‘Magnetic resonance imaging (MRI): A review of genetic damage investigations’, *Mutat. Res. Mutat.*

- Res.*, vol. 764, pp. 51–63, Apr. 2015, doi: 10.1016/j.mrrev.2015.02.002.
- [26] L. Bartella and W. Huang, ‘Proton (1H) MR Spectroscopy of the Breast’, *RadioGraphics*, vol. 27, no. suppl\_1, pp. S241–S252, Oct. 2007, doi: 10.1148/rg.27si075504.
- [27] F. GharehMohammadi and R. A. Sebro, ‘Efficient Health Care: Decreasing MRI Scan Time’, *Radiol. Artif. Intell.*, vol. 6, no. 3, p. e240174, May 2024, doi: 10.1148/ryai.240174.
- [28] Z. Munn, S. Moola, K. Lisy, D. Riitano, and F. Murphy, ‘Claustrophobia in magnetic resonance imaging: A systematic review and meta-analysis’, *Radiography*, vol. 21, no. 2, pp. e59–e63, May 2015, doi: 10.1016/j.radi.2014.12.004.
- [29] M. Mazonakis and J. Damilakis, ‘Computed tomography: What and how does it measure?’, *Eur. J. Radiol.*, vol. 85, no. 8, pp. 1499–1504, Aug. 2016, doi: 10.1016/j.ejrad.2016.03.002.
- [30] R. C. Nelson, S. Feuerlein, and D. T. Boll, ‘New iterative reconstruction techniques for cardiovascular computed tomography: How do they work, and what are the advantages and disadvantages?’, *J. Cardiovasc. Comput. Tomogr.*, vol. 5, no. 5, pp. 286–292, Sept. 2011, doi: 10.1016/j.jcct.2011.07.001.
- [31] D. W. Townsend, ‘Positron Emission Tomography/Computed Tomography’, *Semin. Nucl. Med.*, vol. 38, no. 3, pp. 152–166, May 2008, doi: 10.1053/j.semnuclmed.2008.01.003.
- [32] V. Tolmachev and S. Stone-Elander, ‘Radiolabelled proteins for positron emission tomography: Pros and cons of labelling methods’, *Biochim. Biophys. Acta BBA - Gen. Subj.*, vol. 1800, no. 5, pp. 487–510, May 2010, doi: 10.1016/j.bbagen.2010.02.002.
- [33] G. Delso, E. ter Voert, F. de G. Barbosa, and P. Veit-Haibach, ‘Pitfalls and Limitations in Simultaneous PET/MRI’, *Semin. Nucl. Med.*, vol. 45, no. 6, pp. 552–559, Nov. 2015, doi: 10.1053/j.semnuclmed.2015.04.002.
- [34] E. C. Ehman *et al.*, ‘PET/MRI: Where might it replace PET/CT?’, *J. Magn. Reson. Imaging*, vol. 46, no. 5, pp. 1247–1262, 2017, doi: 10.1002/jmri.25711.
- [35] R. J. Hicks, R. E. Ware, and J. Callahan, ‘Total-Body PET/CT: Pros and Cons’, *Semin. Nucl. Med.*, vol. 55, no. 1, pp. 11–20, Jan. 2025, doi: 10.1053/j.semnuclmed.2024.07.003.
- [36] C. W. Elston and I. O. Ellis, ‘Pathological prognostic factors in breast cancer. I. The value of histological grade in breast cancer: experience from a large study with long-term follow-up’, *Histopathology*, vol. 19, no. 5, pp. 403–410, Nov. 1991, doi: 10.1111/j.1365-2559.1991.tb00229.x.
- [37] Y. Tohi *et al.*, ‘Impact of health-related quality of life on repeat protocol biopsy compliance on active surveillance for favorable prostate cancer: results from a prospective cohort in the PRIAS-

- JAPAN study’, *Urol. Oncol. Semin. Orig. Investig.*, vol. 40, no. 2, p. 56.e9-56.e15, Feb. 2022, doi: 10.1016/j.urolonc.2021.05.003.
- [38] H. Hillman, ‘Limitations of clinical and biological histology’, *Med. Hypotheses*, vol. 54, no. 4, pp. 553–564, Apr. 2000, doi: 10.1054/mehy.1999.0894.
- [39] J. Camps-Herrero, R. Pijnappel, and C. Balleyguier, ‘MR-contrast enhanced mammography (CEM) for follow-up of breast cancer patients: a “pros and cons” debate’, *Eur. Radiol.*, vol. 34, no. 10, pp. 6264–6270, Oct. 2024, doi: 10.1007/s00330-024-10684-w.
- [40] P. Zubor *et al.*, ‘Current approaches in the clinical management of pregnancy-associated breast cancer—pros and cons’, *EPMA J.*, vol. 9, no. 3, pp. 257–270, Sept. 2018, doi: 10.1007/s13167-018-0139-5.
- [41] K. Kataria, A. Srivastava, and D. Qaiser, ‘What Is a False Negative Sentinel Node Biopsy: Definition, Reasons and Ways to Minimize It?’, *Indian J. Surg.*, vol. 78, no. 5, pp. 396–401, Oct. 2016, doi: 10.1007/s12262-016-1531-9.
- [42] A. Ambrosi, F. Airò, and A. Merkoçi, ‘Enhanced Gold Nanoparticle Based ELISA for a Breast Cancer Biomarker’, *Anal. Chem.*, vol. 82, no. 3, pp. 1151–1156, Feb. 2010, doi: 10.1021/ac902492c.
- [43] V. Liustrovaite *et al.*, ‘Electrochemical sensor for vascular endothelial growth factor based on self-assembling DNA aptamer structure’, *Sci. Total Environ.*, vol. 955, p. 177151, Dec. 2024, doi: 10.1016/j.scitotenv.2024.177151.
- [44] A. Popov, B. Brasiunas, K. Blazevic, A. Kausaite-Minkstimiene, and A. Ramanaviciene, ‘Ultra-sensitive electrochemical immunosensors for clinically important biomarker detection: Prospects, opportunities, and global trends’, *Curr. Opin. Electrochem.*, vol. 46, p. 101524, Aug. 2024, doi: 10.1016/j.coelec.2024.101524.
- [45] M. S. Tabatabaei, R. Islam, and M. Ahmed, ‘Applications of gold nanoparticles in ELISA, PCR, and immuno-PCR assays: A review’, *Anal. Chim. Acta*, vol. 1143, pp. 250–266, Jan. 2021, doi: 10.1016/j.aca.2020.08.030.
- [46] U. Rajčević, R. Juvan, B. Gazvoda, S. Repše, and R. Komel, ‘Assessment of differential expression of oncogenes in gastric adenocarcinoma by fluorescent multiplex RT-PCR assay’, *Pflug. Arch.*, vol. 442, no. 1, pp. r190–r192, Sept. 2001, doi: 10.1007/s004240100020.
- [47] D. M. Ross *et al.*, ‘Patients with chronic myeloid leukemia who maintain a complete molecular response after stopping imatinib treatment have evidence of persistent leukemia by DNA PCR’, *Leukemia*, vol. 24, no. 10, pp. 1719–1724, Oct. 2010, doi: 10.1038/leu.2010.185.
- [48] J. Williams, M. Kostiuk, and V. L. Biron, ‘Molecular Detection Methods in HPV-Related Cancers’, *Front. Oncol.*, vol. 12, Apr. 2022, doi: 10.3389/fonc.2022.864820.

- [49] A. N. Cohen, B. Kessel, and M. G. Milgroom, ‘Diagnosing SARS-CoV-2 infection: the danger of over-reliance on positive test results’, Sept. 28, 2020, *medRxiv*. doi: 10.1101/2020.04.26.20080911.
- [50] S. Goodwin, J. D. McPherson, and W. R. McCombie, ‘Coming of age: ten years of next-generation sequencing technologies’, *Nat. Rev. Genet.*, vol. 17, no. 6, pp. 333–351, June 2016, doi: 10.1038/nrg.2016.49.
- [51] T. Hu, N. Chitnis, D. Monos, and A. Dinh, ‘Next-generation sequencing technologies: An overview’, *Hum. Immunol.*, vol. 82, no. 11, pp. 801–811, Nov. 2021, doi: 10.1016/j.humimm.2021.02.012.
- [52] A. Grada and K. Weinbrecht, ‘Next-Generation Sequencing: Methodology and Application’, *J. Invest. Dermatol.*, vol. 133, no. 8, pp. 1–4, Aug. 2013, doi: 10.1038/jid.2013.248.
- [53] R. Płoski, ‘Next Generation Sequencing—General Information about the Technology, Possibilities, and Limitations’, in *Clinical Applications for Next-Generation Sequencing*, Elsevier, 2016, pp. 1–18. doi: 10.1016/B978-0-12-801739-5.00001-5.
- [54] J. D. Pallua, A. Brunner, B. Zelger, M. Schirmer, and J. Haybaeck, ‘The future of pathology is digital’, *Pathol. - Res. Pract.*, vol. 216, no. 9, p. 153040, Sept. 2020, doi: 10.1016/j.prp.2020.153040.
- [55] M. Titford, ‘A Short History of Histopathology Technique’, *J. Histotechnol.*, vol. 29, no. 2, pp. 99–110, June 2006, doi: 10.1179/his.2006.29.2.99.
- [56] L. Zhu *et al.*, ‘A narrative review of tumor heterogeneity and challenges to tumor drug therapy’, *Ann. Transl. Med.*, vol. 9, no. 16, p. 1351, Aug. 2021, doi: 10.21037/atm-21-1948.
- [57] F. Baldini and M. Minunni, ‘New developments in biosensors’, *Anal. Bioanal. Chem.*, vol. 411, no. 29, pp. 7605–7606, Nov. 2019, doi: 10.1007/s00216-019-02232-z.
- [58] B. Nagel, H. Dellweg, and L. M. Gierasch, ‘Glossary for chemists of terms used in biotechnology (IUPAC Recommendations 1992)’, *Pure Appl. Chem.*, vol. 64, no. 1, pp. 143–168, Jan. 1992, doi: 10.1351/pac199264010143.
- [59] A. Haleem, M. Javaid, R. P. Singh, R. Suman, and S. Rab, ‘Biosensors applications in medical field: A brief review’, *Sens. Int.*, vol. 2, p. 100100, Jan. 2021, doi: 10.1016/j.sintl.2021.100100.
- [60] B. Bohunicky and S. A. Mousa, ‘Biosensors: the new wave in cancer diagnosis’, *Nanotechnol. Sci. Appl.*, vol. 4, pp. 1–10, Dec. 2010, doi: 10.2147/NSA.S13465.
- [61] J. F. Rusling, C. V. Kumar, J. S. Gutkind, and V. Patel, ‘Measurement of biomarker proteins for point-of-care early detection and monitoring of cancer’, *Analyst*, vol. 135, no. 10, pp. 2496–2511, Sept. 2010, doi: 10.1039/C0AN00204F.
- [62] A. Ramanavičius, A. Ramanavičienė, and A. Malinauskas, ‘Electrochemical sensors based on conducting polymer—polypyrrole’,

- Electrochimica Acta*, vol. 51, no. 27, pp. 6025–6037, Aug. 2006, doi: 10.1016/j.electacta.2005.11.052.
- [63] N. J. Ronkainen, H. B. Halsall, and W. R. Heineman, ‘Electrochemical biosensors’, *Chem. Soc. Rev.*, vol. 39, no. 5, pp. 1747–1763, Apr. 2010, doi: 10.1039/B714449K.
- [64] S. M. Borisov and O. S. Wolfbeis, ‘Optical Biosensors’, *Chem. Rev.*, vol. 108, no. 2, pp. 423–461, Feb. 2008, doi: 10.1021/cr068105t.
- [65] P. Skládal, ‘Piezoelectric biosensors’, *TrAC Trends Anal. Chem.*, vol. 79, pp. 127–133, May 2016, doi: 10.1016/j.trac.2015.12.009.
- [66] K. Ramanathan and B. Danielsson, ‘Principles and applications of thermal biosensors’, *Biosens. Bioelectron.*, vol. 16, no. 6, pp. 417–423, Aug. 2001, doi: 10.1016/S0956-5663(01)00124-5.
- [67] A. Singh *et al.*, ‘Recent Advances in Electrochemical Biosensors: Applications, Challenges, and Future Scope’, *Biosensors*, vol. 11, no. 9, Art. no. 9, Sept. 2021, doi: 10.3390/bios11090336.
- [68] V. Perumal and U. Hashim, ‘Advances in biosensors: Principle, architecture and applications’, *J. Appl. Biomed.*, vol. 12, no. 1, pp. 1–15, Jan. 2014, doi: 10.1016/j.jab.2013.02.001.
- [69] D. Grieshaber, R. MacKenzie, J. Vörös, and E. Reimhult, ‘Electrochemical Biosensors - Sensor Principles and Architectures’, *Sensors*, vol. 8, no. 3, Art. no. 3, Mar. 2008, doi: 10.3390/s80314000.
- [70] A. Kumar and K. Mahato, ‘Chapter 6 - Recent advancements in bioreceptors and materials for biosensors’, in *Biosensors in Precision Medicine*, L. C. Brazaca and J. R. Sempionatto, Eds, Elsevier, 2024, pp. 163–202. doi: 10.1016/B978-0-443-15380-8.00007-2.
- [71] E. Brazys, V. Ratautaite, E. Mohsenzadeh, R. Boguzaitė, A. Ramanaviciute, and A. Ramanavicius, ‘Formation of molecularly imprinted polymers: Strategies applied for the removal of protein template (review)’, *Adv. Colloid Interface Sci.*, vol. 337, p. 103386, Mar. 2025, doi: 10.1016/j.cis.2024.103386.
- [72] G. Congur, E. Eksin, and A. Erdem, ‘Levan modified DNA biosensor for voltammetric detection of daunorubicin-DNA interaction’, *Sens. Actuators B Chem.*, vol. 326, p. 128818, Jan. 2021, doi: 10.1016/j.snb.2020.128818.
- [73] I. Morkvenaite-Vilkonciene, A. Ramanaviciene, A. Kisieliute, V. Buciskas, and A. Ramanavicius, ‘Scanning electrochemical microscopy in the development of enzymatic sensors and immunosensors’, *Biosens. Bioelectron.*, vol. 141, p. 111411, Sept. 2019, doi: 10.1016/j.bios.2019.111411.
- [74] E. O. Polat *et al.*, ‘Transducer Technologies for Biosensors and Their Wearable Applications’, *Biosensors*, vol. 12, no. 6, Art. no. 6, June 2022, doi: 10.3390/bios12060385.
- [75] S. Neethirajan, S. K. Tuteja, S.-T. Huang, and D. Kelton, ‘Recent advancement in biosensors technology for animal and livestock health

- management', *Biosens. Bioelectron.*, vol. 98, pp. 398–407, Dec. 2017, doi: 10.1016/j.bios.2017.07.015.
- [76] M. B. Kulkarni, N. H. Ayachit, and T. M. Aminabhavi, 'Biosensors and Microfluidic Biosensors: From Fabrication to Application', *Biosensors*, vol. 12, no. 7, Art. no. 7, July 2022, doi: 10.3390/bios12070543.
- [77] B. Singh, S. Ma, T. O. Hara, and S. Singh, 'Nanomaterials-Based Biosensors for the Detection of Prostate Cancer Biomarkers: Recent Trends and Future Perspective', *Adv. Mater. Technol.*, vol. 8, no. 13, p. 2201860, 2023, doi: 10.1002/admt.202201860.
- [78] J. Zhao, K. Xia, P. He, G. Wei, X. Zhou, and X. Zhang, 'Recent advances of nucleic acid-based cancer biomarkers and biosensors', *Coord. Chem. Rev.*, vol. 497, p. 215456, Dec. 2023, doi: 10.1016/j.ccr.2023.215456.
- [79] N. Cheng *et al.*, 'Recent Advances in Biosensors for Detecting Cancer-Derived Exosomes', *Trends Biotechnol.*, vol. 37, no. 11, pp. 1236–1254, Nov. 2019, doi: 10.1016/j.tibtech.2019.04.008.
- [80] I. Morkvenaite-Vilkonciene *et al.*, 'Scanning electrochemical microscopy: Glucose oxidase as an electrochemical label in sandwich format immunoassay', *Electrochimica Acta*, vol. 463, p. 142790, Sept. 2023, doi: 10.1016/j.electacta.2023.142790.
- [81] N. Razmi and M. Hasanzadeh, 'Current advancement on diagnosis of ovarian cancer using biosensing of CA 125 biomarker: Analytical approaches', *TrAC Trends Anal. Chem.*, vol. 108, pp. 1–12, Nov. 2018, doi: 10.1016/j.trac.2018.08.017.
- [82] R. D'Agata, M. C. Giuffrida, and G. Spoto, 'Peptide Nucleic Acid-Based Biosensors for Cancer Diagnosis', *Molecules*, vol. 22, no. 11, Art. no. 11, Nov. 2017, doi: 10.3390/molecules22111951.
- [83] N. Lyu, A. Hassanzadeh-Barforoushi, L. M. Rey Gomez, W. Zhang, and Y. Wang, 'SERS biosensors for liquid biopsy towards cancer diagnosis by detection of various circulating biomarkers: current progress and perspectives', *Nano Converg.*, vol. 11, no. 1, p. 22, May 2024, doi: 10.1186/s40580-024-00428-3.
- [84] Z. Liu *et al.*, 'Microfluidic biosensors for biomarker detection in body fluids: a key approach for early cancer diagnosis', *Biomark. Res.*, vol. 12, no. 1, p. 153, Dec. 2024, doi: 10.1186/s40364-024-00697-4.
- [85] N. Kumaragurubaran, H.-T. Tsai, P. Arul, S.-T. Huang, and H.-Y. Lin, 'Development of an activity-based ratiometric electrochemical probe of the tumor biomarker  $\gamma$ -glutamyl transpeptidase: Rapid and convenient sensing in whole blood, urine and live-cell samples', *Biosens. Bioelectron.*, vol. 248, p. 115996, Mar. 2024, doi: 10.1016/j.bios.2023.115996.
- [86] K. Manibalan, P. Arul, H.-J. Wu, S.-T. Huang, and V. Mani, 'Self-Immolative Electrochemical Redox Substrates: Emerging Artificial

- Receptors in Sensing and Biosensing’, *ACS Meas. Sci. Au*, vol. 4, no. 2, pp. 163–183, Apr. 2024, doi: 10.1021/acsmesuresciau.3c00057.
- [87] R. Bartucci, A. Salvati, P. Olinga, and Y. L. Boersma, ‘Vanin 1: Its Physiological Function and Role in Diseases’, *Int. J. Mol. Sci.*, vol. 20, no. 16, Art. no. 16, Jan. 2019, doi: 10.3390/ijms20163891.
- [88] J. E. Everhart and E. C. Wright, ‘Association of  $\gamma$ -glutamyl transferase (GGT) activity with treatment and clinical outcomes in chronic hepatitis C (HCV)’, *Hepatology*, vol. 57, no. 5, pp. 1725–1733, 2013, doi: 10.1002/hep.26203.
- [89] P. Busek, J. S. Duke-Cohan, and A. Sedo, ‘Does DPP-IV Inhibition Offer New Avenues for Therapeutic Intervention in Malignant Disease?’, *Cancers*, vol. 14, no. 9, Art. no. 9, Jan. 2022, doi: 10.3390/cancers14092072.
- [90] S. M. Traynor *et al.*, ‘Review—Recent Advances in Electrochemical Detection of Prostate Specific Antigen (PSA) in Clinically-Relevant Samples’, *J. Electrochem. Soc.*, vol. 167, no. 3, p. 037551, Jan. 2020, doi: 10.1149/1945-7111/ab69fd.
- [91] F. Khosravi, M. Rahaie, M. R. Ghaani, M. Azimzadeh, and E. Mostafavi, ‘Ultrasensitive electrochemical miR-155 nanocomposite biosensor based on functionalized/conjugated graphene materials and gold nanostars’, *Sens. Actuators B Chem.*, vol. 375, p. 132877, Jan. 2023, doi: 10.1016/j.snb.2022.132877.
- [92] G. Bezerra *et al.*, ‘Electrochemical aptasensor for the detection of HER2 in human serum to assist in the diagnosis of early stage breast cancer’, *Anal. Bioanal. Chem.*, vol. 411, no. 25, pp. 6667–6676, Oct. 2019, doi: 10.1007/s00216-019-02040-5.
- [93] Z. Liao *et al.*, ‘Microfluidic chip coupled with optical biosensors for simultaneous detection of multiple analytes: A review’, *Biosens. Bioelectron.*, vol. 126, pp. 697–706, Feb. 2019, doi: 10.1016/j.bios.2018.11.032.
- [94] M. Sekhwama, K. Mpofu, S. Sudesh, and P. Mthunzi-Kufa, ‘Integration of microfluidic chips with biosensors’, *Discov. Appl. Sci.*, vol. 6, no. 9, p. 458, Aug. 2024, doi: 10.1007/s42452-024-06103-w.
- [95] A. Pieczara *et al.*, ‘Modified glucose as a sensor to track the metabolism of individual living endothelial cells - Observation of the 1602  $\text{cm}^{-1}$  band called “Raman spectroscopic signature of life”’, *Biosens. Bioelectron.*, vol. 230, p. 115234, June 2023, doi: 10.1016/j.bios.2023.115234.
- [96] Y. Qiao, L. Qiao, Z. Chen, B. Liu, L. Gao, and L. Zhang, ‘Wearable Sensor for Continuous Sweat Biomarker Monitoring’, *Chemosensors*, vol. 10, no. 7, Art. no. 7, July 2022, doi: 10.3390/chemosensors10070273.
- [97] B. Ahmed Taha *et al.*, ‘Advancing cancer diagnostics through multifaceted optical biosensors supported by nanomaterials and

- artificial intelligence: A panoramic outlook', *Microchem. J.*, vol. 205, p. 111307, Oct. 2024, doi: 10.1016/j.microc.2024.111307.
- [98] L. D'Alton *et al.*, 'A holistic pathway to biosensor translation', *Sens. Diagn.*, vol. 3, no. 8, pp. 1234–1246, 2024, doi: 10.1039/D4SD00088A.
- [99] V. Pecoraro, A. Negro, T. Pirotti, and T. Trenti, 'Estimate false-negative RT-PCR rates for SARS-CoV-2. A systematic review and meta-analysis', *Eur. J. Clin. Invest.*, vol. 52, no. 2, p. e13706, 2022, doi: 10.1111/eci.13706.
- [100] S. Linfield, S. Gawinkowski, and W. Nogala, 'Toward the Detection Limit of Electrochemistry: Studying Anodic Processes with a Fluorogenic Reporting Reaction', *Anal. Chem.*, vol. 95, no. 30, pp. 11227–11235, Aug. 2023, doi: 10.1021/acs.analchem.3c00694.
- [101] A. Zinovicus, I. Morkvenaite-Vilkonciene, and A. Ramanavicius, 'Localised Electrochemical Impedance Spectroscopy of Gold Nanoparticles Labelled Antibodies Probed by Platinum Microstructured Ultramicroelectrode', *Materials*, vol. 17, no. 6, Art. no. 6, Jan. 2024, doi: 10.3390/ma17061339.
- [102] J. Wang, 'Electrochemical Glucose Biosensors', *Chem. Rev.*, vol. 108, no. 2, pp. 814–825, Feb. 2008, doi: 10.1021/cr068123a.
- [103] G. Bontempelli and R. Toniolo, 'Electrochemical : Linear Sweep and Cyclic Voltammetry', Amsterdam, 2009. Accessed: June 09, 2025. [Online]. Available: <https://air.uniud.it/handle/11390/877998>
- [104] C. G. Zoski, *Handbook of Electrochemistry*. Elsevier, 2006.
- [105] I. Baranowska, P. Markowski, A. Gerle, and J. Baranowski, 'Determination of selected drugs in human urine by differential pulse voltammetry technique', *Bioelectrochemistry*, vol. 73, no. 1, pp. 5–10, June 2008, doi: 10.1016/j.bioelechem.2008.04.022.
- [106] P. Yáñez-Sedeño, J. M. Pingarrón, J. Riu, and F. X. Rius, 'Electrochemical sensing based on carbon nanotubes', *TrAC Trends Anal. Chem.*, vol. 29, no. 9, pp. 939–953, Oct. 2010, doi: 10.1016/j.trac.2010.06.006.
- [107] E. Brazys, V. Ratautaite, E. Mohsenzadeh, R. Boguzaitė, A. Ramanaviciute, and A. Ramanavicius, 'Formation of molecularly imprinted polymers: Strategies applied for the removal of protein template (review)', *Adv. Colloid Interface Sci.*, vol. 337, p. 103386, Mar. 2025, doi: 10.1016/j.cis.2024.103386.
- [108] S. V. Dzyadevych, V. N. Arkhypova, A. P. Soldatkin, A. V. El'skaya, C. Martelet, and N. Jaffrezic-Renault, 'Amperometric enzyme biosensors: Past, present and future', *IRBM*, vol. 29, no. 2, pp. 171–180, Apr. 2008, doi: 10.1016/j.rbmret.2007.11.007.
- [109] T. Mockaitis *et al.*, 'Electrochemiluminescence microscopy of diffusive biocompounds as co-reactants in cell spheroids with [Ru(bpy)<sub>3</sub>]<sup>2+</sup>', *Sens. Actuators B Chem.*, vol. 441, p. 137944, Oct. 2025, doi: 10.1016/j.snb.2025.137944.

- [110] K. Hiramoto *et al.*, ‘Evaluation of respiratory and secretory activities of multicellular spheroids *via* electrochemiluminescence imaging’, *Electrochimica Acta*, vol. 458, p. 142507, Aug. 2023, doi: 10.1016/j.electacta.2023.142507.
- [111] K. Hiramoto, K. Ino, K. Komatsu, Y. Nashimoto, and H. Shiku, ‘Electrochemiluminescence imaging of respiratory activity of cellular spheroids using sequential potential steps’, *Biosens. Bioelectron.*, vol. 181, p. 113123, June 2021, doi: 10.1016/j.bios.2021.113123.
- [112] K. Hiramoto *et al.*, ‘Recent Advances in Electrochemiluminescence-Based Systems for Mammalian Cell Analysis’, *Micromachines*, vol. 11, no. 5, Art. no. 5, May 2020, doi: 10.3390/mi11050530.
- [113] A. Zanut, A. Fiorani, S. Rebecani, S. Kesarkar, and G. Valenti, ‘Electrochemiluminescence as emerging microscopy techniques’, *Anal. Bioanal. Chem.*, vol. 411, no. 19, pp. 4375–4382, July 2019, doi: 10.1007/s00216-019-01761-x.
- [114] A. Barhoum, Z. Altintas, K. S. S. Devi, and R. J. Forster, ‘Electrochemiluminescence biosensors for detection of cancer biomarkers in biofluids: Principles, opportunities, and challenges’, *Nano Today*, vol. 50, p. 101874, June 2023, doi: 10.1016/j.nantod.2023.101874.
- [115] M. M. Richter, ‘Electrochemiluminescence (ECL)’, *Chem. Rev.*, vol. 104, no. 6, pp. 3003–3036, June 2004, doi: 10.1021/cr020373d.
- [116] E. Villani, K. Sakanoue, Y. Einaga, S. Inagi, and A. Fiorani, ‘Photophysics and electrochemistry of ruthenium complexes for electrogenerated chemiluminescence’, *J. Electroanal. Chem.*, vol. 921, p. 116677, Sept. 2022, doi: 10.1016/j.jelechem.2022.116677.
- [117] C. Fang, H. Li, J. Yan, H. Guo, and T. Yifeng, ‘Progress of the Electrochemiluminescence Biosensing Strategy for Clinical Diagnosis with Luminol as the Sensing Probe’, *ChemElectroChem*, vol. 4, no. 7, pp. 1587–1593, 2017, doi: 10.1002/celec.201700465.
- [118] N. Harvey, ‘Luminescence during Electrolysis’, *J. Phys. Chem.*, vol. 33, no. 10, pp. 1456–1459, Oct. 1929, doi: 10.1021/j150304a002.
- [119] M. Asif *et al.*, ‘A review on electrochemical biosensing platform based on layered double hydroxides for small molecule biomarkers determination’, *Adv. Colloid Interface Sci.*, vol. 262, pp. 21–38, Dec. 2018, doi: 10.1016/j.cis.2018.11.001.
- [120] L.-P. Zong *et al.*, ‘Fe-MOGs-based enzyme mimetic and its mediated electrochemiluminescence for *in situ* detection of H<sub>2</sub>O<sub>2</sub> released from Hela cells’, *Biosens. Bioelectron.*, vol. 184, p. 113216, July 2021, doi: 10.1016/j.bios.2021.113216.
- [121] L. Hu, Y. Wu, M. Xu, W. Gu, and C. Zhu, ‘Recent advances in co-reaction accelerators for sensitive electrochemiluminescence analysis’, *Chem. Commun.*, vol. 56, no. 75, pp. 10989–10999, Sept. 2020, doi: 10.1039/D0CC04371K.

- [122] Y. Zhou *et al.*, ‘A Three-Dimensional Electrochemiluminescence Sensor Integrated with Peptide Hydrogel for Detection of H<sub>2</sub>O<sub>2</sub> Released from Different Subtypes of Breast Cancer Cells’, *Anal. Chem.*, vol. 96, no. 33, pp. 13464–13472, Aug. 2024, doi: 10.1021/acs.analchem.4c01625.
- [123] S. Deng, W. Li, Z. Li, P. Wang, and Q. Ma, ‘Bright luminescent Zn<sub>2</sub>GeO<sub>4</sub>:Mn NP/MXene hydrogel-based ECL biosensor for glioblastoma diagnosis’, *Talanta*, vol. 276, p. 126214, Aug. 2024, doi: 10.1016/j.talanta.2024.126214.
- [124] F. Du, Y. Chen, C. Meng, B. Lou, W. Zhang, and G. Xu, ‘Recent advances in electrochemiluminescence immunoassay based on multiple-signal strategy’, *Curr. Opin. Electrochem.*, vol. 28, p. 100725, Aug. 2021, doi: 10.1016/j.coelec.2021.100725.
- [125] J. H. Sloan, R. W. Siegel, Y. T. Ivanova-Cox, D. E. Watson, M. A. Deeg, and R. J. Konrad, ‘A novel high-sensitivity electrochemiluminescence (ECL) sandwich immunoassay for the specific quantitative measurement of plasma glucagon’, *Clin. Biochem.*, vol. 45, no. 18, pp. 1640–1644, Dec. 2012, doi: 10.1016/j.clinbiochem.2012.07.111.
- [126] J.-T. Cao, Liu, Xiang-Mei, Fu, Yi-Zhuo, Ren, Shu-Wei, and Y.-M. and Liu, ‘Label-Free Ratiometric Electrochemiluminescent (ECL) Immunosensor for the Determination of Prostate Specific Antigen (PSA) in Serum’, *Anal. Lett.*, vol. 55, no. 11, pp. 1810–1821, May 2022, doi: 10.1080/00032719.2022.2027957.
- [127] A. Zhang *et al.*, ‘Electrochemiluminescence immunosensor for sensitive determination of tumor biomarker CEA based on multifunctionalized Flower-like Au@BSA nanoparticles’, *Sens. Actuators B Chem.*, vol. 238, pp. 24–31, Jan. 2017, doi: 10.1016/j.snb.2016.07.009.
- [128] Z. Guo, T. Hao, J. Duan, S. Wang, and D. Wei, ‘Electrochemiluminescence immunosensor based on graphene–CdS quantum dots–agarose composite for the ultrasensitive detection of alpha fetoprotein’, *Talanta*, vol. 89, pp. 27–32, Jan. 2012, doi: 10.1016/j.talanta.2011.11.017.
- [129] X. Meng, X. Pang, J. Yang, X. Zhang, and H. Dong, ‘Recent Advances in Electrochemiluminescence Biosensors for MicroRNA Detection’, *Small*, vol. 20, no. 22, p. 2307701, 2024, doi: 10.1002/smll.202307701.
- [130] F. Yang *et al.*, ‘Electrochemiluminescent CdS Quantum Dots Biosensor for Cancer Mutation Detection at Different Positions on Linear DNA Analytes’, *Anal. Chem.*, vol. 95, no. 37, pp. 14016–14024, Sept. 2023, doi: 10.1021/acs.analchem.3c02649.
- [131] H. Jiang and X. Wang, ‘Alkaline Phosphatase-Responsive Anodic Electrochemiluminescence of CdSe Nanoparticles’, *Anal. Chem.*, vol. 84, no. 16, pp. 6986–6993, Aug. 2012, doi: 10.1021/ac300983t.

- [132] H. Gao *et al.*, ‘Highly selective electrogenerated chemiluminescence biosensor for simultaneous detection of matrix metalloproteinase-2 and matrix metalloproteinase-7 in cell secretions’, *Sens. Actuators B Chem.*, vol. 253, pp. 69–76, Dec. 2017, doi: 10.1016/j.snb.2017.05.142.
- [133] H.-R. Zhang, M.-S. Wu, J.-J. Xu, and H.-Y. Chen, ‘Signal-On Dual-Potential Electrochemiluminescence Based on Luminol–Gold Bifunctional Nanoparticles for Telomerase Detection’, *Anal. Chem.*, vol. 86, no. 8, pp. 3834–3840, Apr. 2014, doi: 10.1021/ac403960g.
- [134] A. Blaich *et al.*, ‘Specificity of two HIV screening tests detecting simultaneously HIV-1 p24 antigen and antibodies to HIV-1 and –2’, *J. Virol. Methods*, vol. 249, pp. 143–146, Nov. 2017, doi: 10.1016/j.jviromet.2017.09.005.
- [135] S. E. K. Kirschbaum and A. J. Baeumner, ‘A review of electrochemiluminescence (ECL) in and for microfluidic analytical devices’, *Anal. Bioanal. Chem.*, vol. 407, no. 14, pp. 3911–3926, May 2015, doi: 10.1007/s00216-015-8557-x.
- [136] A. K. Rajendran, D. Sankar, S. Amirthalingam, H. D. Kim, J. Rangasamy, and N. S. Hwang, ‘Trends in mechanobiology guided tissue engineering and tools to study cell-substrate interactions: a brief review’, *Biomater. Res.*, vol. 27, no. 1, p. 55, June 2023, doi: 10.1186/s40824-023-00393-8.
- [137] E. C. Costa, A. F. Moreira, D. de Melo-Diogo, V. M. Gaspar, M. P. Carvalho, and I. J. Correia, ‘3D tumor spheroids: an overview on the tools and techniques used for their analysis’, *Biotechnol. Adv.*, vol. 34, no. 8, pp. 1427–1441, Dec. 2016, doi: 10.1016/j.biotechadv.2016.11.002.
- [138] S. A. Langhans, ‘Three-Dimensional in Vitro Cell Culture Models in Drug Discovery and Drug Repositioning’, *Front. Pharmacol.*, vol. 9, Jan. 2018, doi: 10.3389/fphar.2018.00006.
- [139] M. Ravi, V. Paramesh, S. r. Kaviya, E. Anuradha, and F. D. P. Solomon, ‘3D Cell Culture Systems: Advantages and Applications’, *J. Cell. Physiol.*, vol. 230, no. 1, pp. 16–26, 2015, doi: 10.1002/jcp.24683.
- [140] W. L. Haisler, D. M. Timm, J. A. Gage, H. Tseng, T. C. Killian, and G. R. Souza, ‘Three-dimensional cell culturing by magnetic levitation’, *Nat. Protoc.*, vol. 8, no. 10, pp. 1940–1949, Oct. 2013, doi: 10.1038/nprot.2013.125.
- [141] Y. Imamura *et al.*, ‘Comparison of 2D- and 3D-culture models as drug-testing platforms in breast cancer’, *Oncol. Rep.*, vol. 33, no. 4, pp. 1837–1843, Apr. 2015, doi: 10.3892/or.2015.3767.
- [142] D. Lv, Z. Hu, L. Lu, H. Lu, and X. Xu, ‘Three-dimensional cell culture: A powerful tool in tumor research and drug discovery (Review)’, *Oncol. Lett.*, vol. 14, no. 6, pp. 6999–7010, Dec. 2017, doi: 10.3892/ol.2017.7134.

- [143] N. M. Cruz *et al.*, ‘Organoid cystogenesis reveals a critical role of microenvironment in human polycystic kidney disease’, *Nat. Mater.*, vol. 16, no. 11, pp. 1112–1119, Nov. 2017, doi: 10.1038/nmat4994.
- [144] A. Rigamonti *et al.*, ‘Large-Scale Production of Mature Neurons from Human Pluripotent Stem Cells in a Three-Dimensional Suspension Culture System’, *Stem Cell Rep.*, vol. 6, no. 6, pp. 993–1008, June 2016, doi: 10.1016/j.stemcr.2016.05.010.
- [145] N. M. Cruz *et al.*, ‘Organoid cystogenesis reveals a critical role of microenvironment in human polycystic kidney disease’, *Nat. Mater.*, vol. 16, no. 11, pp. 1112–1119, Nov. 2017, doi: 10.1038/nmat4994.
- [146] M. C. Cushing and K. S. Anseth, ‘Hydrogel Cell Cultures’, *Science*, vol. 316, no. 5828, pp. 1133–1134, May 2007, doi: 10.1126/science.1140171.
- [147] I. A. Potapova *et al.*, ‘Mesenchymal Stem Cells Support Migration, Extracellular Matrix Invasion, Proliferation, and Survival of Endothelial Cells In Vitro’, *Stem Cells*, vol. 25, no. 7, pp. 1761–1768, July 2007, doi: 10.1634/stemcells.2007-0022.
- [148] Z. Cesarz and K. Tamama, ‘Spheroid Culture of Mesenchymal Stem Cells’, *Stem Cells Int.*, vol. 2016, no. 1, p. 9176357, 2016, doi: 10.1155/2016/9176357.
- [149] R. P. Fordham *et al.*, ‘Transplantation of Expanded Fetal Intestinal Progenitors Contributes to Colon Regeneration after Injury’, *Cell Stem Cell*, vol. 13, no. 6, pp. 734–744, Dec. 2013, doi: 10.1016/j.stem.2013.09.015.
- [150] C.-T. Lee, R. M. Bendriem, W. W. Wu, and R.-F. Shen, ‘3D brain Organoids derived from pluripotent stem cells: promising experimental models for brain development and neurodegenerative disorders’, *J. Biomed. Sci.*, vol. 24, no. 1, p. 59, Aug. 2017, doi: 10.1186/s12929-017-0362-8.
- [151] S. L. Forsberg, M. Ilieva, and T. Maria Michel, ‘Epigenetics and cerebral organoids: promising directions in autism spectrum disorders’, *Transl. Psychiatry*, vol. 8, no. 1, pp. 1–11, Jan. 2018, doi: 10.1038/s41398-017-0062-x.
- [152] C. Jensen and Y. Teng, ‘Is It Time to Start Transitioning From 2D to 3D Cell Culture?’, *Front. Mol. Biosci.*, vol. 7, Mar. 2020, doi: 10.3389/fmolb.2020.00033.
- [153] L. Lei, B. Ma, C. Xu, and H. Liu, ‘Emerging tumor-on-chips with electrochemical biosensors’, *TrAC Trends Anal. Chem.*, vol. 153, p. 116640, Aug. 2022, doi: 10.1016/j.trac.2022.116640.
- [154] M. Oliveira, P. Conceição, K. Kant, A. Ainla, and L. Diéguez, ‘Electrochemical Sensing in 3D Cell Culture Models: New Tools for Developing Better Cancer Diagnostics and Treatments’, *Cancers*, vol. 13, no. 6, Art. no. 6, Jan. 2021, doi: 10.3390/cancers13061381.
- [155] S. Liu *et al.*, ‘Biosensors integrated 3D organoid/organ-on-a-chip system: A real-time biomechanical, biophysical, and biochemical

- monitoring and characterization’, *Biosens. Bioelectron.*, vol. 231, p. 115285, July 2023, doi: 10.1016/j.bios.2023.115285.
- [156] F. Alexander, S. Eggert, and J. Wiest, ‘A novel lab-on-a-chip platform for spheroid metabolism monitoring’, *Cytotechnology*, vol. 70, no. 1, pp. 375–386, Feb. 2018, doi: 10.1007/s10616-017-0152-x.
- [157] Y. Utagawa, K. Ino, Y. Shinoda, M. Yamazaki, H. Abe, and H. Shiku, ‘Enzyme-Free In-Situ Electrochemical Measurement Using a Porous Membrane Electrode for Glucose Transport into Cell Spheroids’, *ACS Sens.*, vol. 9, no. 8, pp. 4248–4255, Aug. 2024, doi: 10.1021/acssensors.4c01230.
- [158] A. Weltin, S. Hammer, F. Noor, Y. Kaminski, J. Kieninger, and G. A. Urban, ‘Accessing 3D microtissue metabolism: Lactate and oxygen monitoring in hepatocyte spheroids’, *Biosens. Bioelectron.*, vol. 87, pp. 941–948, Jan. 2017, doi: 10.1016/j.bios.2016.07.094.
- [159] Y. Yang, Y. Hu, W. Shi, and H. Ma, ‘A near-infrared fluorescence probe for imaging of pantetheinase in cells and mice in vivo’, *Chem. Sci.*, vol. 11, no. 47, pp. 12802–12806, 2020, doi: 10.1039/D0SC04537C.
- [160] A. Sagi, J. Rishpon, and D. Shabat, ‘Amperometric Assay for Aldolase Activity: Antibody-Catalyzed Ferrocenylamine Formation’, *Anal. Chem.*, vol. 78, no. 5, pp. 1459–1461, Mar. 2006, doi: 10.1021/ac0517141.
- [161] T. S. T. Balamurugan, C.-H. Huang, P.-C. Chang, and S.-T. Huang, ‘Electrochemical Molecular Switch for the Selective Profiling of Cysteine in Live Cells and Whole Blood and for the Quantification of Aminoacylase-1’, *Anal. Chem.*, vol. 90, no. 21, pp. 12631–12638, Nov. 2018, doi: 10.1021/acs.analchem.8b02799.
- [162] S. Campuzano, M. Pedrero, P. Yáñez-Sedeño, and J. M. Pingarrón, ‘New challenges in point of care electrochemical detection of clinical biomarkers’, *Sens. Actuators B Chem.*, vol. 345, p. 130349, Oct. 2021, doi: 10.1016/j.snb.2021.130349.
- [163] N. Kumaragurubaran, P. Arul, S.-T. Huang, C.-H. Huang, S.-B. Fang, and Y.-H. Lin, ‘Nanocatalyst coupled with a latent-ratiometric electrochemical switch for label-free zero-tolerance rapid detection of live *Salmonella* in whole blood samples’, *Sens. Actuators B Chem.*, vol. 381, p. 133428, Apr. 2023, doi: 10.1016/j.snb.2023.133428.
- [164] S. Kumaravel, G.-R. Luo, S.-T. Huang, H.-Y. Lin, C.-M. Lin, and Y.-C. Lee, ‘Development of a novel latent electrochemical molecular substrate for the real-time monitoring of the tumor marker aminopeptidase N in live cells, whole blood and urine’, *Biosens. Bioelectron.*, vol. 203, p. 114049, May 2022, doi: 10.1016/j.bios.2022.114049.
- [165] K. Hosohata, H. Ando, Y. Fujiwara, and A. Fujimura, ‘Vanin-1; a potential biomarker for nephrotoxicant-induced renal injury’,

- Toxicology*, vol. 290, no. 1, pp. 82–88, Nov. 2011, doi: 10.1016/j.tox.2011.08.019.
- [166] S. Duprè, R. Chiaraluce, M. Nardini, C. Cannella, G. Ricci, and D. Cavallini, ‘Continuous spectrophotometric assay of pantetheinase activity’, *Anal. Biochem.*, vol. 142, no. 1, pp. 175–181, Oct. 1984, doi: 10.1016/0003-2697(84)90534-7.
- [167] Y. Hu, H. Li, W. Shi, and H. Ma, ‘Ratiometric Fluorescent Probe for Imaging of Pantetheinase in Living Cells’, *Anal. Chem.*, vol. 89, no. 20, pp. 11107–11112, Oct. 2017, doi: 10.1021/acs.analchem.7b03303.
- [168] J. Qian *et al.*, ‘Visible to Near-Infrared Emission Ratiometric Fluorescent Probe for the Detection of Vanin-1 In Vivo’, *ACS Sens.*, vol. 5, no. 9, pp. 2806–2813, Sept. 2020, doi: 10.1021/acssensors.0c00880.
- [169] J. Qian *et al.*, ‘Red emission ratio fluorescent probe for the activity of vanin-1 and imaging in vivo’, *J. Hazard. Mater.*, vol. 401, p. 123863, Jan. 2021, doi: 10.1016/j.jhazmat.2020.123863.
- [170] P. Lu *et al.*, ‘Near-Infrared Fluorescent Probe for Imaging and Evaluating the Role of Vanin-1 in Chemotherapy’, *Anal. Chem.*, vol. 93, no. 29, pp. 10378–10387, July 2021, doi: 10.1021/acs.analchem.1c02386.
- [171] F. Mariani and L. Roncucci, ‘Role of the Vanins–Myeloperoxidase Axis in Colorectal Carcinogenesis’, *Int. J. Mol. Sci.*, vol. 18, no. 5, Art. no. 5, May 2017, doi: 10.3390/ijms18050918.
- [172] Y. Hu, H. Li, W. Shi, and H. Ma, ‘Ratiometric Fluorescent Probe for Imaging of Pantetheinase in Living Cells’, *Anal. Chem.*, vol. 89, no. 20, pp. 11107–11112, Oct. 2017, doi: 10.1021/acs.analchem.7b03303.
- [173] P. A. M. Jansen *et al.*, ‘Discovery of Small Molecule Vanin Inhibitors: New Tools To Study Metabolism and Disease’, *ACS Chem. Biol.*, vol. 8, no. 3, pp. 530–534, Mar. 2013, doi: 10.1021/cb3006424.
- [174] H. Yu *et al.*, ‘Vanin1 (VNN1) in chronic diseases: Future directions for targeted therapy’, *Eur. J. Pharmacol.*, vol. 962, p. 176220, Jan. 2024, doi: 10.1016/j.ejphar.2023.176220.
- [175] C. T. Wittwer *et al.*, ‘Enzymes for liberation of pantothenic acid in blood: use of plasma pantetheinase’, *Am. J. Clin. Nutr.*, vol. 50, no. 5, pp. 1072–1078, Nov. 1989, doi: 10.1093/ajcn/50.5.1072.
- [176] K. Hosohata, H. Matsuoka, and E. Kumagai, ‘Association of urinary vanin-1 with kidney function decline in hypertensive patients’, *J. Clin. Hypertens.*, vol. 23, no. 7, pp. 1316–1321, 2021, doi: 10.1111/jch.14295.
- [177] M. O. Oduoye *et al.*, ‘Unlocking the potential of novel RTS, S/AS01, and R21/Matrix-M™ malaria vaccines in African nations’, *Health Sci. Rep.*, vol. 7, no. 1, p. e1797, 2024, doi: 10.1002/hsr2.1797.
- [178] F. Ben Trad *et al.*, ‘Electrochemiluminescent imaging of a NADH-based enzymatic reaction confined within giant liposomes’, *Anal.*

- Bioanal. Chem.*, vol. 416, no. 30, pp. 7385–7394, Dec. 2024, doi: 10.1007/s00216-024-05133-y.
- [179] Q. Yu and A. A. Heikal, ‘Two-photon autofluorescence dynamics imaging reveals sensitivity of intracellular NADH concentration and conformation to cell physiology at the single-cell level’, *J. Photochem. Photobiol. B*, vol. 95, no. 1, pp. 46–57, Apr. 2009, doi: 10.1016/j.jphotobiol.2008.12.010.
- [180] J. Li, X. Shan, D. Jiang, Y. Wang, W. Wang, and Z. Chen, ‘A novel electrochemiluminescence sensor based on resonance energy transfer from MoS<sub>2</sub>QDs@g-C<sub>3</sub>N<sub>4</sub> to NH<sub>2</sub>-SiO<sub>2</sub>@PTCA for glutathione assay’, *Analyst*, vol. 145, no. 23, pp. 7616–7622, Nov. 2020, doi: 10.1039/D0AN01542C.
- [181] Y. Pu, M. Zhou, P. Wang, Q. Wu, T. Liu, and M. Zhang, ‘An ultrasensitive electrochemiluminescence sensor based on luminol functionalized AuNPs@Fe-Co-Co nanocomposite as signal probe for glutathione determination’, *J. Electroanal. Chem.*, vol. 873, p. 114374, Sept. 2020, doi: 10.1016/j.jelechem.2020.114374.
- [182] C. V. Raju and S. S. Kumar, ‘Highly sensitive novel cathodic electrochemiluminescence of tris(2,2'-bipyridine)ruthenium(II) using glutathione as a co-reactant’, *Chem. Commun.*, vol. 53, no. 49, pp. 6593–6596, June 2017, doi: 10.1039/C7CC03349D.
- [183] Y. Xu *et al.*, ‘Sensitive and selective determination of GSH based on the ECL quenching of Ru(II) 1,10-phenanthroline-5,6-dione complex’, *Biosens. Bioelectron.*, vol. 77, pp. 182–187, Mar. 2016, doi: 10.1016/j.bios.2015.09.033.
- [184] K. Umezawa, M. Yoshida, M. Kamiya, T. Yamasoba, and Y. Urano, ‘Rational design of reversible fluorescent probes for live-cell imaging and quantification of fast glutathione dynamics’, *Nat. Chem.*, vol. 9, no. 3, pp. 279–286, Mar. 2017, doi: 10.1038/nchem.2648.



# SANTRAUKA

## Ivadas

Vėžys yra viena didžiausių pasaulinių sveikatos problemų, kuri kasmet nusineša milijonus žmonių gyvybių. Pasaulio sveikatos organizacijos duomenimis, naujų vėžio atvejų skaičius pasaulyje kasmet auga ir nuo 20 mln. užregistruotų 2022 m. atvejų turėtų pasiekti 35 mln. 2025 m. [1]. Šis augimas siejamas su sparčiai didėjančia ir senėjančia žmonių populiacija, žalingais gyvenimo būdo įpročiais, tokiais kaip tabako ir alkoholio vartojimu, nutukimu bei aplinkos tarša. Viena dažniausiai pasitaikančių vėžio formų yra plaučių vėžys, kuris yra siejamas ir su pagrindine mirčių priežastimi [2]. Nepaisant mokslinės pažangos ankstyva vėžio diagnostika išlieka dideliu iššūkiu, nes dauguma vėžio formų nesukelia simptomų pradinėse stadijose ir išlieka nepastebėtos. Dėl šių priežasčių liga yra nustatoma vėlai, gydymas tampa sudėtingesnis ir reikalaujantis agresyvių gydymo metodų, kaip chemoterapija ar chirurgija, kurie yra susiję su mažesniu išgyvenamumo procentu [3].

Ankstyva vėžio diagnostika yra kritinis veiksnys nulemiantis gydymo strategiją ir paciento išgyvenamumą, nes tai leidžia taikyti veiksmingesnius ir mažiau invazinius metodus [4, 5], tačiau vis dar trūksta jautrių metodų, kurie leistų patikimai nustatyti vėžio plitimą ankstyvose stadijose. Dabartiniai tyrimų metodai yra lėti, nepatogūs pacientui, pavojingi pakartotiniam naudojimui ir per brangūs mažesnėms gydymo įstaigoms [6]. Reaguodama į iškilusius trūkumus mokslo bendruomenė aktyviai ieško naujų sprendimų, kaip išspręsti šias problemas. Daug žadantys yra nanotechnologijų, dirbtinio intelekto ir elektrocheminių metodų pagrindu sukurti įrankiai [7, 8]. Dabartiniame kontekste ypač išsiskiria elektrocheminiai biologiniai jutikliai. Jie užtikrina didelį specifiškumą, jautrumą, itin žemą aptikimo ribą bei greitą tyrimą [9, 10]. Biologiniai jutikliai geba aptikti su vėžiu susijusius biožymenis (baltymus, DNR mutacijas, cirkuliuojančias naviko ląsteles) kūno skysčiuose. Jų integravimas į gydymo procesą sudaro sąlygas neinvaziniam ir dažnesniam paciento būklės stebėjimui bei personalizuotam gydymui. Tarp inovatyvių metodų ypač reikšminga tapma elektrocheminės liuminescencijos (ECL) mikroskopija. ECL pagrįsti imunologiniai tyrimai pasiekia femtomolines aptikimo ribas ir yra pranašesni už tradicinius ELISA metodus tiek jautrumo, tiek greičio požiūriu, todėl itin tinka ankstyvosios stadijos vėžio diagnostikai [11]. Dar didesnę potencialą ateityje suteikia biologinių jutiklių ir 3D ląstelių sferoidų tyrimai. Šie metodai gali tiksliau atkurti naviko struktūrą ir mikroaplinką, maistinių medžiagų ir deguonies gradientus, ląstelių sąveiką ir vaistų prasiskverbimo barjerus nei įprastinės 2D ląstelių kultūros [16], todėl

leidžia patikimiau tirti vaistų veiksmingumą ir naviko elgesį [14]. Biologinių jutiklių ir ECL integravimas leidžia realiuoju laiku stebėti sferoidų metabolizmą, biožymenų sekreciją ir reakcijas į terapinius agentus [17], tai suteiktų unikalią galimybę greitai ir tiksliai įvertinti gydymo efektyvumą bei atsparumo vystymąsi.

Šiame darbe sąmoningai pasirinktos kliniškai aktualios sistemos. Sukurta elektrocheminė platforma orientuota į fermentą Vanin-1 ir panteteinazę, vėžio biožymenį, kurio perteklius nustatomas kelių tipų vėžiuose. 3D sferoidų tyrimams naudota plačiai taikoma MCF-7 krūties vėžio ląstelių linija. Visus šiuos tyrimus jungia elektrochemija, kuri pasirinkta dėl didelio jautrumo, mažos kainos ir miniatiūrizacijos galimybių. Tikimasi, kad tolesnis šios technologijos tobulinimas leis kurti prietaisus, kurie pagreitins vėžio diagnostiką, supaprastins analizę ir per kelias minutes pateiks rezultatus gydytojo kabinete, žymiai pagerinant vėžio progresavimo ir gydymo stebėjimą.

### **Tyrimo tikslas:**

Ištirti Vani-1 biožymenį ir MCF-7 vėžio ląstelių linijos sferoidus naudojant susintetintą VaninLP zondą ir elektrocheminės liuminescencijos mikroskopiją.

### **Tyrimo uždaviniai:**

1. Susintetinti VaninLP zondą fermentui Vanin-1 ir ištirti jo elektrocheminės savybes.
2. Atlikti elektrocheminius tyrimus su susintetintu zonu, siekiant nustatyti Vanin-1 fermentą kraujo ir šlapimo mėginiuose.
3. Ištirti MCF-7 sferoidų išskiriamus koregentus naudojant elektrocheminės liuminescencijos mikroskopiją.

## **Disertacijos mokslinis naujumas**

Šios disertacijos darbo naujumą sudaro dviejų elektrocheminių platformų, skirtų spręsti pagrindinius vėžio diagnostikos iššūkius, sukūrimas. Pirmasis pagrindinis indėlis, tai VaninLP zondo sukūrimas ir sintezė. VaninLP yra pirmasis aktyvumu pagrįstas elektrocheminis ratiometrinis zondas skirtas fermentui Vanin-1 aptikti. Šiame darbe pademonstruotas sėkmingas jo taikymas tiesioginiam fermento aktyvumo kiekybiniam įvertinimui realiuoju laiku sudėtinguose, neapdorotuose biologiniuose mėginiuose, įskaitant kraują ir gyvų vėžio ląstelių paviršių. Antrasis indėlis, tai elektrocheminės liuminescencijos mikroskopijos panaudojimas vizualizuoti endogeninius, difunduojančius biocheminius junginius, tokius, kaip glutationas, kai jie išsiskiria iš gyvų 3D vėžio ląstelių sferoidų. Tai leido sukurti naują, neinvazinį metodą, skirtą funkciniam naviko modelio metabolinės būklės vaizdavimui. Abi šios platformos žymi reikšmingą pažangą, suteikdamos naujus įrankius tiek tiesioginiam biožymenų kiekybiniam nustatymui, tiek funkcinei fiziologiškai reikšmingų vėžio modelių analizei

### **Ginamieji teiginiai:**

1. Naujasis elektrocheminis zondas VaninLP leidžia jautriai, selektyviai ir realiuoju laiku kiekybiškai įvertinti panteteinazės (Vanin-1) aktyvumą sudėtingose biologinėse terpėse, įveikiant pagrindinius tradicinių tyrimo metodų trūkumus.
2. Elektrocheminės liuminescencijos mikroskopija gali būti sėkmingai pritaikyta neinvaziniam endogeninių, difunduojančių koregentų (daugiausia glutationo) išsiskyrimo iš gyvų 3D vėžio sferoidų stebėjimui, suteikiant informatyvų jų metabolinės būklės vaizdą.
3. Sukurtos elektrocheminės platformos, skirtos panteteinazės kiekybiniam nustatymui kraujo ir šlapimo mėginiuose bei MCF-7 sferoidų metabolizmo tyrimams pasitelkiant elektrocheminę liuminescenciją, kurios leidžia realiuoju laiku stebėti fermentinius biožymenis ir naviko pokyčius.

## **Autoriaus indėlis**

Šios disertacijos autorius buvo pagrindinis tyrėjas, atsakingas už eksperimentinį darbą, duomenų analizę ir dviejų pagrindinių čia pristatomų projektų rankraščių parengimą. Pirmojo projekto metu autorius atliko visą daugiapakopę VaninLP zondo cheminę sintezę, paruošė mėginius charakterizavimui BMR, MS ir FT-IR metodais bei atliko visus elektrocheminius eksperimentus. Antrojo projekto metu autorius buvo atsakingas už 3D vėžio sferoidų auginimą, elektrodų gamybą ir visų elektrocheminės liuminescencijos mikroskopijos matavimų atlikimą. Abiejuose tyrimuose autorius analizavo duomenis, parengė grafikus ir iliustracijas bei prisidėjo prie mokslinių straipsnių rengimo.

# 1. LITERATŪROS APŽVALGA

## 1.1. Tradiciniai vėžio nustatymo metodai

Nors tradiciniai vėžio diagnostikos metodai tebėra nepakeičiama klinikinės onkologijos dalis, jie turi esminių trūkumų, kurie apsunkina ankstyvą ir tikslią pacientų diagnostiką. Vaizdinimo metodai, tokie kaip magnetinio rezonanso tyrimas (MRT), kompiuterinė tomografija (KT) ar pozitronų emisijos tomografija (PET) yra labai naudingos nustatant jau susiformavusius navikus, tačiau jų galimybes riboja didelės išlaidos, jonizuojančiosios spinduliuotės poveikis ir nepakankama skiriamoji geba, trukdanti aptikti mažus, ankstyvos stadijos vėžio darinius [33–35]. Biopsija ir histopatologinis tyrimas, tai invazinės procedūros, galinčios kelti riziką pacientui ir dėl naviko heterogeniškumo bei mėginių paėmimo klaidų diagnozė gali būti netiksli ir klaidinga [38, 41]. Molekulinės diagnostikos metodai, tokie kaip fermentais susietas imunosorbento tyrimas (ELISA), polimerazinė grandininė reakcija (PGR) ar naujos kartos sekoskaita (NGS), nors ir yra labai jautrūs, taip pat turi savų trūkumų. Jie gali rodyti klaidingus rezultatus, būti jautrūs užteršimui, brangūs ir per sudėtingi, kad būtų plačiai taikomi įprastinėje klinikinėje praktikoje [44, 45, 49, 52, 53].

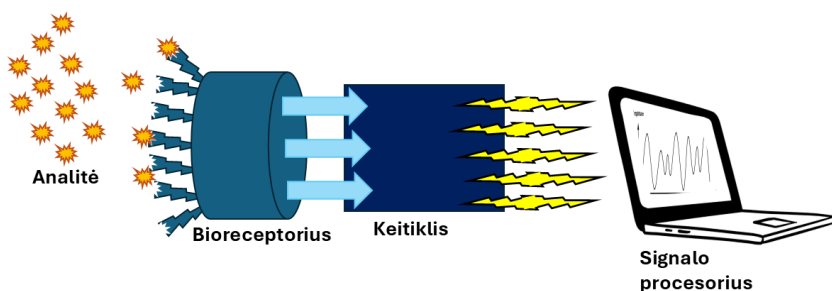
Taigi susiduriame su problema, kad dalis navikų nustatoma per vėlai, tyrimai išlieka brangūs, invaziniai, o ligos eigos realiuoju laiku stebėti dažnai nėra galimybių [35, 39, 51]. Todėl skubiai reikalingos alternatyvios diagnostikos platformos, kurios būtų greitesnės, tikslesnės, neinvazinės ir lengvai pritaikomos klinikoje. Vienas tokių sprendimų yra šiame darbe sukurti elektrocheminiai biologiniai jutikliai, leidžiantys atlikti greitą, patikimą ir pacientui saugų tyrimą [9].

## 1.2 Biologiniai jutikliai onkologijoje

Biologiniai jutikliai arba biojutikliai yra pažangūs analitiniai prietaisai, kurių svarba onkologiniuose tyrimuose nuolat auga. Biojutikliai siūlo jautrią, specifinę ir greitą alternatyvą tradiciniams diagnostikos metodams [59, 60]. Jų veikimo principas pagrįstas trimis pagrindiniais komponentais (1.2.1 pav.): bioreceptoriaus (pvz. Antikūnas ar fermentas), kuris specifiskai atpažįsta ieškomą vėžio biožymenį [70, 71]; keitiklio, kuris šį atpažinimo įvykį paverčia matomu signalu, dažniausiai elektriniu [74]; ir signalo procesoriaus, kuris gautą signalą apdoroja ir pateikia aiškų, interpretuojamą signalą [68].

Dėl tokios sandaros biojutikliai yra universalūs ir gali aptikti platų spektrą vėžio biožymenų, įskaitant baltymus (pvz., PSA) [77], nukleino rūgštis (pvz., ctDNA) [78] ir fermentus (pvz., Vanin-1) [12], tiesiogiai sudėtinguose biologiniuose mėginiuose, tokiuose kaip kraujas. Jų klinikinė reikšmė jau įrodyta, nes jie sėkmingai taikomi stebint terapinių taikinių, tokių kaip HER2, aktyvumą [92] ar yra integruojami į skystosios biopsijos platformas [84].

Apibendrinant, biologiniai jutikliai, ypač elektrocheminiai, išsprendžia daugumą tradicinių metodų trūkumų. Jie greitesni, pigesni, nereikalauja sudėtingos infrastruktūros ir yra skirti diagnostikai prie paciento lovos [97]. Tai paverčia juos galingais ir perspektyviais įrankiais, padedančiais užpildyti kritines spragas individualizuotoje vėžio diagnostikoje bei ilgalaikėje pacientų stebėsenoje.

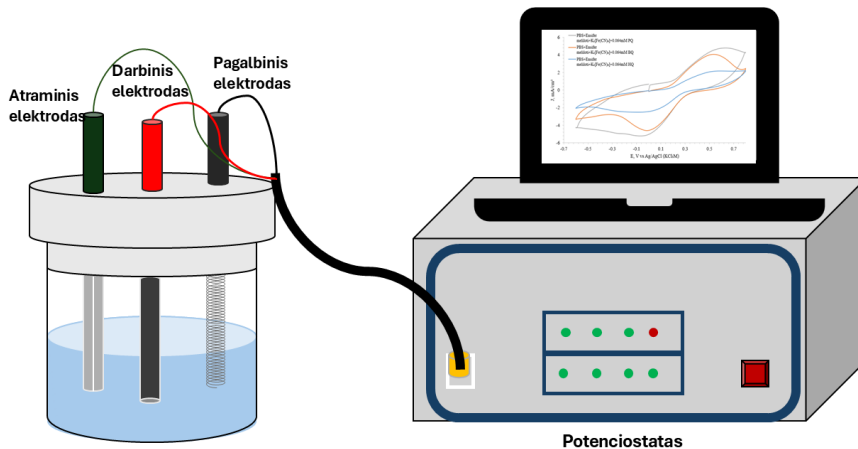


1.2.1 pav. Biosensoriaus veikimo principo schema

### 1.3 Elektrocheminio aptikimo principai

Elektrocheminio aptikimo principas grindžiamas specifinių biocheminių sąveikų konversija į kiekybiškai įvertinamą elektrinį signalą, kuris dažniausiai gaunamas vykstant redokso reakcijoms elektrodų paviršiuje [62, 100]. Šiems matavimams paprastai naudojama trijų elektrodų sistema (1.3.1 pav), leidžianti tiksliai kontroliuoti potencialą ir matuoti srovę [102]. Elektrocheminės technologijos suteikia biojutikliams reikšmingų privalumų, tokių kaip didelis jautrumas, greita atsako kinetika bei galimybė miniatiūrizuoti sistemas, todėl jos tampa tinkamos naudoti prie paciento [97]. Esminis šių biojutiklių pranašumas, lyginant su optinėmis sistemomis, yra

gebėjimas veikti drumzlinuose ar nepermatomuose biologiniuose mėginiuose, pavyzdžiui, kraujyje, todėl jie ypač tinka klinikinei diagnostikai [12]. Be to, šių platformų universalumą atskleidžia platus pritaikomų metodų spektras: nuo jautrios kiekybinės analizės, atliekamos diferencine impulsine voltamperometrija (DPV) [105], iki pažangaus vaizdinimo, pasitelkiant elektrocheminę liuminescenciją (ECL) [14], kurie sukuria galingą ir lankstų įrankį šiuolaikinėje diagnostikoje [109, 110].



1.3.1 pav. Trijų elektrodų sistemos schema

#### 1.4 Elektrocheminė liuminescencija vėžio nustatymui

Elektrocheminės liuminescencijos (ECL) mikroskopija yra procesas, kurio metu ant elektrodo paviršiaus vykstant elektrochemiškai sukeltoms redokso reakcijoms išspinduliuojama šviesa [17]. Šiai reakcijai paprastai reikalingas liuminoformas (pvz.  $[\text{Ru}(\text{bpy})_3]^{2+}$ ) ir tinkamas koregentas [14, 110]. Pagrindinis šio metodo pranašumas – išskirtinis jautrumas. Kadangi šviesa sukuriama pačios reakcijos metu ir nenaudojami išoriniai sužadinimo šaltiniai, beveik visiškai pašalinamas foninis triukšmas. Tai užtikrina labai aukštą signalo ir triukšmo santykį [111, 113]. Onkologijoje ši technologija tapo itin veiksmingu metodu vėžio biožymenų (baltymų, nukleorūgščių ir fermentų) aptikimui. Jos jautrumas dažnai viršija tradicinių imunologinių tyrimų galimybes [122, 124, 125]. ECL technologijos klinikinis potencialas patvirtintas sėkmingu jos integravimu į komercines diagnostines platformas

[134]. Be to, naujoviškas ECL mikroskopijos pritaikymas leidžia realiuoju laiku, su erdvine skiriamąja geba, vaizduoti gyvas ląsteles ir 3D navikų modelius, tokius kaip sferoidai ar organoidai. Tai suteikia vertingos funkcinės informacijos apie jų metabolinę būklę, išvengiant fluorescencinei mikroskopijai būdingų problemų: fotoblukimo ir autofluorescencijos [109, 112, 136].

### 1.5 3D ląstelių kultūros modeliai vėžio tyrimuose

Trimačiai (3D) ląstelių kultūros modeliai, tokie kaip sferoidai ar organoidai, yra pranašesni už tradicines 2D ląstelių kultūras. Jie daug tiksliau imituoja *in vivo* naviko mikroaplinką, kurioje susidaro svarbūs fiziologiniai gradientai, vyksta tarpląstelinės sąveikos procesai, kurie nėra stebimi 2D ląstelių monoslouksniuose [137, 138]. Būtent dėl šio fiziologinio panašumo 3D kultūros yra ideali platforma pažangių analitinių technologijų integracijai, pavyzdžiui, elektrocheminių biosensorių, leidžiančių nuolat, neinvaziniu būdu ir kiekybiškai vertinti ląstelių išskiriamus metabolitus bei biožymenų molekules [152, 153, 154]. Tokie metodai kaip amperometrija ar impedanso spektroskopija leidžia realiuoju laiku stebėti dinamiškus ląstelių procesus, pavyzdžiui, reaktyviųjų deguonies formų (ROS) svyravimus ar ląstelių adhezijos pokyčius [154, 156, 157]. Dar viena itin perspektyvi technologija, kurią galima paminėti prie anksčiau išvardintų metodų yra ECL, kuri užtikrina aukštą erdvinę ir laiko skiriamąją gebą bei leidžia vizualizuoti biocheminius procesus šiuose 3D modeliuose be optiniams metodams būdingų foninių trukdžių, o tai suteikia galimybę detaliau analizuoti navikų atsaką į gydymą [14, 109, 136, 155].

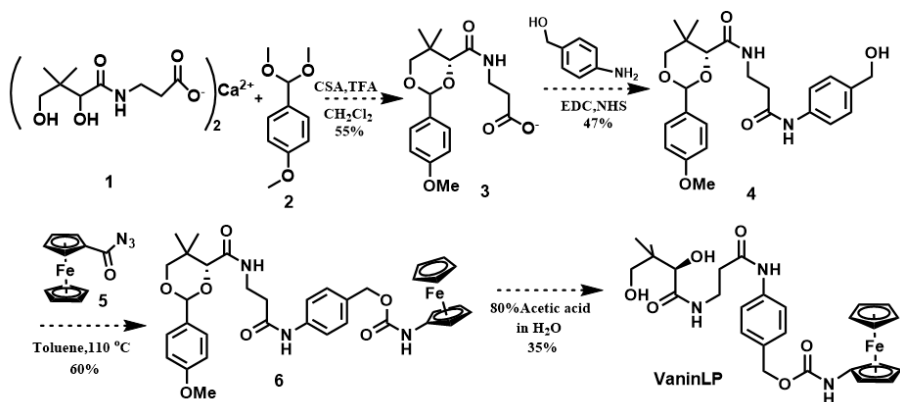
## 2. TYRIMO METODIKA

### 2.1 VaninLP zondo sintezė

VaninLP zondas buvo sintetintas pagal keturių etapų, kruopščiai suplanuotą sintezės schemą (Schema 1), pradedant nuo komerciškai prieinamo kalcio D-pantotenato (1-asis junginys). Pirmajame etape buvo apsaugota 1-ojo junginio diolio grupė, taip sukuriant tarpinį produktą – 2-ąjį junginį, kuris leido vėlesnėms reakcijoms vykti selektyviai kitame molekulės gale.

Antrajame etape 2-ojo junginio karboksirūgštis buvo aktyvuota naudojant standartinius EDC ir NHS sujungimo reagentus, leidusius prijungti 4-aminobenzilo alkoholio fragmentą ir gauti 4-ąjį junginį. Po šios prijungimo reakcijos buvo įvestas pagrindinis elektroaktyvus komponentas. 4-ajam junginiui reaguojant su azido funkcionalizuotu ferocenu padidintoje temperatūroje, prijungta “reporterio” grupė, taip formuojant pilnai apsaugotą zondą 6-ąjį junginį.

Paskutiniame etape iš 6-ojo junginio, naudojant vandeninį acto rūgšties tirpalą, buvo selektyviai pašalinta apsauginė grupė, gaunant galutinį produktą – VaninLP. Visų etapų metu tarpiniai ir galutiniai produktai buvo kruopščiai atskirti koloninės chromatografijos metodu, užtikrinant aukštą grynumą, kuris būtinas tolimesniems elektrocheminiams tyrimams.



Schema 1. VaninLP sintezė [12].

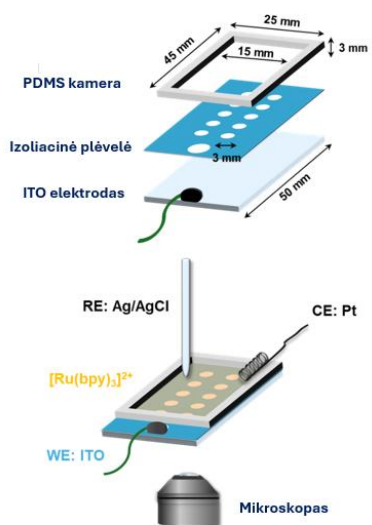
## 2.2 MCF-7 ląstelių linijos sferoidų formavimas

MCF-7 ląstelės buvo auginamos RPMI 1640 terpėje, papildytoje 10 % fetalus veršiuko serumo (FBS) ir 1 % penicilino-streptomicino, standartinėmis inkubatoriaus sąlygomis (37 °C, 5 % CO<sub>2</sub>). 3D sferoidai buvo formuojami 96 duobučių plokštelėse su U formos dugnu, į kiekvieną duobutę įpilant po 200 µL ląstelių suspensijos ir kultivuojant 1–7 dienas. Prieš ECL matavimus, paruošti sferoidai buvo nuplauti du kartus su PBS tirpalu ir vieną kartą su ECL tyrimo tirpalu. Kontroliniai fiksuotų (negyvų) sferoidų mėginiai buvo paruošti fiksuojant juos 4 % paraformaldehido (PFA) tirpalu vieną valandą ir po to papildomai plaunant PBS.

## 2.3 ECL vaizdinimas

ECL vaizdinimo sistemą (2.1.1 pav.) sudarė indžio alavo oksido (ITO) darbinis elektrodas, ant kurio buvo suformuota polidimetilsiloksano (PDMS) kamerėlė. Visa sistema buvo patalpinta ant apverstos mikroskopo, sujungto su jautria EM-CCD kamera. Prieš matavimą į kamerėlę buvo įpilamas PBS buferinis tirpalas su 5 mM [Ru(bpy)<sub>3</sub>]<sup>2+</sup> ir įkeliami tiriamieji sferoidai.

ECL signalas buvo generuojamas potencialą pakeitus šuoliu nuo 0 V iki 1,2 V. Šis staigus potencialo pokytis sukėlė elektroporaciją – laikiną ląstelių membranų pralaidumo padidėjimą, dėl kurio iš sferoido vidaus į aplinką pradėjo difunduoti biologiniai junginiai. Tuo pačiu metu ant elektrodo paviršiaus buvo oksiduojamas [Ru(bpy)<sub>3</sub>]<sup>2+</sup> liuminoforas. Jam reaguojant su iš ląstelių išsiskyrusiais biojunginiais, buvo sukeltas ECL švytėjimas, kurį po 15 sekundžių fiksavo kamera. Gautų vaizdų ECL intensyvumas vėliau buvo analizuojamas „ImageJ“ programine įranga.



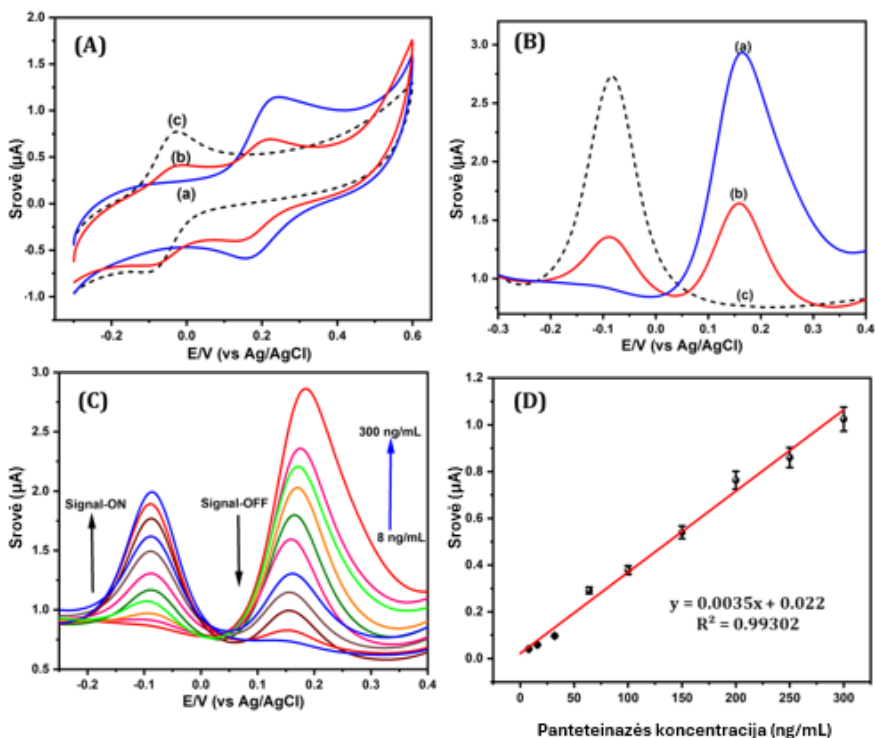
**2.11 pav.** Elektrocheminės liuminesencijos mikroskopijos vaizdinimo schema [109].

### 3. REZULTATAI

#### 3.1 VaninLP zondo elektrocheminių savybių tyrimas nustatant panteteinazės aktyvumą

Šiame darbe VaninLP zondo veikimas buvo ištirtas dviem voltamperometriniais metodais (3.1.1 pav). Atlikti ciklinės voltametrijos (CV) (3.1.1 pav. (A)) ir diferencialinės impulso voltametrijos (DPV) matavimai (3.1.1 pav (B)). CV tyrimai patvirtino zondo ratiometrinių veikimo principą, veikiant panteteinazei, pradinė zondo redokso pora ties  $+0,17$  V išnyksta ir atsiranda nauja, ties  $-0,08$  V, atitinkanti atpalaiduotą AF reporterį. Identiškas signalo poslinkis buvo užfiksuotas ir atliekant matavimus DPV metodu, kas galutinai patvirtino mechanizmo teisingumą. Kiekybiniam jautrumo įvertinimui VaninLP ( $50 \mu\text{M}$ ) buvo inkubuotas su įvairiomis panteteinazės koncentracijomis ( $8\text{--}300 \text{ ng/mL}$ ) (3.1.1 pav (C)). AF anodinės piko srovės ( $I_{pa}$ ) intensyvumas didėjo tiesiškai didėjant fermento koncentracijai ( $R^2 = 0,993$ ), o VaninLP signalo intensyvumas mažėjo. Aptikimo riba (LOD), apskaičiuota pagal  $3\delta$ /kriterijų, siekė  $2,47 \text{ ng/mL}$  (3.1.1 pav (D)).

Šie rezultatai įrodo, kad VaninLP leidžia tiesiogiai ir kiekybiškai nustatyti panteteinazės koncentraciją, užtikrina aukštą jautrumą bei selektyvumą.



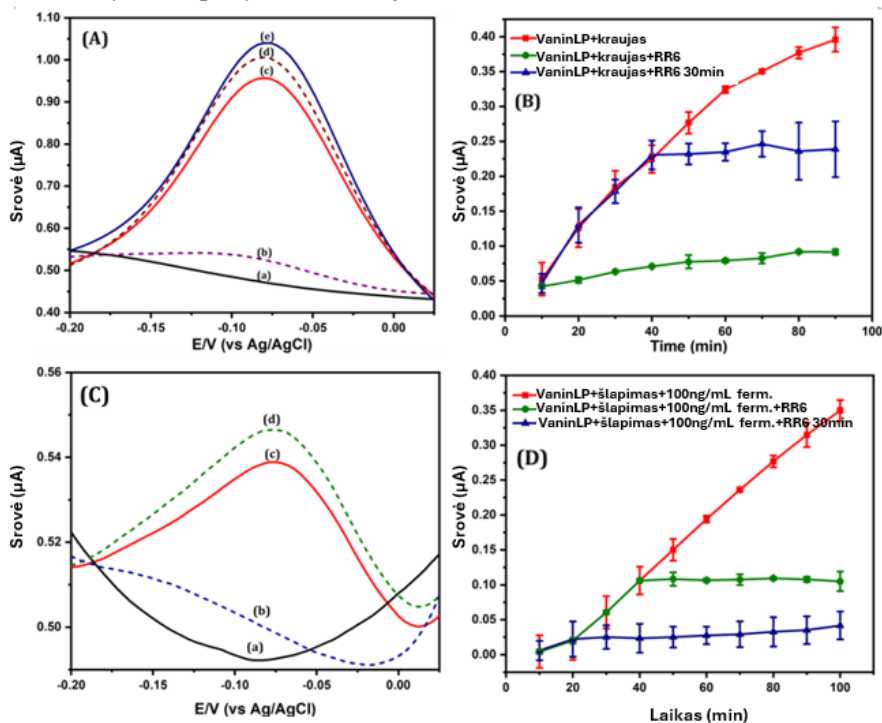
**3.1.1 pav.** Elektrocheminė VaninLP zondo charakterizacija. (A, B) Zondo atsakas į 120 ng/mL panteteinazės, išmatuotas naudojant (A) CV ir (B) DPV metodus. Kiekviename grafike palyginamas tik zondas (a), zondas su fermentu (b) ir grynas AF reporteris kaip kontrolė (c). (C) DPV atsako kreivė, rodanti 50  $\mu$ M VaninLP signalą, esant didėjančioms panteteinazės koncentracijoms (8–300 ng/mL). (D) Atitinkama kalibracijos kreivė, sudaryta iš (C) duomenų. Visi matavimai atlikti DMSO/HEPES buferyje (pH 7,0) 37  $^{\circ}$ C temperatūroje [12].

### 3.2 Panteteinazės nustatymas kraujo ir šlapimo mėginiuose

Nustačius optimalias sąlygas atlikta DPV analizė parodė, kad 50 % kraujo mėginiai, inkubuoti 37  $^{\circ}$ C temperatūroje 30 min., nesukėlė jokio signalo neigiamame potencialų regione (3.2.1 pav. A, kreivė a). Tuo tarpu kartu su VaninLP zonu inkubuotas kraujas generavo srovės atsaką (3.2.1 pav. A, kreivė b), atitinkantį 314,2 ng/mL panteteinazės koncentraciją, apskaičiuotą pagal kalibracinę kreivę (3.1.1 pav. D). Signalo stiprumas buvo nuslopintas pridėjus panteteinazės inhibitorių RR6 (3.2.1 pav. A, kreivė c). Tyrimai buvo atlikti ir su šlapimo mėginiais. Nei grynas šlapimas, nei

šlapimas su VaninLP zonu nesukėlė detektuojamo signalo (3.2.1 pav. C, kreivės a ir b), kas dera su literatūroje aprašytu labai mažu panteteinazės kiekiu šlapime. Tačiau į šlapimą įdėjus 50–55 ng/mL panteteinazės, atsirado aiškus srovės signalas (3.2.1 pav. C, kreivės c–e). Atlikti realaus laiko stebėjimo eksperimentai parodė, kad DPV signalas kraujo mėginiuose didėja inkubacijos metu (3.2.1 pav. B, raudona kreivė), o pridėjus RR6 jis yra slopinamas (3.2.1 pav. B, žalia kreivė). Inhibitorių pridėjus po 30 min., signalas mažėja (3.2.1 pav. B, mėlyna kreivė). Analogiški rezultatai gauti ir šlapimo mėginiuose su dirbtinai pridėta panteteinaze (3.2.1 pav. D).

Šie rezultatai patvirtina, kad VaninLP leidžia tiesiogiai ir patikimai aptikti bei kiekybiškai įvertinti panteteinazės aktyvumą tiek kraujo, tiek šlapimo mėginiuose be sudėtingų paruošimo procedūrų ir suteikia galimybę stebėti aktyvumo pokyčius realiuoju laiku.

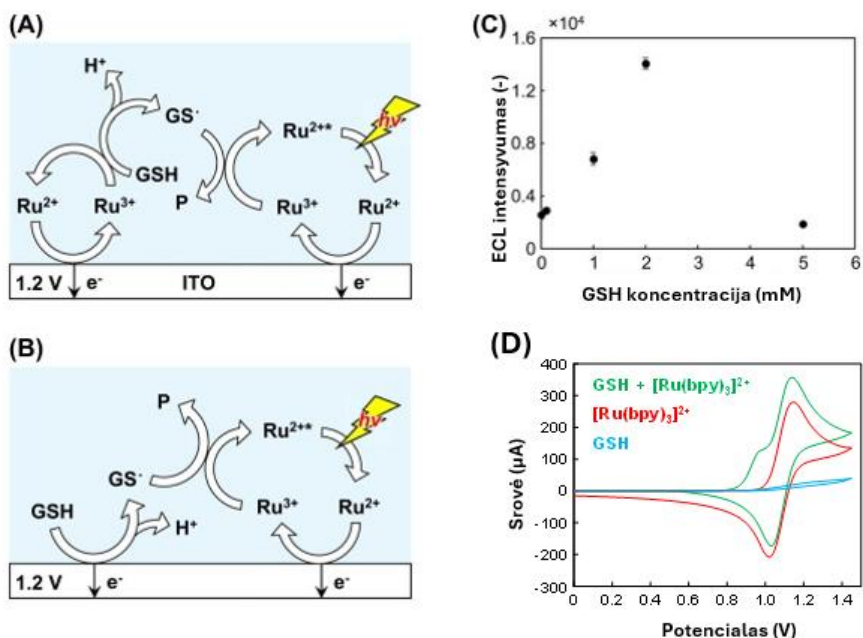


**3.2.1 pav.** (A) Kraujo matavimai DPV. Kreivės vaizduoja: a) kraujo foną; b) VaninLP zondą su kraujo mėginiu; c) zondą su krauju ir RR6 inhibitoriumi; d, e) zondą su krauju ir skirtingais pridėtos panteteinazės kiekiais (30 ir 36 ng/mL). (B) Srovės priklausomybė nuo laiko kraujo mėginiuose: be RR6 (raudona kreivė) ir pridėjus RR6 tyrimo pradžioje (žalia kreivė) arba po 30 minučių (mėlyna kreivė). Matavimai buvo atliekami kas 10 minučių, 90 minučių laikotarpyje. (C) Šlapimo matavimai DPV. Kreivės vaizduoja: a) šlapimo foną; b) VaninLP zondą su šlapimu; c, d) zondą su šlapimu ir

nurodytais pridėtos panteteinazės kiekiais (50 ir 55 ng/mL). (D) Srovės priklausomybė nuo laiko šlapimo mėginiuose: be RR6 (raudona kreivė) ir pridėjus RR6 tyrimo pradžioje (mėlyna kreivė) arba po 30 minučių (žalia kreivė). Matavimai buvo atliekami kas 10 minučių, 100 minučių laikotarpyje [12].

### 3.3 Glutationo analizė taikant ECL mikroskopiją

Nustačius, kad ankstesni tyrimai nepatvirtino NADH, kaip pagrindinio koregento, tolesni tyrimai buvo atliekami su glutationu (GSH). Eksperimentiškai patvirtinome, kad GSH oksiduoja esant 1,2 V potencialui (3.3.1 pav. (D)), o tai yra būtina sąlyga ECL signalui generuoti. Be to, atlikus literatūros analizę paaiškėjo, kad anksčiau nebuvo aprašytų signalo įjungimo anodinių ECL tyrimų su šia sistema, kas pabrėžia mūsų darbo novatoriškumą. Sudarius GSH kalibracinę kreivę (3.3.1 pav. (C)), pastebėta, kad ECL intensyvumas didėja tiesiškai iki 2 mM koncentracijos. Esant didesnėms koncentracijoms (pvz., 5 mM), signalas pradeda silpnėti dėl emisijos gesinimo efekto. Nors tokia varpo formos priklausomybė apsunkina tikslų kiekybinį įvertinimą, ji leido padaryti svarbią išvadą: norint paaiškinti sferoidų generuojamą signalą, koregento koncentracija ant elektrodo paviršiaus neturi viršyti 2 mM. Ši apskaičiuota vertė puikiai sutampa su literatūroje nurodomu viduląsteliniu GSH koncentracijų diapazonu (1–10 mM). Šis atitikimas yra svarus argumentas, leidžiantis teigti, kad būtent GSH yra pagrindinis difunduojantis koregentas, atsakingas už stebimą ECL signalą.



**3.3.1 pav.** GSH nustatymas ECL mikroskopija, naudojant  $[\text{Ru}(\text{bpy})_3]^{2+}$ . (A, B) Numanomos ECL reakcijos: (A) katalizinė ir (B) tiesioginės oksidacijos. (C) GSH kalibracinė kreivė ( $n = 3$ ). (D) 1 mM GSH (mėlyna kreivė), 5 mM  $[\text{Ru}(\text{bpy})_3]^{2+}$  (raudona kreivė) ir jų mišinio (žalia kreivė) ciklinės voltamogramos. Potencialo sklaidimo greitis: 100 mV/s [109].

## Išvados

Šiame darbe sėkmingai sukurtos dvi naujos elektrocheminės platformos, skirtos vėžio tyrimams. Šios platformos leidžia jautriai aptikti biožymenis ir tirti 3D sferoidus, todėl turi didelį potencialą tiek klinikinėje diagnostikoje, tiek fundamentiniuose tyrimuose.

1. Sukurtas novatoriškas ratiometrinis elektrocheminis zondas VaninLP, skirtas panteteinazės (Vanin-1) aktyvumui matuoti. Zondas veikia ratiometriniu signalo įjungimo principu: fermentinės reakcijos metu jo elektrocheminė smailė pasislenka nuo +0,17 V iki naujo reporterio signalo ties -0,08 V. Zondas pasižymi stipriu afinitetu fermentui, kurio Michaelio konstanta ( $K_m$ ) yra 2,38  $\mu\text{M}$  – šis rodiklis prilygsta arba yra geresnis už esamų fluorescencinių zondu.
2. VaninLP zondas pasirodė itin efektyvus tiesioginei analizei sudėtinguose biologiniuose skysčiuose. Veikianti, kaip DPV platforma, sistema pasižymi dideliu jautrumu, kurio aptikimo riba siekia 2,47 ng/mL, o tiesinis diapazonas yra nuo 8 iki 300 ng/mL, o  $R^2=0,993$ . Šie rezultatai leidžia kiekybiškai ir realiuoju laiku stebėti Vanin-1 aktyvumą neapdorotame žmogaus kraujyje ir šlapime, todėl nebereikia išankstinio mėginių paruošimo ir pabrėžia zondo, kaip potencialaus diagnostikos įrankio, vertę.
3. Šiame darbe pristytas naujas ECL mikroskopijos metodas, skirtas vizualizuoti difunduojančius biojunginius iš 3D vėžio sferoidų pasitelkiant elektroporaciją. Kalibraciniai eksperimentai su MCF-7 sferoidais parodė, kad glutationas yra pagrindinis endogeninis koregentas, generuojantis  $[\text{Ru}(\text{bpy})_3]^{2+}$  signalą. Metodas yra jautrus milimoliarinių koncentracijų diapazone (iki 2 mM). Ši metodika yra naujas funkcinio vaizdinimo įrankis, skirtas 3D navikų modelių metabolinei būsenai įvertinti.

Apibendrinant, šioje disertacijoje sukurtos dvi galingos elektrocheminės platformos, skirtos vėžio tyrimams. VaninLP zondas leidžia tiesiogiai ir jautriai aptikti biožymenis biologiniuose skysčiuose, o ECL mikroskopijos metodas yra nauja funkcinio vaizdinimo priemonė 3D navikų modeliams. Ateities darbuose VaninLP zondą planuojama pritaikyti vienkartiniams, mažo tūrio formatams, o ECL metodą tobulinti siekiant padidinti jo selektyvumą specifiniams biožymenims pažangiuose modeliuose, tokiuose kaip sferoidai ir organoidai.

## ACKNOWLEDGEMENTS

Nuoširdžiausiai dėkoju savo šeimai už besąlygišką palaikymą ir padėsinimą viso šio nelengvo mokslo kelio metu. Jūsų patarimai ir emocinė parama sunkiausiomis akimirkomis buvo neįkainojami. Be Jūsų nebūčiau pasiekęs to, ką pasiekiau šiandien.

Esu be galo dėkingas savo vadovei dr. Ingai Morkvėnaitei-Vilkončienei. Ačiū, kad patikėjote manimi, kai pats sakiau „Niekada nestosiu į doktorantūrą“, ir pakvietėte prisijungti prie savo komandos. Dėkoju už išskirtinę mentorystę, padėjusią pakloti tvirtus jauno tyrėjo pamatus, ir už parodytą pasitikėjimą.

Taip pat dėkoju prof. Arūnui Ramanavičiui už vertingas konsultacijas, pagalbą ir nuolatinį motyvavimą judėti pirmyn.

Nuoširdžiai dėkoju savo stažuočių vadovams – dr. Wojciech Nogala, prof. Sheng-Tung Huang ir prof. Kosuke Ino. Ačiū Jums už skirtą laiką, išskirtinę mentorystę ir galimybę mokytis iš geriausių. Jūsų perduotos žinios ir patirtis neabejotinai praplėtė mano, kaip mokslininko pasaulėžiūrą.

Ačiū draugams – tiek tiems, kurie buvo šalia nuo pat pradžių, tiek tiems, kurie prisijungė vėliau. Jūsų palaikymas buvo be galo svarbus.

Dėkoju laboratorijos kolegoms Lietuvoje ir stažuočių metu, kurių daugelis tapo gerais draugais. Laikas, praleistas kartu, ir diskusijos buvo ne tik produktyvios, bet ir nepamiršamos.

Galiausiai, ačiū Jums, skaičiusiems šį darbą. Ir ypatingas ačiū tiems, kurie sunkiai tiki, kad šią akimirką stoviu čia, apsigynęs daktaro laipsnį! 😊

## CURRICULUM VITAE

Name and surname: Tomas Mockaitis  
Email: [tomas.mockaitis@ftmc.lt](mailto:tomas.mockaitis@ftmc.lt)

Education:

**2021 – 2025** Chemistry N003 doctoral studies, Centre for Physical Sciences and Technology, Department of Nanotechnology.

**2019 – 2021** Master's studies in biochemical analysis in Vytautas Magnus University, Faculty of Natural Sciences, department of biochemistry.

**2015 – 2019** Bachelor's studies in biochemistry in Vytautas Magnus University, Faculty of Natural Sciences, department of biochemistry.

Work experience:

**2021.03 – 2022.09** Biotechnologist at Thermo Fisher Scientific Baltics.

**2023.08 – present** Junior Researcher at Centre for Physical Sciences and Technology, department of Nanotechnology.

**2024.09 – present** Junior assistant at Klaipeda State College.

## LIST OF PUBLICATIONS AND CONFERENCES

Publications included in the thesis:

**Mockaitis, T.**, Shikuwa, R., Utagawa, Y., Oba, K., Hiramoto, K., Abe, H., Morkvėnaitė-Vilkončienė, I., Shiku, H., Ino, K. Electrochemiluminescence microscopy of diffusive biocompounds as co-reactants in cell spheroids with  $[\text{Ru}(\text{bpy})_3]^{2+}$ , *Sensors and actuators B: Chemical*, **2025**, *441*, 137944, 1-7. [doi.org/10.1016/j.snb.2025.137944](https://doi.org/10.1016/j.snb.2025.137944).

Kumaragurubaran, N., Huang, Y.-Z., **Mockaitis, T.**, Arul, P., Huang, S.-T., Lin, H.-Y., Wei, Y.-C., Morkvenaite-Vilkonciene, I. Development of an Activity-Based Ratiometric Electrochemical Switch for Direct, Real-Time Sensing of Pantetheinase in Live Cells, Blood, and Urine Samples, *ACS sensors*, **2024**, *9* (10), 5436-5444. [doi.org/10.1021/acssensors.4c01658](https://doi.org/10.1021/acssensors.4c01658).

Ino, K., **Mockaitis, T.**, Shikuwa, R., Oba, K., Hiramoto, K., Morkvenaite-Vilkonciene, I., Abe, H., Shiku, H. Recent Advances in Electrochemiluminescence Sensing for in Vitro Cell Analysis: A Review, *Analytical sciences*, **2025**, *41* (5), 557-569. [doi.org/10.1007/s44211-025-00723-x](https://doi.org/10.1007/s44211-025-00723-x).

Publications not included in the thesis:

Bendinskaite, S., Bruzaite, I., Rozene, J., **Mockaitis, T.**, Zinovicius, A., Morkvenaite-Vilkonciene, I., Ramanaviciene, A., Ramanavicius, A. Microbial Fuel Cell Based on Ensifer Meliloti, *Journal of the electrochemical society*, **2024**, *171* (10), 1-8. [doi.org/10.1149/1945-7111/ad8037](https://doi.org/10.1149/1945-7111/ad8037).

Attended conferences:

**Mockaitis, T.,** Bubnelytė, A., Bružaitė, I., Ramanavičius, A., Morkvėnaitė-Vilkončienė, I. Influence of redox mediators on performance of Ensifer meliloti microbial fuel cells, Biosensors 2025, 19-22 May, 2025, Lisbon, Portugal.

<https://www.elsevier.com/events/conferences/all/anniversary-world-congress-on-biosensors>

**Mockaitis, T.,** Huang, S-T., Kumaragurubaran, N., Morkvėnaitė-Vilkončienė, I. Development of a latent electrochemical redox probe for direct detection of pantetheinase in live cells, whole blood, and urine samples, Pittcon 2025, 1-5 March, 2025, Boston, MA, United States.

<https://app.swapcard.com/event/pittcon2025/planning/UGxhbm5pbmdfMjQ1MzM1OA==>

**Mockaitis, T.,** Huang, S-T., Morkvėnaitė-Vilkončienė, I. Advancing GGT research with secm and novel electrochemical probes, Open readings 2024, 23-26 April, 2024, Vilnius, Lithuania.

[https://openreadings.eu/wpcontent/uploads/2024/05/2024\\_abstract\\_book.pdf](https://openreadings.eu/wpcontent/uploads/2024/05/2024_abstract_book.pdf)

**Mockaitis, T.,** Morkvėnaitė-Vilkončienė, I. MFC efficiency with E. meliloti and redox mediators, FizTeCh2024, 15-17 October, 2024, Vilnius, Lithuania.

<https://www.ftmc.lt/news/1895/69/14-oji-FTMC-doktorantu-ir-jaunuju-mokslininku-konferencija-FizTeCh2024>

**Mockaitis, T.,** Huang, Y-Z., Huang, S-T., Morkvėnaitė-Vilkončienė, I. Development of latent electrochemical redox probe for detecting VANIN- 1 in blood and cells, FizTeCh2023, 18-19 October, 2023, Vilnius, Lithuania.

<https://www.ftmc.lt/uploads/pdf/Dokumentai/doktorantura/FizTech2023/Book%20of%20abstracts%202023.pdf>

**Mockaitis, T.,** Nogala, W., Boguševičė, A., Kižys, K., Morkvėnaitė-Vilkončienė I. Imaging of glucose oxidase activity by scanning electrochemical microscopy, Open readings 2023, 18-21 April, 2023, Vilnius, Lithuania.

<https://openreadings.eu/wp-content/abstracts/abstract-2023.pdf>

Not attended conferences:

Barkauskas, D., **Mockaitis, T.**, Bružaitė, I., Morkvėnaitė-Vilkončienė, I. Electrochemical investigation of CHO cells with various redox mediators, Open readings 2025, 13-16 May, 2025, Vilnius, Lithuania. <https://openreadings.eu/>

Boguševičė, A., **Mockaitis, T.**, Morkvėnaitė-Vilkončienė, I. Application of mfc in agricultural samples using *E.Meliloti*, Open readings 2025, 13-16 May, 2025, Vilnius, Lithuania. <https://openreadings.eu/>

Boguševičė, A., **Mockaitis, T.**, Morkvėnaitė-Vilkončienė, I., Huang, Y-Z., Huang, S-T. Yeast-powered microbial biofuel cells with quinones as mediators, CYSENI 2024, 21–23 May, 2024, Kaunas, Lithuania. <https://cyseni.com/programme/>

Bubnelytė, A., **Mockaitis, T.**, Bružaitė, I., Morkvėnaitė-Vilkončienė, I. Electrochemical analysis of ensifer meliloti using diverse redox mediators for MFC applications, Open readings 2025, 13-16 May, 2025, Vilnius, Lithuania. <https://openreadings.eu/>

Kulikauskaitė, B., Zinovičius, A., Sapijanskaitė-Banevič, B., **Mockaitis, T.**, Ramanavičius, A. Development of a microbial biofuel cell using biocompatible nanocomposites, Chemistry and chemical technology 2025, 9 May, 2025, Vilnius, Lithuania. <https://www.journals.vu.lt/proceedings/issue/view/2783>

Internships:

2022.09-2023.02 Institute of Physical Chemistry Polish Academy of Science.  
Supervisor: Ph. D Wojciech Nogala

2023.03-2023.06 National Taipei University of Technology.  
Supervisor: Professor Ph.D Sheng-Tung Huang

2024.08-2024.10 Tohoku University.  
Supervisor: Assoc. Prof. Ph.D Kosuke Ino

## Projects:

2024.11.04 – 2025.05.30. Junior researcher in Center for Physical Sciences and Technology. Project no. 1620-SF458. „MTEP Idea Verification – Electrochemiluminescent Cell Imaging After Electroporation“.

Coordinator PhD Evaldas Balčiūnas

2024.08.28 – 2025.03.31. Junior researcher in Center for Physical Sciences and Technology. Project no. S-MIP-22-87 „ Development and improvement of a biosensor using polymer and nanomaterial composites and scanning electrochemical microscopy“.

Coordinator Assoc. Prof. PhD Inga Morkvėnaitė-Vilkončienė

## NOTES

Vilnius University Press  
Saulėtekio Ave., 9, Building III, LT-10222 Vilnius  
mail: [info@leidykla.vu.lt](mailto:info@leidykla.vu.lt), [www.leidykla.vu.lt](http://www.leidykla.vu.lt)  
[bookshop.vu.lt](http://bookshop.vu.lt), [journals.vu.lt](http://journals.vu.lt)  
Print run copies 25